Optical Characterization of Bio-Inspired Functional Materials, Metal Nanoparticles, and Their Composites

Kathryn N. Guye

A dissertation

submitted in partial fulfillment of the

requirements for the degree of

Doctor of Philosophy

University of Washington

2021

Reading Committee:

David S. Ginger, Chair
David J. Masiello
Bo Zhang

Program Authorized to Offer Degree:

Chemistry

© Copyright 2021

Kathryn N. Guye

University of Washington

ABSTRACT

Optical Characterization of Bio-Inspired Functional Materials, Metal Nanoparticles, and Their Composites

Kathryn N. Guye

Chair of the Supervisory Committee:
Professor David S. Ginger
Department of Chemistry

The ability to characterize optically-active materials by their transmutable optical signatures can both yield noncontact information on the nanoscale behavior of the material and be used to predict its applicable functionality. The work presented herein covers the optical characterization of a variety of metal nanoparticles, stimulus-responsive bio-inspired polymers, and biotemplated metal nanoparticles. We first show the optical modeling of a variety of plasmonic nanoparticles by the finite-difference time-domain method, supporting experimental observation made by both traditional and novel spectroscopic methods. Using finite-difference time-domain modeling, we identify a large magnitude of interparticle coupling for reversible, reconfigurable nanoparticle composites with the thermoresponsive polymer microgel, poly(N-isopropylacrylamide) and compare the simulated results to experimental UV-Vis extinction spectra. We then confirm the experimental results of a new photoacoustic absorption spectroscopy technique by simulating the scattering, absorption, and extinction coefficients of different sized gold nanorods and compare with the experimental findings. Lastly, finite-difference time-domain modeling allows us to deconvolute complex scattering spectra and draw conclusions about the coupling of plasmonic-excitonic system which could not be otherwise inferred experimentally. Next, we characterize a self-folding polymer with pendant host-guest cyclodextrin-azobenzene derivatives by

demonstrating reversibility of the azobenzene derivative isomerization and photoisomerization quantum yield differences providing evidence of self-folding via UV-Vis extinction spectroscopy. Finally, we employ *de novo* designed protein nanofibers to electrostatically template gold nanoparticles at the surface of a charged substrate and explore how substrate-nanoparticle repulsion via nanoparticle size and the pH of solution dictate the final assembly outcome using the well-studied the Derjaguin-Landau-Verwey-Overbeek theory to justify our results. We then employ hyperspectral darkfield microscopy to compare optical scattering observations for larger nanoparticles with the assembly conclusions made with small gold nanoparticles and motivate the use of optical scattering microscopy for future *in situ* characterization and observation of protein-templated nanoparticle assemblies.

TABLE OF CONTENTS

LIST OF FIGURES

LIST OF TABLES

ACKNOWLEDGEMENTS

I am incredibly indebted to so many people who have guided and supported me on my academic journey throughout the years. In college I had the wonderful opportunity attend a talk by United States Supreme Court Justice Sonia Sotomayor where she emphasized the point that no one can succeed alone, especially in academia. I knew it was true then, and I am elated to have the opportunity here to express my gratitude to the village that raised me.

First and foremost I would like to acknowledge my parents, Ronald and Jacqueline Guye for believing in me and being there to support me through the good and hard times. You were always there to cheer my on while I explored new interests and made so many opportunities possible that led me here today. Thank you both with so much love.

With much gratitude, I would like to thank my advisor, Dr. David S. Ginger, for his guidance over the past several years. There was never a moment I felt like I was not growing or learning something new, and I appreciate the time and energy invested into helping me evolve into a much better scientist than from where I began. I would also like to express my gratitude to my supervisory committee and research collaborators, Dr. Arka Majumdar, Dr. Bo Zhang, Dr. David Masiello, Dr. Suzie Pun, and Dr. David Baker for their tremendous guidance and support over the years. I have enjoyed our discussions and learned so much from their expertise. Thank you to my undergraduate research advisor, Dr. Jonas I. Goldsmith, for introducing me to academic research and trusting me to take the reins on my own project. And to the one who started me on this path, an incredible thank you to my high school chemistry teacher, Ms. Barb Webb, who not only made chemistry enjoyable and accessible, but often went above and beyond to provide our classes with extra support when needed.

I would like to acknowledge the Department of Energy Basic Energy Sciences Office for providing the funding for a large portion of the following work through the Energy Frontier Research Center the Center for the Science of Synthesis Across Scales (CSSAS), and express my gratefulness to the entire CSSAS community for not only generating a large volume of incredible science, but also for cultivating a unique community and support network, yielding many professional connections and friendships.

Thank you to the current and former members of the Ginger Lab who have overlapped my time here, Erin Jedlicka, Jiajie Guo, Sarthak Jariwala, Justin Pothoof, Ramsess Quezada, Muammer Yaman, Shaun Gallagher, Maddie Breshears, Margherita Taddei, Yangwei Shi, Emerson Chen, Jessica Kong, Jeff Harrison, Jake Precht, Dr. Yun Liu, Dr. Lucas Flagg, Dr. Mark Ziffer, Dr. Soumyadyuti Samai, Dr. Sarah Vorpahl, Dr. Dane DeQuilette, Dr. Phillip Cox, Dr. Durmus Karatay, Dr. Jian Wang, Dr. Xudong Wang, Dr. Connor Bischak, Dr. Franziska Muckel, Dr. Zhaoxia Qian, Dr. Jie Zhang, Dr. David Moerman, Dr. Giles Eperon, and Dr. Tony Wu, for all of their support that helped make possible my personal and professional successes, whether in the form of providing practice talk feedback or making coffee runs in the rain. I have been very fortunate to be surrounded by such amazing scholars. In particular, I would like to thank Dr. Zhaoxia Qian and Dr. Soumyadyuti Samai for their mentorship when I was first entering the lab, and Muammer Yaman, Shaun Gallagher, Dr. Franziska Muckel, and Dr. Xudong Wang for our amazing collaborations and encouragement to always produce the best work.

I have also had the privilege to work with three undergraduate researchers during my time at UW, James Lee, Ariel Scott, and Gerald Liao. Every day I was inspired by their excitement to learn something new, and the insights they brough to each research project continue to benefit the lab and our work.

Thank you to all of the departmental staff members who often went above and beyond to support me as a student and researcher from those in the front office, to the research stockroom, the Molecular Analysis Facility and Research Training Testbeds instrumental staff, the research coordinators, and the maintenance and custodial staff members.

I would like to thank my Michigan, Pennsylvania, Washington, and beyond friends, communities, and support systems. The outpouring of love and support I have received from so many throughout this journey has meant so much to me, and I would not have made it to this point without them.

Finally, a massive thank you to the front line workers, researchers, and public health experts who put forth a monumental effort and great personal sacrifices to minimize the lasting effects the SARS-CoV-2 pandemic will have on our lives and community. While nothing about this pandemic has felt minimal, their heroic efforts saved untold countless lives and provided a pathway to return to normality.

DEDICATION

Ronald Lee Guye (1957-2016)

I dedicate this dissertation to my father, Ronald L. Guye, who passed away on August 28, 2016. I will always hold close to my heart the spiritual and intellectual lessons you endowed us with, and I hope to emulate even a fraction of your strength, wisdom, and compassion wherever I go. I could not have ever imagined arriving at this point without you, but the legacy of your love continues on, and I know you are watching over us from Heaven. I miss you and I love you.

CHAPTER 1. INTRODUCTION

1.1 OVERVIEW

In this chapter, we briefly discuss the origin of the optical properties of plasmonic nanoparticles, how finite-difference time-domain simulations have developed a greater understanding of the optoelectronic interactions of plasmonic particles, the use of azobenzene and its derivatives in stimulus-responsive, reversible/reconfigurable materials, and finally, the assembly of bio-inspired templates and bio-directed assembly of inorganic materials.

1.2 OPTICAL PROPERTIES OF PLASMONIC NANOPARTICLES

The optical properties of plasmonic nanoparticulates first became relevant centuries ago when it was discovered they could be embedded in glass to prepare beautifully red-stained glass and ceramics.[1] Since then, our understanding of localized surface plasmon resonances and the optoelectronic capabilities they enable has greatly matured and have been applied to much more sophisticated technologies such as plasmonic nanosensors,[2–4] nanolasers,[5–7] nanopixels,[8,9] and nanomedicine.[10,11] The origin of these exciting optical properties is due to the localized surface plasmon resonance (LSPR), generated by the oscillation of free electrons of the metal nanoparticle as shown in figure 1.2.1 below.[12] This is made possible only when the nanoparticle is much smaller than the incident wavelength of light so that the metallic electron cloud feels the push-pull of the alternating electric field of the incident light wave.

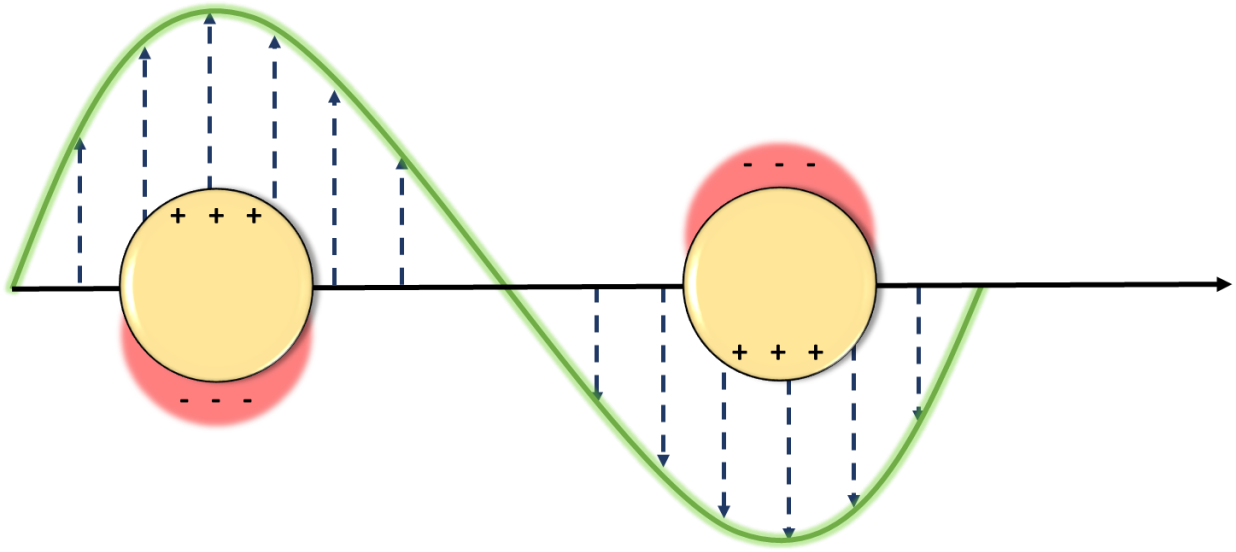

Figure 1.2.1. Oscillation of the free electron cloud of a plasmonic gold nanoparticle due to the excitation of the localized surface plasmon resonance (LSPR). The black solid vector represents the direction of light and the blue dashed lines the direction of the electric field, perpendicular to the incident light vector. The electron cloud is repelled by the electric field, resulting in a dipole across the nanoparticle surface.

As described by Mie theory, for gold nanoparticles, the electric dipole generated by the oscillation of free electrons is primarily responsible for the strong light scattering at the LSPR position.[13] This scattering of light is responsible for the bright, opalescent color of nanoparticle solutions which have been used for both aesthetic and functional purposes. Because the extinction at the LSPR is dependent on the energy dipole, it is also extremely sensitive to changes to the dielectric background of the environment. This results in the position of the LSPR to observably redshift with even a slight increase to the local refractive index. As such, nanoparticles can serve as exceptional nanosensors.[12,14]

Because the LSPR is the result of a collective oscillation across the surface of the metallic nanostructure, additional resonance modes can be introduced by changing the geometry of the nanoparticle from isotropically spherical to a variety of anisotropic shapes, such as rods, which

exhibit a longitudinal and transverse LSPR due to the variation in length and width respectively.[15] As such, if two spherical nanoparticles come into close proximity with one another, their plasmonic modes couple, resulting in a longitudinal resonance across the dimer axis in addition to the perpendicular transverse peak, as electrons oscillate in motion together across the dimer structure rather than as independent particles. Additionally, the electric field of the dimer structure is greatly enhanced in the gap between the two particles when the longitudinal mode is activated.[16–18]

Therefore, significant attention has been given by researchers for assembling gold nanoparticles in an ordered and controlled manner to take advantage of this impressive optoelectronic feature for potential applications in sensing, catalysis,[19,20] lasing,[21,22] and optical transistors.[23] In addition to the assembly of static structures, the use of many stimulus-responsive organic functional materials which can reversibly tune the interparticle distance, orientation, or aggregation state of inorganic nanoparticles, and therefore the subsequent tuning of the optoelectronic properties of the system,[24] has been intensely studied as discussed in the following section.

1.3 Stimulus-Responsive, Reversible, and Reconfigurable Materials

Organic materials with intrinsic molecular switches, coupled to functional inorganic particles, have created a path forward for stimulus-responsive, tunable composite materials for use in many applications such as sensing,[25,26] drug delivery,[27,28] climate control,[29] and controllable catalysis.[19] Such stimuli include heat,[30] oxidation state,[31] magnetic field,[32] pH,[33] and light.[34] Light-responsiveness, in particular, serves as a valuable stimulus as it can be applied to a given system in a noninvasive, noncontact manner and from a distance yielding an additional dimension of

control and applicability. Light is such an attractive stimulus-type, many fields have developed relay mechanisms for achieving a photoresponse from an otherwise photo-unresponsive system.

For example, Baumberg and coworkers have published several studies[35–38] employing the thermoresponsive polymer, poly(N-isopropylacrylamide) (PNIPAM), with gold nanoparticles to create stimulus-responsive actuating particles and films. By exciting such a system at the resonant wavelength of the gold nanoparticles, they take advantage of the thermoplasmonic properties of gold nanoparticles. When illuminated at the resonant wavelength, the metallic electrons are excited into a higher energy state. If those electrons are not transferred to another material via an oxidation process, they will thermally relax back to the ground state, releasing a significant amount of heat at the nanoparticle surface.[39–41] Such heat can then be transferred to local materials like PNIPAM to trigger the temperature-dependent coil-to-globule transition.

Another indirect mechanism for using light as a stimulus for particle assembly includes the use of photoacids and photobases to toggle a pH-responsive material. Photoacids are typically chromophores which contain a very weakly acidic labile proton (pK_a ~7). However, when photoexcited, the molecule reduces its affinity for that proton, resulting in a pK_a drop of several pH units (pK_a^* ~ 0-2).[42,43] Photobases work by a similar mechanism, however can act as a proton acceptor or hydroxyl group donator. Recently Yucknovsky et al.[44] demonstrated the use of photoacid-photobase pair to reversibly drive the aggregation and de-aggregation of gold nanoparticles capped with mercaptohexanoic acid, a pH-responsive ligand. Rather than manually titrating in an acid and base source, they incorporated 8-hydroxypyrene-1,3,6-trisulfonic acid (HPTS) as the photoacid, which when protonating the mercaptohexanoic acid at the surface of the nanoparticles resulted in interparticle capping ligand hydrogen bonding, and an aggregation of the

nanoparticles. By triggering the photobase, 6-methoxyquinoline, those protons were taken up by the photoinduced strong base, and the particle system de-aggregated.

Ultimately, to reduce cycling fatigue of a system, directly photoresponsive molecular switches are popular for directing reconfigurable materials. Azobenzene and azobenzene derivatives, in particular, are perhaps one of the most-studied photoresponsive molecular switches used to direct the assembly of organic and inorganic materials.

The photoisomerization of trans-azobenzene to cis-azobenzene results in two main physical changes. The trans-form of azobenzene is planar with no net-dipole across the azo double bond, whereas the cis-form breaks planarity and does yield a net-dipole perpendicular to the azo bond.[45] As a result, material behavior can be impacted as the result of local changes in polarity and functional group solubility or due to changes in steric interactions between neighboring molecules.

For example, in 2014 Köhntopp et al.[45] showed that gold nanoparticles with a co-ligand cap of azobenzenethiolate and alkylthiolate monolayers were stable in a solution of toluene when the azobenzene was in the predominately trans-, nonpolar-form, but when photoconverted to the predominantly cis-form with UV light, the azobenzene adapted a net dipole moment and was no longer miscible in the nonpolar solvent, resulting in nanoparticle aggregation. The nanoparticles could be redispersed, then, with visible light illumination.

The effect of isomer geometry has been well-demonstrated by Ginger and coworkers via azobenzene-modified DNA. In 2012, Yan et al.[46] used azobenzene-modified DNA to functionalize the surface of gold nanoparticles, showing nanoparticles functionalized with complimentary DNA strands quickly aggregated when the azobenzene was in the trans form, allowing the azobenzene to intercalate between the DNA base pairs. When photoisomerized to the cis-state, the non-planar structure of the azobenzene broke apart the complimentary base pairing, resulting in a melting of

the double strand (ds)-DNA structure to the single strand (ss)-DNA, and a redispersal of the nanoparticle aggregates. And in 2013, Yan et al.[47] further showed the local steric environment around azobenzene influenced the photoisomerization quantum yield of the trans-to-cis azobenzene embedded in a DNA sequence. Expanding on this work, a few years later, Samai and coworkers[16,48] demonstrated a temperature-dependence of the photoisomerization quantum yield of azobenzene embedded in DNA as a function of steric hindrance around the azobenzene chromophore. Below the thermal melting point of DNA, the photoisomerization quantum yield of the azobenzene was dependent on the local DNA environment, whereas at temperatures above the thermal melting point of the various DNA sequences, the azobenzene quantum yields became identical. The combined works of Yan, Samai, and coworkers revealed that the reversible photoinduced transition between ds-DNA with trans-azobenzene and ss-DNA with cis-azobenzene is the result of the cis-isomer breaking planar geometry and disrupting the complementary DNA base pair interactions. Samai and coworkers then extended this work by generating asymmetric gold nanoparticle dimers using an azobenzene-modified DNA hairpin. Upon trans-to-cis isomerization, the hairpin loop could no longer hold its closed geometry due to steric hindrance of the cis-form azobenzene, and opened to an uncoiled DNA strand. This in in turn, increased the interparticle distance between gold nanoparticles. By photoswitching between the cis- and trans-state, actuation of the nanoparticles became possible.

To shift the preferred photoisomerization wavelengths of both azobenzene transitions into the visible light in order to prevent UV-damage to organic systems, tetra-*ortho*-substitutions of azobenzene have been shown to redshift the absorption bands of azobenzene.[49,50] Additionally, such substitutions have also proven to thermally stabilize the cis-state of the azobenzene resulting in thermal half-lives of days.[49,51]

Finally, in a combination of polarity and geometric effects of the azobenzene isomerization, a number of reports have demonstrated the effectiveness of the host-guest inclusion complex of azobenzene with α-, β-, and γ-cyclodextrins.[27,52–54] In short, the hydrophobic interior of the cyclodextrin cup stabilizes the nonpolar trans-azobenzene dissolved in an aqueous solution, while the polar cis-form is both more stable in the aqueous environment, and also does not fit within the cyclodextrin interior.[54,55] This interaction has been shown to reversibly crosslink bifunctionalized polymers[56,57] and cause the demicellization of semi-soluble polymers[27] leading to applications such as drug delivery and decontamination.

In conclusion, molecular switches have enabled the reversible assemblies and actuation of organic and organic-inorganic hybrid composites. Stimuli such as heat, pH, and light can be used to toggle on and off such molecular switches, driving reversible or irreversible morphological changes. Light, in particular, as a non-contact and noninvasive stimulus is of particular interest to many material researchers, driving the development of many phototriggered relay mechanisms such as thermoplasmonic heating and the use of photomediated acids and bases, and direct triggers such as azobenzene-related functional materials. Such functional materials will certainly contribute to many applications such as solar harvesting, drug delivery, interior climate control, and beyond.

1.4 Biotemplates and Bio-Directed Assemblies

The emerging field of using biological and bio-inspired materials for the hierarchical assembly of inorganic nanostructures has grown rapidly due to the intrinsic evolved purpose of many organic scaffolds to organize inorganic materials,[58,59] atomic precision afforded to the *de novo* synthesis of biological nanostructures,[60] and tunable interactions not always afforded to ligand-mediated interactions.[61]

A prime example of such bio-directed structures is the body of work generated by Mirkin and coworkers over the past 25 years employing DNA to assemble colloidal nanoparticles in programmable ionic crystal structures.[61–67] By tuning the overlapping binding strength of complementary DNA covalently bound to the surface of gold nanoparticles, Mirkin and coworkers have continuously proven nano-to-microscale control over the crystallization of colloidal nanoparticles by annealing out high fidelity ionic crystal structures dependent on nanoparticle size and surface coverage of DNA, and have gone on to show reversible assembly and disassembly by employing azobenzene-modified DNA and metallic electron-like behavior of DNA-functionalized nanoparticles only ~1.5 nm in diameter which stabilize larger nanoparticles, 10 nm in diameter, into a metallic lattice structures. Beyond ionic crystal lattice structures, DNA has been employed in DNA origami,[68,69] nanoparticle thin film assembly,[70] and stimulus-responsive actuating nanoparticle dimers as previously discussed.[16,46]

By utilizing biomaterials, researchers often take advantage of the chiral suprastructure which emerges from chiral amino acid building blocks. Rosi and coworkers have demonstrated chiroptical helices of gold nanoparticles by peptide-templating, with g-factors up to 0.04[71] and the ability to tune the structural geometry and therefore chirality by engineering specific peptide sequences.[72,73] Lee et al. showed that by introducing a chiral amino acid or peptide into the growth solution of gold nanocubes, chiral helicoid nanoparticles were grown with g-factors up to 0.2.[74] Other plasmonic capabilities, such as electric field enhancement, can be amplified via careful engineering of the biotemplates. In 2018, Yan et al.[75] published work demonstrating the use of peptoids – a synthetic peptide analog with the functional side chain stemming from the backbone nitrogen rather than the α-carbon[76] – to direct the growth of highly-branched gold nanoparticles

which yielded an electric field enhancement up to 10^5-fold greater than colloidal particles prepared by common methods.

Stimulus-responsive behavior can even be incorporated into biomimetic materials by virtue of their programmable design, such as described above, and often, due to the nature of several amino acids containing pH-sensitive labile protons, have a surface charge that is notably dictated and tunable by the local pH of the solution. Recently, Jin et al.[77] prepared peptoid nanotubes designed with an inner core and outer wall lined by hydrophilic, carboxylic acid moieties, while the interior of the wall contained hydrophobic groups. Due to the acidic nature of the carboxylic acid functional groups, at high pH, the groups are deprotonated, assuming a formal negative charge, and generating electrostatic repulsion within the inner core and maximizes the inner diameter to passivate repulsive forces. If the pH drops below the pK_a of the functional groups, the carboxylic acids are protonated and carry no net charge. The peptoid core then collapses due to the lack of repulsive force. Actuation of the nanotube diameter can be switched between ~13 nm at pH 3.6 and ~25 nm at pH 8.0. Another approach to a stimulus-responsive biomaterial, has been the design of 2D ^{C98}RhuA lattices by Tezcan and coworkers[78,79], wherein the truncated square pyramidal RhuA monomers are interconnected via a disulfide bond. The RhuA monomer, carries a net dipole perpendicular to its base, allowing for controllable adsorption onto a mica template. Furthermore, the disulfide bond is redox-responsive, an assembly of the 2D lattice with oxidation and a disassembly of the lattice with reduction of the disulfide bond. Furthermore, the 2D lattice displays auxetic behavior with mechanical perturbation of the solution, changing reversibly between an porous corner-to-corner orientation of each monomer building block to a close-packed side-to-side orientation. Finally, as previously mentioned, the rapid progression in the *de novo* design of proteins has accelerated the ability to devise programmable designs of biological templates for

directed applications.[80–83] Therefore, building in a reversible, reconfigurable mechanism for protein assembly was made possible by Boyken et al.[84] by designing proteins with a central histidine network. The histidine residues engage in hydrogen bonding with neighboring protonated residues, however upon a decrease in the solution pH, the histidine becomes protonated as well, breaking the stabilizing hydrogen bonding and creating steric hindrance, resulting in a disassembly of the protein. If the pH is raised again, the protein monomers will reassemble.

By using such bio- and bio-inspired materials to direct the assembly of inorganic nanoparticles, the achievement of specific applications may soon be achieved as well as the emergence of new and exciting optoelectronic properties.

1.5 REFERENCES

1. Freestone, I.; Meeks, N.; Sax, M.; Higgitt, C. The Lycurgus Cup - A Roman nanotechnology. *Gold Bull.* **2008**, *40*, 270–277.
2. Haes, A. J.; Zou, S.; Schatz, G. C.; Van Duyne, R. P. Nanoscale optical biosensor: Short range distance dependence of the localized surface plasmon resonance of noble metal nanoparticles. *J. Phys. Chem. B* **2004**, *108*, 6961–6968.
3. Piliarik, M.; Kvasnička, P.; Galler, N.; Krenn, J. R.; Homola, J. *Local refractive index sensitivity of plasmonic nanoparticles*. (2011).
4. El-Ansary, A.; Faddah, L. M. Nanoparticles as biochemical sensors. *Nanotechnology, Science and Applications* **2010**, vol. 3 65–76.
5. Wang, B.; Yu, P.; Wang, W.; Zhang, X.; Kuo, H. C.; Xu, H.; Wang, Z. M. High-Q Plasmonic Resonances: Fundamentals and Applications. *Adv. Opt. Mater.* **2021**, *2001520*, 1–30.
6. Luo, Y.; Zhao, J. Plasmon-exciton interaction in colloidally fabricated metal nanoparticle-quantum emitter nanostructures. *Nano Res.* **2019**, *12*, 2164–2171.
7. Zhou, W.; Dridi, M.; Suh, J. Y.; Kim, C. H.; Co, D. T.; Wasielewski, M. R.; Schatz, G. C.; Odom, T. W. Lasing action in strongly coupled plasmonic nanocavity arrays. *Nat. Nanotechnol.* **2013**, *8*, 506–511.
8. Rothemund, P. W. K. Folding DNA to create nanoscale shapes and patterns. *Nature* **2006**, *440*, 297–302.
9. Peng, J.; Jeong, H. H.; Lin, Q.; Cormier, S.; Liang, H. L.; De Volder, M. F. L.; Vignolini, S.; Baumberg, J. J. Scalable electrochromic nanopixels using plasmonics. *Sci. Adv.* **2019**, *5*, 1–9.
10. Jørgensen, J. T.; Norregaard, K.; Tian, P.; Bendix, P. M.; Kjaer, A.; Oddershede, L. B. Single Particle and PET-based Platform for Identifying Optimal Plasmonic Nano-Heaters for Photothermal Cancer Therapy. *Sci. Rep.* **2016**, *6*,.
11. Emerich, D. F.; Thanos, C. G. The pinpoint promise of nanoparticle-based drug delivery and molecular diagnosis. *Biomolecular Engineering* **2006**, vol. 23 171–184.
12. Willets, K. A.; Van Duyne, R. P. Localized Surface Plasmon Resonance Spectroscopy and Sensing. *Annu. Rev. Phys. Chem.* **2007**, *58*, 267–297.
13. Fan, X.; Zheng, W.; Singh, D. J. Light scattering and surface plasmons on small spherical particles. *Light: Science and Applications* **2014**, vol. 3 e179–e179.
14. Guo, L.; Jackman, J. A.; Yang, H. H.; Chen, P.; Cho, N. J.; Kim, D. H. Strategies for enhancing the sensitivity of plasmonic nanosensors. *Nano Today* **2015**, vol. 10 213–239.
15. Nehl, C. L.; Hafner, J. H. Shape-dependent plasmon resonances of gold nanoparticles. *J. Mater. Chem.* **2008**, *18*, 2415–2419.
16. Samai, S.; Choi, T. L. Y.; Guye, K. N.; Yan, Y.; Ginger, D. S. Plasmonic Nanoparticle Dimers with Reversibly Photoswitchable Interparticle Distances Linked by DNA. *J. Phys. Chem. C* **2018**, *122*, 13363–13370.
17. K. Jain, P.; Huang, W.; A. El-Sayed, M. On the Universal Scaling Behavior of the Distance Decay of Plasmon Coupling in Metal Nanoparticle Pairs: A Plasmon Ruler Equation. *Nano Lett.* **2007**, *7*, 2080–2088.
18. Marinica, D. C.; Kazansky, A. K.; Nordlander, P.; Aizpurua, ‖ J; Borisov, A. G. Quantum Plasmonics: Nonlinear Effects in the Field Enhancement of a Plasmonic Nanoparticle

Dimer. *Nano Lett* **2012**, *12*, 1333–1339.
19. Satapathy, S. S.; Bhol, P.; Chakkarambath, A.; Mohanta, J.; Samantaray, K.; Bhat, S. K.; Panda, S. K.; Mohanty, P. S.; Si, S. Thermo-responsive PNIPAM-metal hybrids: An efficient nanocatalyst for the reduction of 4-nitrophenol. *Appl. Surf. Sci.* **2017**, *420*, 753–763.
20. Zhou, P.; Jia, S.; Pan, D.; Wang, L.; Gao, J.; Lu, J.; Shi, J.; Tang, Z.; Liu, H. Reversible regulation of catalytic activity of gold nanoparticles with DNA nanomachines. *Sci. Rep.* **2015**, *5*, 1–7.
21. Yang, Z.; Pelton, M.; Bodnarchuk, M. I.; Kovalenko, M. V.; Waks, E. Spontaneous emission enhancement of colloidal perovskite nanocrystals by a photonic crystal cavity. *Appl. Phys. Lett.* **2017**, *111*,.
22. Thakkar, N.; Rea, M. T.; Smith, K. C.; Heylman, K. D.; Quillin, S. C.; Knapper, K. A.; Horak, E. H.; Masiello, D. J.; Goldsmith, R. H. Sculpting Fano Resonances to Control Photonic-Plasmonic Hybridization. *Nano Lett.* **2017**, *17*, 6927–6934.
23. Abraham, E.; Smith, S. D. Optical bistability and related devices. *Reports Prog. Phys.* **1982**, *45*, 815.
24. Qian, Z.; Ginger, D. S. Reversibly Reconfigurable Colloidal Plasmonic Nanomaterials. *J. Am. Chem. Soc.* **2017**, *139*, 5266–5276.
25. Ma, Y.; Sikdar, D.; Fedosyuk, A.; Velleman, L.; Zhao, M.; Tang, L.; Kornyshev, A. A.; Edel, J. B. Auxetic Thermoresponsive Nanoplasmonic Optical Switch. *ACS Appl. Mater. Interfaces* **2019**, *11*, 22754–22760.
26. Li, D.; Dong, Y.; Li, B.; Wu, Y.; Wang, K.; Zhang, S. Colorimetric sensor array with unmodified noble metal nanoparticles for naked-eye detection of proteins and bacteria. *Analyst* **2015**, *140*, 7672–7677.
27. Zheng, X.; Bian, Q.; Ye, C.; Wang, G. Visible light-, pH-, and cyclodextrin-responsive azobenzene functionalized polymeric nanoparticles. *Dye. Pigment.* **2019**, *162*, 599–605.
28. Klouda, L.; Mikos, A. G. Thermoresponsive hydrogels in biomedical applications. *Eur. J. Pharm. Biopharm.* **2008**, *68*, 34–45.
29. Ke, Y.; Yin, Y.; Zhang, Q.; Tan, Y.; Hu, P.; Wang, S.; Tang, Y.; Zhou, Y.; Wen, X.; Wu, S.; White, T. J.; Yin, J.; Peng, J.; Xiong, Q.; Zhao, D.; Long, Y. Adaptive Thermochromic Windows from Active Plasmonic Elastomers. *Joule* **2019**, *3*, 858–871.
30. Karg, M.; Hellweg, T. New 'smart' poly(NIPAM) microgels and nanoparticle microgel hybrids: Properties and advances in characterisation. *Current Opinion in Colloid and Interface Science* **2009**, vol. 14 438–450.
31. Lee, S. H.; Gupta, M. K.; Bang, J. B.; Bae, H.; Sung, H. J. Current progress in reactive oxygen species (ROS)-Responsive materials for biomedical applications. *Adv. Healthc. Mater.* **2013**, *2*, 908–915.
32. Filipcsei, G.; Csetneki, I.; Szilágyi, A.; Zrínyi, M. *Magnetic field-responsive smart polymer composites*. *Advances in Polymer Science* (Springer, Berlin, Heidelberg, 2007). vol. 206.
33. Swift, T.; Swanson, L.; Geoghegan, M.; Rimmer, S. The pH-responsive behaviour of poly(acrylic acid) in aqueous solution is dependent on molar mass. *Soft Matter* **2016**, *12*, 2542–2549.
34. Wu, S.; Butt, H. Solar-Thermal Energy Conversion and Storage Using Photoresponsive Azobenzene-Containing Polymers. *Macromol. Rapid Commun.* **2020**, *1900413*,.
35. Ding, T.; Valev, V. K.; Salmon, A. R.; Forman, C. J.; Smoukov, S. K.; Scherman, O. A.;

Frenkel, D.; Baumberg, J. J. Light-induced actuating nanotransducers. *Proc. Natl. Acad. Sci. U. S. A.* **2016**, *113*, 5503–5507.
36. Cormier, S.; Ding, T.; Turek, V.; Baumberg, J. J. Actuating Single Nano-Oscillators with Light. *Adv. Opt. Mater.* **2018**, *6*, 1701281.
37. Ding, T.; Rüttiger, C.; Zheng, X.; Benz, F.; Ohadi, H.; Vandenbosch, G. A. E.; Moshchalkov, V. V.; Gallei, M.; Baumberg, J. J. Fast Dynamic Color Switching in Temperature-Responsive Plasmonic Films. *Adv. Opt. Mater.* **2016**, *4*, 877–882.
38. Cormier, S.; Ding, T.; Turek, V.; Baumberg, J. J. Dynamic- and Light-Switchable Self-Assembled Plasmonic Metafilms. *Adv. Opt. Mater.* **2018**, *6*, 1800208.
39. Baffou, G.; Quidant, R. Thermo-plasmonics: Using metallic nanostructures as nano-sources of heat. *Laser Photonics Rev.* **2013**, *7*, 171–187.
40. Jauffred, L.; Samadi, A.; Klingberg, H.; Bendix, P. M.; Oddershede, L. B. Plasmonic Heating of Nanostructures. *Chem. Rev.* **2019**, *119*, 8087–8130.
41. Herzog, J. B.; Knight, M. W.; Natelson, D. Thermoplasmonics: Quantifying plasmonic heating in single nanowires. *Nano Lett.* **2014**, *14*, 499–503.
42. Abeyrathna, N.; Liao, Y. A Reversible Photoacid Functioning in PBS Buffer under Visible Light. *J. Am. Chem. Soc.* **2015**, *137*, 11282–11284.
43. N. Silverman, L.; B. Spry, D.; G. Boxer, S.; D. Fayer, M. Charge Transfer in Photoacids Observed by Stark Spectroscopy. *J. Phys. Chem. A* **2008**, *112*, 10244–10249.
44. Yucknovsky, A.; Mondal, S.; Burnstine-Townley, A.; Foqara, M.; Amdursky, N. Use of Photoacids and Photobases to Control Dynamic Self-Assembly of Gold Nanoparticles in Aqueous and Nonaqueous Solutions. *Nano Lett.* **2019**, *19*, 3804–3810.
45. Hartley, G. S.; Le Fèvre, R. J. W. 119. The dipole moments of cis- and trans-azobenzenes and of some related compounds. *J. Chem. Soc.* **1939**, 531–535 doi:10.1039/JR9390000531.
46. Yan, Y.; Chen, J. I. L.; Ginger, D. S. Photoswitchable oligonucleotide-modified gold nanoparticles: Controlling hybridization stringency with photon dose. *Nano Lett.* **2012**, *12*, 2530–2536.
47. Yan, Y.; Wang, X.; Chen, J. I. L.; Ginger, D. S. Photoisomerization quantum yield of azobenzene-modified DNA depends on local sequence. *J. Am. Chem. Soc.* **2013**, *135*, 8382–8387.
48. Samai, S.; Bradley, D. J.; Choi, T. L. Y.; Yan, Y.; Ginger, D. S. Temperature-Dependent Photoisomerization Quantum Yields for Azobenzene-Modified DNA. *J. Phys. Chem. C* **2017**, *121*, 6997–7004.
49. Konrad, D. B.; Savasci, G.; Allmendinger, L.; Trauner, D.; Ochsenfeld, C.; Ali, A. M. Computational Design and Synthesis of a Deeply Red-Shifted and Bistable Azobenzene. *J. Am. Chem. Soc.* **2020**, *142*, 6538–6547.
50. Beharry, A. A.; Sadovski, O.; Woolley, G. A. Azobenzene Photoswitching without Ultraviolet Light. *J. Am. Chem. Soc.* **2011**, *133*, 19684–19687.
51. Weis, P.; Wang, D.; Wu, S. Visible-Light-Responsive Azopolymers with Inhibited π-π Stacking Enable Fully Reversible Photopatterning. *Macromolecules* **2016**, *49*, 6368–6373.
52. Zhao, Y.-L.; Stoddart, J. F. Azobenzene-Based Light-Responsive Hydrogel System. *Langmuir* **2009**, *25*, 8442–8446.
53. Tomatsu, I.; Hashidzume, A.; Harada, A. Photoresponsive Hydrogel System Using Molecular Recognition of a-Cyclodextrin. *Macromolecules* **2005**, *38*, 5223–5227.
54. Bortolus, P.; Monti, S. Cis ⇄ trans photoisomerization of azobenzene-cyclodextrin

inclusion complexes. *J. Phys. Chem.* **1987**, *91*, 5046–5050.
55. Zheng, P. J.; Wang, C.; Hu, X.; Tam, K. C.; Li, L. Supramolecular Complexes of Azocellulose and α-Cyclodextrin: Isothermal Titration Calorimetric and Spectroscopic Studies. *Macromolecules* **2005**, *38*, 2859–2864.
56. Wang, D.; Wagner, M.; Butt, H. J.; Wu, S. Supramolecular hydrogels constructed by red-light-responsive host-guest interactions for photo-controlled protein release in deep tissue. *Soft Matter* **2015**, *11*, 7656–7662.
57. Gao, Y.; Guo, R.; Feng, Y.; Zhang, L.; Wang, C.; Song, J.; Jiao, T.; Zhou, J.; Peng, Q. Self-Assembled Hydrogels Based on Poly-Cyclodextrin and Poly-Azobenzene Compounds and Applications for Highly Efficient Removal of Bisphenol A and Methylene Blue. *ACS Omega* **2018**, *3*, 11663–11672.
58. Reznikov, N.; Shahar, R.; Weiner, S. Bone hierarchical structure in three dimensions. *Acta Biomater.* **2014**, *10*, 3815–3826.
59. Tesson, B.; Hildebrand, M. Characterization and Localization of Insoluble Organic Matrices Associated with Diatom Cell Walls: Insight into Their Roles during Cell Wall Formation. *PLoS One* **2013**, *8*, 61675.
60. Huang, P. S.; Boyken, S. E.; Baker, D. The coming of age of de novo protein design. *Nature* **2016**, vol. 537 320–327.
61. Park, S. Y.; Lytton-Jean, A. K. R.; Lee, B.; Weigand, S.; Schatz, G. C.; Mirkin, C. A. DNA-programmable nanoparticle crystallization. *Nature* **2008**, *451*, 553–556.
62. Mirkin, C. A.; Letsinger, R. L.; Mucic, R. C.; Storhoff, J. J. A DNA-based method for rationally assembling nanoparticles into macroscopic materials. *Nature* **1996**, *382*, 607–609.
63. Girard, M.; Wang, S.; Du, J. S.; Das, A.; Huang, Z.; Dravid, V. P.; Lee, B.; Mirkin, C. A.; de la Cruz, M. O. Particle analogs of electrons in colloidal crystals. *Science* **2019**, *364*, 1174–1178.
64. Zhang, C.; MacFarlane, R. J.; Young, K. L.; Choi, C. H. J.; Hao, L.; Auyeung, E.; Liu, G.; Zhou, X.; Mirkin, C. A. A general approach to DNA-programmable atom equivalents. *Nat. Mater.* **2013**, *12*, 741–746.
65. Macfarlane, R. J.; Lee, B.; Jones, M. R.; Harris, N.; Schatz, G. C.; Mirkin, C. A. Nanoparticle superlattice engineering with DNA. *Science* **2011**, *334*, 204–208.
66. Jones, M. R.; MacFarlane, R. J.; Lee, B.; Zhang, J.; Young, K. L.; Senesi, A. J.; Mirkin, C. A. DNA-nanoparticle superlattices formed from anisotropic building blocks. *Nat. Mater.* **2010**, *9*, 913–917.
67. Zhu, J.; Lin, H.; Kim, Y.; Yang, M.; Skakuj, K.; Du, J. S.; Lee, B.; Schatz, G. C.; Van Duyne, R. P.; Mirkin, C. A. Light-Responsive Colloidal Crystals Engineered with DNA. *Adv. Mater.* **2020**, *32*, 1906600.
68. Dey, S.; Fan, C.; Gothelf, K. V.; Li, J.; Lin, C.; Liu, L.; Liu, N.; Nijenhuis, M. A. D.; Saccà, B.; Simmel, F. C.; Yan, H.; Zhan, P. DNA origami. *Nat. Rev. Methods Prim.* **2021**, *1*, 1–24.
69. Hong, F.; Zhang, F.; Liu, Y.; Yan, H. DNA Origami: Scaffolds for Creating Higher Order Structures. *Chem. Rev.* **2017**, *117*, 12584–12640.
70. Lewis, D. J.; Gabrys, P. A.; Macfarlane, R. J. DNA-Directed Non-Langmuir Deposition of Programmable Atom Equivalents. *Langmuir* **2018**, *34*, 14842–14850.
71. D. Merg, A.; C. Boatz, J.; Mandal, A.; Zhao, G.; Mokashi-Punekar, S.; Liu, C.; Wang, X.; Zhang, P.; C. A. van der Wel, P.; L. Rosi, N. Peptide-Directed Assembly of Single-Helical

Gold Nanoparticle Superstructures Exhibiting Intense Chiroptical Activity. *J. Am. Chem. Soc.* **2016**, *138*, 13655–13663.
72. Mokashi-Punekar, S.; Brooks, S. C.; Hogan, C. D.; Rosi, N. L. Leveraging Peptide Sequence Modification to Promote Assembly of Chiral Helical Gold Nanoparticle Superstructures. *Biochemistry* **2021**, *60*, 1044–1049.
73. Mokashi-Punekar, S.; Walsh, T. R.; Rosi, N. L. Tuning the Structure and Chiroptical Properties of Gold Nanoparticle Single Helices via Peptide Sequence Variation. *J. Am. Chem. Soc.* **2019**, *141*, 15710–15716.
74. Lee, H. E.; Ahn, H. Y.; Mun, J.; Lee, Y. Y.; Kim, M.; Cho, N. H.; Chang, K.; Kim, W. S.; Rho, J.; Nam, K. T. Amino-acid- and peptide-directed synthesis of chiral plasmonic gold nanoparticles. *Nature* **2018**, *556*, 360–364.
75. Yan, F.; Liu, L.; Walsh, T. R.; Gong, Y.; El-Khoury, P. Z.; Zhang, Y.; Zhu, Z.; De Yoreo, J. J.; Engelhard, M. H.; Zhang, X.; Chen, C. L. Controlled synthesis of highly-branched plasmonic gold nanoparticles through peptoid engineering. *Nat. Commun.* **2018**, *9*, 1–8.
76. Liu, J.; Cai, B.; Cui, L.; Chen, C. L. Peptoid-based hierarchically-structured biomimetic nanomaterials: Synthesis, characterization and applications. *Science China Materials* **2020**, vol. 63 1099–1112.
77. Jin, H.; Ding, Y. H.; Wang, M.; Song, Y.; Liao, Z.; Newcomb, C. J.; Wu, X.; Tang, X. Q.; Li, Z.; Lin, Y.; Yan, F.; Jian, T.; Mu, P.; Chen, C. L. Designable and dynamic single-walled stiff nanotubes assembled from sequence-defined peptoids. *Nat. Commun.* **2018**, *9*, 1–11.
78. Zhang, S.; Alberstein, R. G.; De Yoreo, J. J.; Tezcan, F. A. Assembly of a patchy protein into variable 2D lattices via tunable multiscale interactions. *Nat. Commun.* **2020**, *11*, 1–12.
79. Suzuki, Y.; Cardone, G.; Restrepo, D.; Zavattieri, P. D.; Baker, T. S.; Tezcan, F. A. Self-assembly of coherently dynamic, auxetic, two-dimensional protein crystals. *Nature* **2016**, *533*, 369–373.
80. Shen, H.; Fallas, J. A.; Lynch, E.; Sheffler, W.; Parry, B.; Jannetty, N.; Decarreau, J.; Wagenbach, M.; Vicente, J. J.; Chen, J.; Wang, L.; Dowling, Q.; Oberdorfer, G.; Stewart, L.; Wordeman, L.; De Yoreo, J.; Jacobs-Wagner, C.; Kollman, J.; Baker, D. De novo design of self-assembling helical protein filaments. *Science* **2018**, *362*, 705–709.
81. Cao, L.; Goreshnik, I.; Coventry, B.; Case, J. B.; Miller, L.; Kozodoy, L.; Chen, R. E.; Carter, L.; Walls, A. C.; Park, Y. J.; Strauch, E. M.; Stewart, L.; Diamond, M. S.; Veesler, D.; Baker, D. De novo design of picomolar SARS-CoV-2 miniprotein inhibitors. *Science* **2020**, *370*, 426–431.
82. Vorobieva, A. A.; White, P.; Liang, B.; Horne, J. E.; Bera, A. K.; Chow, C. M.; Gerben, S.; Marx, S.; Kang, A.; Stiving, A. Q.; Harvey, S. R.; Marx, D. C.; Nasir Khan, G.; Fleming, K. G.; Wysocki, V. H.; Brockwell, D. J.; Tamm, L. K.; Radford, S. E.; Baker, D. De novo design of transmembrane β barrels. *Science* **2021**, *371*,.
83. Quijano-Rubio, A.; Yeh, H. W.; Park, J.; Lee, H.; Langan, R. A.; Boyken, S. E.; Lajoie, M. J.; Cao, L.; Chow, C. M.; Miranda, M. C.; Wi, J.; Hong, H. J.; Stewart, L.; Oh, B. H.; Baker, D. De novo design of modular and tunable protein biosensors. *Nature* **2021**, *591*, 482–487.
84. Boyken, S. E.; Benhaim, M. A.; Busch, F.; Jia, M.; Bick, M. J.; Choi, H.; Klima, J. C.; Chen, Z.; Walkey, C.; Mileant, A.; Sahasrabuddhe, A.; Wei, K. Y.; Hodge, E. A.; Byron, S.; Quijano-Rubio, A.; Sankaran, B.; King, N. P.; Lippincott-Schwartz, J.; Wysocki, V. H.; Lee, K. K.; Baker, D. De novo design of tunable, pH-driven conformational changes. *Science* **2019**, *364*, 658–664.

Chapter 2. FINITE-DIFFERENCE TIME-DOMAIN MODELING OF PLASMONIC NANOPARTICLES

2.1 OVERVIEW

In this chapter, we use finite-difference time-domain (FDTD) simulations for plasmonic metal nanoparticles of varying shapes, sizes, metal types, and orientation in simple and complex media for supporting experimental observations when experiments are obtainable and predicting optical properties when such experiments are not possible. We compare the plasmonic resonance coupling efficiency of silver nanoprisms with different orientations with respect to one another and to the coupling efficiency of gold nanospheres to justify the novel emerging infrared scattering of silver nanoprisms anchored to the thermoresponsive polymer, poly(N-isopropylacrylamide) (PNIPAM). Then the absorption, scattering, and extinction spectra of gold nanorods of varying aspect ratios are simulated and compared to the UV-Visible (UV-Vis) extinction and photoacoustic absorption spectra of the nanoparticle solution. Lastly, we simulate the scattering and absorption spectra of excitonic 2D butylammonium lead iodide ($(C_4H_9NH_3)_2PbI_4$, BAPI) thin films and independent grains, plasmonic silver nanoprisms in a heterogeneous refractive index environment, and the exciton-photon, silver nanoprism-BAPI coupled system to justify experimentally-observed coupling scattering spectra from individual silver nanoprisms, to compare simulated and measured Rabi splitting values, and to show unmeasurable splitting in the nanoparticle absorption peaks, indicative of a strongly-coupled system.

2.2 Introduction to Finite-Difference Time-Domain Simulations

Plasmonic metal nanoparticles have long been the focus of many studies for use in applications such as sensing,[1,2] labelling,[3,4] chemical catalysis,[5–7] and electric field enhancement[8,9] due to their unique ability to focus light beneath the diffraction limit, characteristic large extinction coefficients with narrow scattering and absorption linewidths, and exceptional refractive index sensitivities. When multiple nanoparticles are brought together within close proximity, usually when the interparticle spacing is within the length of a nanoparticle's diameter, the plasmon modes couple to generate additional coupled plasmon resonances[10] and an increase in the extinction coefficient and electric field enhancement.[11,12] Such environmental variances yield notable and predictable effects on the absorption and scattering resonances, often measurable by simple UV-Vis extinction spectroscopy and predicted by models such as the plasmon ruler equation,[10] linear refractive index sensitivity,[13] or coupled oscillator models.[14–17] Such models, however, tend to either be most-suitable for simple isotropic particles in a homogenous refractive index environment or based on experimentally-determined variables which must be characterized prior to performing useful calculations.

Finite-difference time-domain (FDTD) simulations provide a convenient solution for overcoming many of these obstacles, predicting the optical characteristics of a sample with only a few, fundamental optical properties of the materials, and knowledge of the three-dimensional geometry of the system. To do so, the FDTD method solves Maxwell's equations for the electric and magnetic fields, the E-field and H-field respectively, across all space within the simulation area by smaller, discretized unit cells.[18] More specifically, for non-magnetic materials, FDTD solves Maxwell's curl equations[19]:

$$\frac{\partial \vec{D}}{\partial t} = \nabla \times \vec{H} \quad (2.2.1)$$

$$\vec{D}(\omega) = \varepsilon_0 \varepsilon_r(\omega) \vec{E}(\omega) \quad (2.2.2)$$

$$\frac{\partial \vec{H}}{\partial t} = -\frac{1}{\mu_0} \nabla \times \vec{E} \quad (2.2.3)$$

Where H is the magnetic field, E is the electric field, and D is the displacement field. $\varepsilon_r(\omega)$ is the complex relative dielectric constant. By making the following assumptions:

$$\varepsilon_r(\omega, x, y, z) = \varepsilon_r(\omega, x, y) \quad (2.2.4)$$

$$\frac{\partial \vec{E}}{\partial z} = \frac{\partial \vec{H}}{\partial z} = 0 \quad (2.2.5)$$

Then Maxwell's equations are separated into two set of equations, containing vector quantities each. The transverse electric (TE) comprised of E_x, E_y, and H_z and the transverse magnetic (TM) comprised of H_x, H_y, and E_z, resulting in a solution in only the x-y plane.

Some drawbacks to FDTD modeling is that due to the discretized mechanism of simulation, structures with significant complexity or those that are drawn to a sharp point are difficult to resolve, often requiring extremely small mesh to prevent simulation error. To make the mesh an order of x smaller, however, is to increase the simulation time by an order of 4^x, due to the four dimensions of x, y, z, and time handled by the simulation method. As a result, users commonly are required to find a balance between accuracy of results and computational cost. Nevertheless, the FDTD method is remarkable for its ability to handle three-dimensional systems containing a variety of dielectric materials of different geometries and field interactions. Often computational cost can be overcome by a physical understanding of the desired system and the flexibility of the simulation to adjust for regions of importance.

FDTD simulations have become a staple in the plasmonics publishing community, alongside discrete-dipole approximations and the plasmon ruler, providing reliable and informative insight about the optical properties of the simulated system, supporting experimental observations[20] and theoretical predictions.[21]

REFERENCES

1. Giannini, V.; Fernández-Domínguez, A. I.; Heck, S. C.; Maier, S. A. Plasmonic nanoantennas: Fundamentals and their use in controlling the radiative properties of nanoemitters. *Chemical Reviews* **2011**, vol. 111 3888–3912.
2. Willets, K. A.; Van Duyne, R. P. Localized Surface Plasmon Resonance Spectroscopy and Sensing. *Annu. Rev. Phys. Chem.* **2007**, *58*, 267–297.
3. Mayer, K. M.; Lee, S.; Liao, H.; Rostro, B. C.; Fuentes, A.; Scully, P. T.; Nehl, C. L.; Hafner, J. H. A label-free immunoassay based upon localized surface plasmon resonance of gold nanorods. *ACS Nano* **2008**, *2*, 687–692.
4. Stuart, D. A.; Haes, A. J.; Yonzon, C. R.; Hicks, E. M.; Van Duyne, R. P. Biological applications of localised surface plasmonic phenomenae. *IEE Proceedings Nanobiotechnology* **2005**, vol. 152 13–32.
5. Rossi, L. M.; Fiorio, J. L.; Garcia, M. A. S.; Ferraz, C. P. The role and fate of capping ligands in colloidally prepared metal nanoparticle catalysts. *Dalt. Trans.* **2018**, *47*, 5889–5915.
6. Zhou, P.; Jia, S.; Pan, D.; Wang, L.; Gao, J.; Lu, J.; Shi, J.; Tang, Z.; Liu, H. Reversible regulation of catalytic activity of gold nanoparticles with DNA nanomachines. *Sci. Rep.* **2015**, *5*, 1–7.
7. Satapathy, S. S.; Bhol, P.; Chakkarambath, A.; Mohanta, J.; Samantaray, K.; Bhat, S. K.; Panda, S. K.; Mohanty, P. S.; Si, S. Thermo-responsive PNIPAM-metal hybrids: An efficient nanocatalyst for the reduction of 4-nitrophenol. *Appl. Surf. Sci.* **2017**, *420*, 753–763.
8. HA Atwater, A. P. Plasmonics for improved photovoltaic devices. *Nat. Mater.* **2010**, *9*, 205–213.
9. Munechika, K.; Chen, Y.; Tillack, A. F.; Kulkarni, A. P.; Plante, I. J. La; Munro, A. M.; Ginger, D. S. Spectral control of plasmonic emission enhancement from quantum dots near single silver nanoprisms. *Nano Lett.* **2010**, *10*, 2598–2603.
10. K. Jain, P.; Huang, W.; A. El-Sayed, M. On the Universal Scaling Behavior of the Distance Decay of Plasmon Coupling in Metal Nanoparticle Pairs: A Plasmon Ruler Equation. *Nano Lett.* **2007**, *7*, 2080–2088.
11. Chen, Y.; Munechika, K.; Jen-La Plante, I.; Munro, A. M.; Skrabalak, S. E.; Xia, Y.; Ginger, D. S. Excitation enhancement of CdSe quantum dots by single metal nanoparticles. *Appl. Phys. Lett.* **2008**, *93*, 053106.
12. Rosen, D. A.; Tao, A. R. Modeling the optical properties of bowtie antenna generated by self-assembled Ag triangular nanoprisms. *ACS Appl. Mater. Interfaces* **2014**, *6*, 4134–4142.
13. Piliarik, M.; Kvasnička, P.; Galler, N.; Krenn, J. R.; Homola, J. *Local refractive index sensitivity of plasmonic nanoparticles*. (2011).
14. Limonov, M. F.; Rybin, M. V.; Poddubny, A. N.; Kivshar, Y. S. Fano resonances in photonics. *Nat. Photonics* **2017**, *11*, 543–554.
15. Thakkar, N.; Rea, M. T.; Smith, K. C.; Heylman, K. D.; Quillin, S. C.; Knapper, K. A.; Horak, E. H.; Masiello, D. J.; Goldsmith, R. H. Sculpting Fano Resonances to Control Photonic-Plasmonic Hybridization. *Nano Lett.* **2017**, *17*, 6927–6934.
16. Wu, X.; Gray, S. K.; Pelton, M. Quantum-dot-induced transparency in a nanoscale plasmonic resonator. *Opt. Express* **2010**, *18*, 23633.

17. Zengin, G.; Johansson, G.; Johansson, P.; Antosiewicz, T. J.; Käll, M.; Shegai, T. Approaching the strong coupling limit in single plasmonic nanorods interacting with J-aggregates. *Sci. Rep.* **2013**, *3*, 3074.
18. Gedney, S. D. Introduction to the Finite-Difference Time-Domain (FDTD)) method for electromagnetics. *Synth. Lect. Comput. Electromagn.* **2011**, *27*, 1–250.
19. Finite Difference Time Domain (FDTD) solver introduction – Lumerical Support. https://support.lumerical.com/hc/en-us/articles/360034914633-Finite-Difference-Time-Domain-FDTD-solver-introduction.
20. Pelivanov, I.; Petrova, E.; Yoon, S. J.; Qian, Z.; Guye, K.; O'Donnell, M. Molecular fingerprinting of nanoparticles in complex media with non-contact photoacoustics: beyond the light scattering limit. *Sci. Rep.* **2018**, *8*, 1–13.
21. Hoggard, A.; Wang, L. Y.; Ma, L.; Fang, Y.; You, G.; Olson, J.; Liu, Z.; Chang, W. S.; Ajayan, P. M.; Link, S. Using the plasmon linewidth to calculate the time and efficiency of electron transfer between gold nanorods and graphene. *ACS Nano* **2013**, *7*, 11209–11217.

2.3 THEORETICAL MODELING OF PLASMONIC COUPLING OF ANISOTROPIC SILVER NANOPRISMS WITH VARYING INTERPARTICLE DISTANCES AND ORIENTATIONS

*This section is reproduced in part with permission from "Optical Properties of Reconfigurable Polymer/Silver Nanoprism Hybrids: Tunable Color and Infrared Scattering Contrast" Soumyadyuti Samai, Zhaoxia Qian, Jian Ling, Kathryn N. Guye, David S. Ginger, Applied Materials and Interfaces **2018**, 10, 10, 8976-8984. Copyright 2018 American Chemical Society.*

2.3.1 INTRODUCTION

Recently, combining inorganic plasmonic nanoparticles with stimulus-responsive organic materials has drawn notable focus for the design, synthesis, and characterization of reversibly reconfigurable composite materials for potential applications in sensing,[1–3] catalysis,[4–6] drug delivery,[7–9] and photonics.[10,11] Due to an external stimulus such as light, heat, or a change in pH, a molecular switch is activated resulting in some physical structural change to an organic functional material.[12,13] When plasmonic nanoparticles are complexed to such materials, the structural transitions reversibly changes the interparticle distance.[14,15] The degree of plasmonic coupling between two nanoparticles in proximity is interparticle distance-dependent, and can easily be characterized by the redshift of the localized surface plasmon resonance (LSPR).[16] Depending on the organic scaffold, the stimulus-induced transition between the two structural states can either be a discrete, binary state jump[17] or a gradual change with the ability to access intermediate structures.[18] Poly(N-isopropylacrylamide) (PNIPAM) is one such polymeric scaffold which has been the subject of intense focus for its temperature-dependent coil-to-globule transition due to a hydrophilic-to-hydrophobic phase transition at its lower critical solution temperature

(LCST)[19]. Its popularity has been due to several factors favorable to different areas of study including a simple monomer-to-polymer synthesis, thermal cycling stability, facile copolymerization for a dual-stimulus response, and an LCST within a few degrees of physiological temperature (37°C).[20–22]

In aqueous solution, the coil-to-globule transition of PNIPAM results in a drastic decrease in the hydrodynamic diameter of the polymer above the LCST. This temperature-induced transition proceeds as a sigmoidal deswelling of the polymer as it reorganizes to reduce its contact with water molecules, with the ability to access intermediate hydrodynamic diameters at intermediate temperatures.[18,21] As such, PNIPAM/plasmonic nanoparticle composites were quickly identified for stimulus-responsive composite materials with dynamically-controllable interparticle spacing. It has been shown that the functionalization of gold nanoparticles with PNIPAM single-chain and crosslinked structures yield a redshift of the LSPR due to both the 1.32 to 1.39 refractive index increase[23] and reversible aggregation of nanoparticles as the PNIPAM undergoes hydrophilic-to-hydrophobic transitions. Baumberg and coworkers have extensively demonstrated PNIPAM-functionalized nanoparticles on a gold mirror as powerful nanoactuators driven by both external and plasmonic photothermal heating.[24–26] PNIPAM can also be crosslinked into hydrogel microspheres with sub-LCST diameters of several hundred nanometers and super-LCST deswelling of over 50%. Such microspheres can then be decorated with plasmonic nanoparticles at its surface, yielding strong thermally-driven and reversible plasmonic coupling between particles without particle aggregation. In 2017, Qian et al.[18] demonstrated even sparse loading of only a few nanoparticles onto PNIPAM hydrogels could yield large shifts in the extinction spectra of over 150 nm for PNIPAM-gold nanoparticle hybrids.[27] In this work, they showed by a series of finite-difference time-domain (FDTD) simulations that there was 1) redistribution of nanoparticles

within the hydrosphere during the first thermal cycle, 2) plasmonic coupling with sparse loading comparable to the experimentally observed LSPR shift, and 3) the redshift of the plasmon resonance was due to plasmonic coupling and not the increase of refractive index alone.

While much work on hybrid composites has been performed using gold nanoparticles due to gold's stability and durability, particularly with fluctuating environmental conditions, silver nanoparticles, however, offer stronger plasmonic coupling,[28] refractive index sensitivity,[29] and a broader range of vibrant scattered light in the visible region as the interband transition of silver does not overlap the visible region as it does for gold, resulting in only the LSPR extinction to influence the perceived color of solution.[30] Additionally, silver's reactivity has enabled researchers to readily design synthetic strategies for silver nanoparticles of varying shapes such as nanoprisms,[31] increasing electric field enhancement and nanoparticle coupling between sharper features on a nanoparticle compared to the smooth curve of a nanosphere. Such properties make silver nanoparticles, and in particular silver nanoprisms, an attractive target for combining with the thermoresponsive functional materials for enhanced hybrid properties.

In this work, Samai et al. prepared PNIPAM-silver nanoprism hybrids using a PNIPAM microsphere as the stimulus-responsive scaffold, yielding thermochromic shifts 5-10 times larger than what had been reported in the literature.[32–34] Intriguingly, for the first time with PNIPAM-nanoparticle hybrids, the redshift in extinction was so great in the super-LCST deswelled state that infrared light scattering was observed, suggesting potential applications for infrared imaging or climate control technologies.

In the work presented here, we perform a series of FDTD simulations of gold nanosphere and silver nanoprism dimers, with the nanoprisms in varying orientations with respect to one another. We then decrease the interparticle spacing, resulting in increased nanoparticle coupling and

redshifted extinction, and compare these results with the simulations of Qian et al.[18] to show that this large >180 nm LSPR redshift was the result of decreased interparticle spacing between the swelled and deswelled state of the PNIPAM microsphere.

2.3.2 Results and Discussion

The redshift of plasmon resonances due to particle-particle coupling can be predictably calculated as a function of particle size and interparticle spacing by the plasmon ruler equation as described by Jain et al.[16] and shown in Eqn. 2.3.2.1.:

$$\frac{\Delta\lambda}{\lambda_0} = A * exp\left(\frac{-\frac{s}{D}}{\tau}\right) \qquad (2.3.2.1)$$

Where $\Delta\lambda/\lambda_0$ is the fractional plasmon resonance shift, A is the amplitude related to the refractive index, s is the surface-to-surface interparticle spacing, D is the nanoparticle diameter, and τ is the decay constant also related to the local refractive index. This model, however, is optimal for isotropic nanoparticles and does not take into account the varying orientations with respect to one another for anisotropic nanoparticle dimers by the individual dimer.

With average nanoparticle loading densities up to ~120 particles/microsphere, we chose not to simulate a whole PNIPAM microsphere with silver nanorprisms as Qian et al. had for the sparsely-loaded hybrids. Instead, using FDTD simulations as shown in **Figure 2.3.2.1**, we predict the plasmon ruler model for gold nanosphere and silver nanoprisms in varying orientations under a low refractive index (n =1), to show even under conditions which reduce particle-particle coupling, silver nanoprisms at any given interparticle distance will exhibit a larger redshift of the plasmon resonance.

In this study, we use two samples of nanoprisms. The first sample had an average edge length of 30 ± 5 nm with a thickness of 8 ± 2 nm with an LSPR in the range of 474-480 nm. The second sample and an average edge length of 55 ± 14 nm. Recalling Eqn. 2.3.2.1, the plasmon ruler equation, the fractional plasmon resonance redshift is exponentially inversely proportional to the effective diameter of the nanoparticle. Therefore, the second sample with the larger nanoparticle is expected to display a smaller fractional redshift in the plasmon resonance. This prediction is consistent with the numerical simulations which reveal the smaller nanoparticles in the first sample redshift almost twice as far at some distances compared to the second sample. This was consistent as well with experimental observations that smaller nanoparticles resulted in a much larger redshift than larger nanoparticles, even independent from loading density (Appendix A).

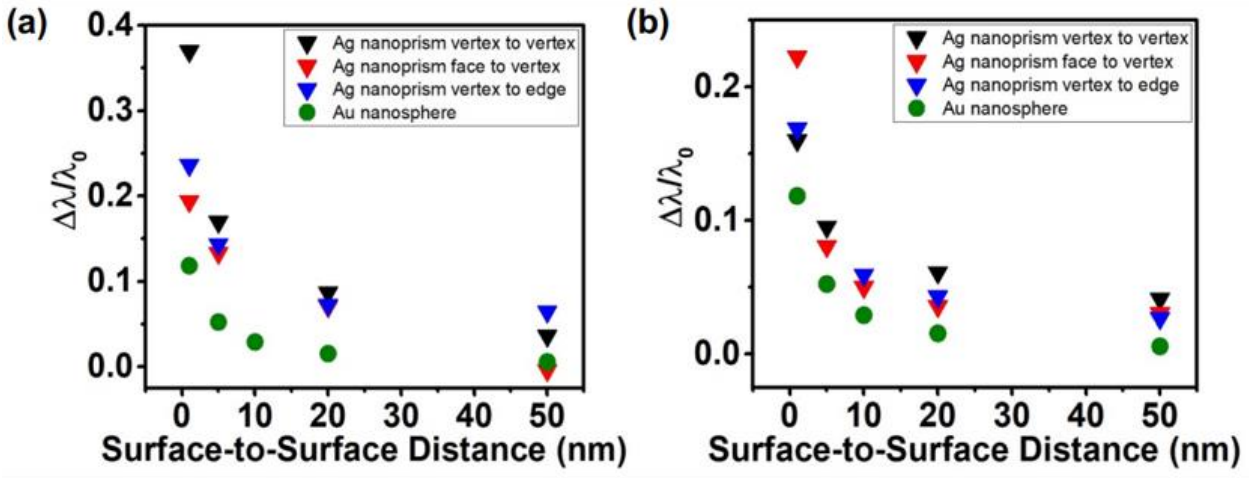

Figure 2.3.2.1. Fractional redshift of a) silver nanoparticle sample 1 and b) silver nanoparticle sample 2 as a function of surface-to-surface interparticle distance. Anisotropic silver nanoparticles are shown with varying orientations with respect to one another including vertex to vertex (black triangle), face to vertex (red triangle), and vertex to edge (blue triangle), and then compared to the fractional shift of isotropic gold nanoparticles (green circles).

It is also important to take into consideration the geometric difference between isotropic nanospheres and anisotropic nanoprisms. The magnitude of coupling between two nanoparticles is both dependent on the shape of the nanoparticle and orientation of particles with respect to one

another.[35–37] As such, we simulate a variety of interparticle geometries with consideration that nanoparticles complexed to the surface of the PNIPAM microsphere are free to attach with random rotation, and potential movement throughout the sphere as indicated in the previous study by Qian et al. The three orientations chosen were a vertex-to-vertex, vertex-to-face, and vertex-to-edge of the nanoprisms, with the total-field scatter field electric field polarization of light in the simulation parallel to the first nanoprism vertex-to-opposite edge axis (Appendix A).

Comparing these simulations to those performed by Qian et al., we come to the same conclusion that the >180 nm extinction spectrum redshift is due to plasmonic coupling as the result of deswelling of the PNIPAM microsphere, and that a larger redshift is consistent for silver nanoprisms compared to gold nanoparticles.

2.3.3 CONCLUSIONS

In this work, we simulated the plasmon redshift of several nanoparticle dimers with varying interparticle distances including isotropic gold nanospheres and anisotropic silver nanoprisms with various orientations. At any given interparticle separation, silver nanoprisms almost always display a greater fractional plasmon resonance redshift than do gold nanoparticles. Furthermore, as the interparticle separation decreases, silver nanoprisms display a greater relative redshift compared to the larger distances than do gold nanoparticles. With these simulations, compared to the simulations of Qian et al., we conclude the redshift observed in the experimental data in the main text of Samai et al. is due to significant reversible interparticle coupling.

2.3.4 METHODS

Synthesis of Silver Nanoprisms

Nanoprism-1 was prepared following previously reported methods.[38,39] Nanoprism-2 was prepared following methods reported by Xue and Mirkin[31], modified as follows. 2 mL of 5 mM AgNO3 solution and 1 mL of 30 mM sodium citrate solution were added to 95 mL of water in a 250 mL round-bottom flask placed in ice. The mixture was purged with nitrogen and stirred with a magnetic stirrer for 1 h. Then, 1.4 mL of freshly prepared ice-cold 50 mM NaBH4 solution was added in a stepwise manner to yield a pale-yellow solution, indicating the formation of spherical AgNPs. A few minutes later, a mixture containing 1 mL of 5 mM BSPP and 500 μL of the 50 mM $NaBH_4$ solution was gradually injected into the solution. After aging this precursor solution in the dark for 15 h, the pH of the solution was adjusted to 11.0, and the spherical silver particles were then photochemically converted into flat prisms by exposing the solution to a 590 nm LED (LED Engin, Inc.) for 24 h, after which the solution turned blue. We followed the same purification procedure as method 1 and redispersed the nanoprisms in a solution of 5 mM sodium citrate to store at 4 °C for future use. The resulting nanoprisms had an average edge length of 55 ± 14 nm and a thickness of 10 ± 2 nm and exhibited an absorbance of ∼3.1 at the LSPR peak near 570 nm. The absorbance value of the solution at 318 nm was measured to be in the range of 0.15–0.20.

Numerical Simulations

FDTD simulations were performed (Lumerical Solutions, Inc. – version 8.18) on nanoparticle dimers of silver nanoprisms and gold nanospheres with varying interparticle distances and relative orientations (Appendix A). The silver nanoprisms 1 and 2 were modeled as triangular prisms with edge lengths:widths of 30 nm:8 nm and 55 nm:10 nm respectively using the Palik (0-2 μm) dielectric fit for silver modeling[40,41]; the gold nanospheres were modeled as an isotropic sphere

with diameter of 50 nm using the Johnson and Christy dielectric fit for gold modeling.[42] The dimers were centered in a simulation box with an override mesh size of 0.6 nm for silver nanoprism-1 and 1 nm for silver nanoprism-2 and the gold nanosphere. The light source was a broadband total-field scatter-field source, with the k-vector perpendicular to the nanoparticle dimer and the E-vector parallel to the longitudinal axis of the dimer. The background index was set to 1 in order to avoid overestimating n, resulting in greater nanoparticle coupling and LSPR redshifting. The simulation box was build with perfectly matched layer boundaries to prevent back-scattering or reflection from the boundary. Frequency-domain field and power monitors were placed on the inside and outside of the source to determine the absorption and scattering, respectively. Fractional plasmon resonance shifts were calculated by comparing the extinction spectra of nanoparticle dimers to the simulated spectrum of a single nanoparticle. Interparticle separation was then varied for each dimer pair.

2.3.5 ACKNOWLEDGEMENTS

This publication is in part on work initially supported by AFOSR (FA9550-14-1-02509). Part of this work was conducted at the Molecular Analysis Facility, a National Nanotechnology Coordinated Infrastructure site at the University of Washington, which is supported in part by the National Science Foundation (grant ECC-1542101), the University of Washington, the Molecular Engineering & Sciences Institute, the Clean Energy Institute, and the National Institutes of Health. D.S.G. also acknowledges the Alvin L. and Verla R. Kwiram endowed fund and Washington Research Foundation for partial support. S.S. and Z.Q. also acknowledge Prof. Miqin Zhang and her group in the Department of Materials Science and Engineering, University of Washington, for the Malvern Zetasizer instrument used for all the dynamic light scattering measurements.

2.3.6 ABBREVIATIONS

FDTD, finite-difference time-domain; LCST, lower critical solution temperature; LSPR, localized surface plasmon resonance; PNIPAM, poly(N-isopropylacrylamide)

2.3.7 REFERENCES

1. Yan, Y.; Chen, J. I. L.; Ginger, D. S. Photoswitchable oligonucleotide-modified gold nanoparticles: Controlling hybridization stringency with photon dose. *Nano Lett.* **2012**, *12*, 2530–2536.
2. Joshi, G. K.; Blodgett, K. N.; Muhoberac, B. B.; Johnson, M. A.; Smith, K. A.; Sardar, R. Ultrasensitive photoreversible molecular sensors of azobenzene- functionalized plasmonic nanoantennas. *Nano Lett.* **2014**, *14*, 532–540.
3. Nam, J. M.; Park, S. J.; Mirkin, C. A. Bio-barcodes based on oligonucleotide-modified nanoparticles. *J. Am. Chem. Soc.* **2002**, *124*, 3820–3821.
4. Satapathy, S. S.; Bhol, P.; Chakkarambath, A.; Mohanta, J.; Samantaray, K.; Bhat, S. K.; Panda, S. K.; Mohanty, P. S.; Si, S. Thermo-responsive PNIPAM-metal hybrids: An efficient nanocatalyst for the reduction of 4-nitrophenol. *Appl. Surf. Sci.* **2017**, *420*, 753–763.
5. Pérez-Juste, J.; Pastoriza-Santos, I.; Liz-Marzán, L. M. Multifunctionality in metal@microgel colloidal nanocomposites. *J. Mater. Chem. A* **2013**, *1*, 20–26.
6. Zhou, P.; Jia, S.; Pan, D.; Wang, L.; Gao, J.; Lu, J.; Shi, J.; Tang, Z.; Liu, H. Reversible regulation of catalytic activity of gold nanoparticles with DNA nanomachines. *Sci. Rep.* **2015**, *5*, 1–7.
7. Mura, S.; Nicolas, J.; Couvreur, P. Stimuli-responsive nanocarriers for drug delivery. *Nat. Mater.* **2013**, *12*, 991–1003.
8. Karimi, M.; Sahandi Zangabad, P.; Ghasemi, A.; Amiri, M.; Bahrami, M.; Malekzad, H.; Ghahramanzadeh Asl, H.; Mahdieh, Z.; Bozorgomid, M.; Ghasemi, A.; Rahmani Taji Boyuk, M. R.; Hamblin, M. R. Temperature-Responsive Smart Nanocarriers for Delivery of Therapeutic Agents: Applications and Recent Advances. *ACS Appl. Mater. Interfaces* **2016**, *8*, 21107–21133.
9. Kang, H.; Trondoli, A. C.; Zhu, G.; Chen, Y.; Chang, Y. J.; Liu, H.; Huang, Y. F.; Zhang, X.; Tan, W. Near-infrared light-responsive core-shell nanogels for targeted drug delivery. *ACS Nano* **2011**, *5*, 5094–5099.
10. Schäfer, C. G.; Winter, T.; Heidt, S.; Dietz, C.; Ding, T.; Baumberg, J. J.; Gallei, M. Smart polymer inverse-opal photonic crystal films by melt-shear organization for hybrid core-shell architectures. *J. Mater. Chem. C* **2015**, *3*, 2204–2214.
11. Karg, M.; Hellweg, T.; Mulvaney, P. Self-assembly of tunable nanocrystal superlattices using poly-(NIPAM) spacers. *Adv. Funct. Mater.* **2011**, *21*, 4668–4676.
12. Pack, D. W.; Hoffman, A. S.; Pun, S.; Stayton, P. S. Design and development of polymers for gene delivery. *Nature Reviews Drug Discovery* **2005**, vol. 4 581–593.
13. Harris, J. D.; Moran, M. J.; Aprahamian, I. New molecular switch architectures. *Proc. Natl. Acad. Sci. U. S. A.* **2018**, *115*, 9414–9422.
14. Ding, T.; Rudrum, A. W.; Herrmann, L. O.; Turek, V.; Baumberg, J. J. Polymer-assisted self-assembly of gold nanoparticle monolayers and their dynamical switching. *Nanoscale* **2016**, *8*, 15864–15869.
15. Qian, Z.; Ginger, D. S. Reversibly Reconfigurable Colloidal Plasmonic Nanomaterials. *J. Am. Chem. Soc.* **2017**, *139*, 5266–5276.
16. K. Jain, P.; Huang, W.; A. El-Sayed, M. On the Universal Scaling Behavior of the Distance Decay of Plasmon Coupling in Metal Nanoparticle Pairs: A Plasmon Ruler Equation. *Nano*

Lett. **2007**, *7*, 2080–2088.
17. Samai, S.; Choi, T. L. Y.; Guye, K. N.; Yan, Y.; Ginger, D. S. Plasmonic Nanoparticle Dimers with Reversibly Photoswitchable Interparticle Distances Linked by DNA. *J. Phys. Chem. C* **2018**, *122*, 13363–13370.
18. Qian, Z.; Guye, K. N.; Masiello, D. J.; Ginger, D. S. Dynamic Optical Switching of Polymer/Plasmonic Nanoparticle Hybrids with Sparse Loading. *J. Phys. Chem. B* **2017**, *121*, 1092–1099.
19. Schild, H. G. Poly(N-isopropylacrylamide): experiment, theory and application. *Prog. Polym. Sci.* **1992**, *17*, 163–249.
20. Klouda, L.; Mikos, A. G. Thermoresponsive hydrogels in biomedical applications. *Eur. J. Pharm. Biopharm.* **2008**, *68*, 34–45.
21. Pelton, R. Temperature-sensitive aqueous microgels. *Adv. Colloid Interface Sci.* **2000**, *85*, 1–33.
22. Lim, S.; Song, J. E.; La, J. A.; Cho, E. C. Gold nanospheres assembled on hydrogel colloids display a wide range of thermoreversible changes in optical bandwidth for various plasmonic-based color switches. *Chem. Mater.* **2014**, *26*, 3272–3279.
23. Garner, B. W.; Cai, T.; Ghosh, S.; Hu, Z.; Neogi, A. Refractive index change due to volume-phase transition in polyacrylamide gel nanospheres for optoelectronics and bio-photonics. *Appl. Phys. Express* **2009**, *2*, 057001.
24. Ding, T.; Rüttiger, C.; Zheng, X.; Benz, F.; Ohadi, H.; Vandenbosch, G. A. E.; Moshchalkov, V. V.; Gallei, M.; Baumberg, J. J. Fast Dynamic Color Switching in Temperature-Responsive Plasmonic Films. *Adv. Opt. Mater.* **2016**, *4*, 877–882.
25. Cormier, S.; Ding, T.; Turek, V.; Baumberg, J. J. Dynamic- and Light-Switchable Self-Assembled Plasmonic Metafilms. *Adv. Opt. Mater.* **2018**, *6*, 1800208.
26. Cormier, S.; Ding, T.; Turek, V.; Baumberg, J. J. Actuating Single Nano-Oscillators with Light. *Adv. Opt. Mater.* **2018**, *6*, 1701281.
27. Qian, Z.; Guye, K. N.; Masiello, D. J.; Ginger, D. S. Dynamic Optical Switching of Polymer/Plasmonic Nanoparticle Hybrids with Sparse Loading. *J. Phys. Chem. B* **2017**, *121*,.
28. Sönnichsen, C.; Reinhard, B. M.; Liphardt, J.; Alivisatos, A. P. A molecular ruler based on plasmon coupling of single gold and silver nanoparticles. *Nat. Biotechnol.* **2005**, *23*, 741–745.
29. Lee, K. S.; El-Sayed, M. A. Gold and silver nanoparticles in sensing and imaging: Sensitivity of plasmon response to size, shape, and metal composition. *J. Phys. Chem. B* **2006**, *110*, 19220–19225.
30. Kolwas, K.; Derkachova, A. Impact of the interband transitions in gold and silver on the dynamics of propagating and localized surface plasmons. *Nanomaterials* **2020**, *10*, 1–27.
31. Xue, C.; Mirkin, C. A. pH-switchable silver nanoprism growth pathways. *Angew. Chemie - Int. Ed.* **2007**, *46*, 2036–2038.
32. Liu, Y. Y.; Liu, X. Y.; Yang, J. M.; Lin, D. L.; Chen, X.; Zha, L. S. Investigation of Ag nanoparticles loading temperature responsive hybrid microgels and their temperature controlled catalytic activity. *Colloids Surfaces A Physicochem. Eng. Asp.* **2012**, *393*, 105–110.
33. Dong, Y.; Ma, Y.; Zhai, T.; Shen, F.; Zeng, Y.; Fu, H.; Yao, J. Silver nanoparticles stabilized by thermoresponsive microgel particles: Synthesis and evidence of an electron donor-

acceptor effecta. *Macromol. Rapid Commun.* **2007**, *28*, 2339–2345.
34. Liu, X.; Wang, X.; Zha, L.; Lin, D.; Yang, J.; Zhou, J.; Zhang, L. Temperature- and pH-tunable plasmonic properties and SERS efficiency of the silver nanoparticles within the dual stimuli-responsive microgels. *J. Mater. Chem. C* **2014**, *2*, 7326–7335.
35. Hua, Y.; Chandra, K.; Hieu, D.; Dam, M.; Wiederrecht, G. P.; Odom, T. W. Shape-Dependent Nonlinear Optical Properties of Anisotropic Gold Nanoparticles. *J. Phys. Chem. Lett* **2015**, *6*, 4908.
36. Chien, M. H.; Nien, L. W.; Chao, B. K.; Li, J. H.; Hsueh, C. H. Effects of the rotation angle on surface plasmon coupling of nanoprisms. *Nanoscale* **2016**, *8*, 3660–3670.
37. Cortés, E.; Xie, W.; Cambiasso, J.; Jermyn, A. S.; Sundararaman, R.; Narang, P.; Schlücker, S.; Maier, S. A. Plasmonic hot electron transport drives nano-localized chemistry. *Nat. Commun.* **2017**, *8*, 1–10.
38. Métraux, G. S.; Mirkin, C. A. Rapid thermal synthesis of silver nanoprisms with chemically tailorable thickness. *Adv. Mater.* **2005**, *17*, 412–415.
39. Wang, H.; Cui, X.; Guan, W.; Zheng, X.; Zhao, H.; Wang, Z.; Wang, Q.; Xue, T.; Liu, C.; Singh, D. J.; Zheng, W. Kinetic effects in the photomediated synthesis of silver nanodecahedra and nanoprisms: Combined effect of wavelength and temperature. *Nanoscale* **2014**, *6*, 7295–7302.
40. *Handbook of Optical Constants of Solids - 1st Edition*. (Academic Press, 1985). vol. 1.
41. Munechika, K.; Smith, J. M.; Chen, Y.; Ginger, D. S. Plasmon line widths of single silver nanoprisms as a function of particle size and plasmon peak position. *J. Phys. Chem. C* **2007**, *111*, 18906–18911.
42. Johnson, P. B.; Christy, R. W. Optical constants of the noble metals. *Phys. Rev. B* **1972**, *6*, 4370–4379.

2.4 Theoretical Modeling of Size-Dependent Absorption and Scattering of Gold Nanorods in Comparison with Photoacoustic Spectroscopy

This section is adapted with modification with permission from the original publication "Molecular fingerprinting of nanoparticles in complex media with non-contact photoacoustics: beyond the light scattering limit" Ivan Pelivanov, Elena Petrova, Soon Joon Yoon, Zhaoxia Qian, Kathryn N. Guye, Matthew O'Donnell, Scientific Reports ***2018****, 8, 14425.*

2.4.1 INTRODUCTION

Due to their nanoscale size, large extinction cross section,[1,2] and, in the case of gold nanorods, a plasmon resonance in the near-IR water window,[3] such nanoparticles provide an excellent opportunity for *in situ* microscopic imaging and spectroscopy of cells and cellular functions.[4–11] The typical UV-Vis extinction experiment, however, while it would potentially yield valuable information about nanoparticle spacing or local refractive indices to establish position or functionalization of the nanoparticles, is often unable to accomplish such measurements due to the large scattering cross section of not only the nanoparticles, but also of the complex aqueous media of the cellular solution.[12–14] Because extinction is defined as the attenuation of light by all possible mechanisms including absorption, scattering, and reflectance, the diagnostic information given by the transmutation of the plasmonic signature is obscured by additional scattering. One such solution to this dilemma is by photoacoustic absorption (PA) spectroscopy.[15] PA spectroscopy uses an incident laser resonant with the gold nanoparticles, leading to photothermal heating of the nanoparticle. A probe beam then passes through the solution, and the deflection of the probe beam due to local temperature gradients is recorded.[16,17] The magnitude of the beam deflection can then be correlated to the magnitude of light absorption by the nanoparticles. Only absorbed light leads

to photothermal heating,[18] and therefore, this system isolates the absorption signature and is unperturbed by scattering or reflection. Traditional PA spectroscopy, however, does have its limitations. Although scattering by the nanoparticles will not be measured by temperature-dependent beam deflection, a highly scattering system (e.g. a concentrated solution of nanoparticles) can scatter the probe beam and obscure the measurement. Therefore, usually only very dilute samples of nanoparticles or low-scattering solutions can be effectively used with PA spectroscopy for robust results. In the article, *Molecular fingerprinting of nanoparticles in complex media with non-contact photoacoustics: beyond the light scattering limit*,[18] Pelivanov and coworkers developed a new method for non-contact PA spectroscopy which accurately measures absorption of light between 700-900 nm. Here, we show this method accurately measures the absorption of highly concentrated gold nanoparticles by contrasting the absorption signature of gold nanorods of different lengths and comparing the spectral measurements to the absorption cross sections predicted by FDTD simulations.

2.4.2 Results and Discussion

The absorption and scattering cross sections of plasmonic particles are both size-dependent, however the scattering cross section scales as r^6, where r is the effective particle radius, while the absorption cross section scales only as r^3.[19] As a result, the ratio of scattering:absorption for nanoparticles is notably different for particles of different sizes. For smaller particles, the scattering contribution is very weak, and the extinction cross section is largely attributed to the absorption cross section. For large particles, however, the scattering cross section is significantly larger, and plays a more significant role in the overall extinction cross section.

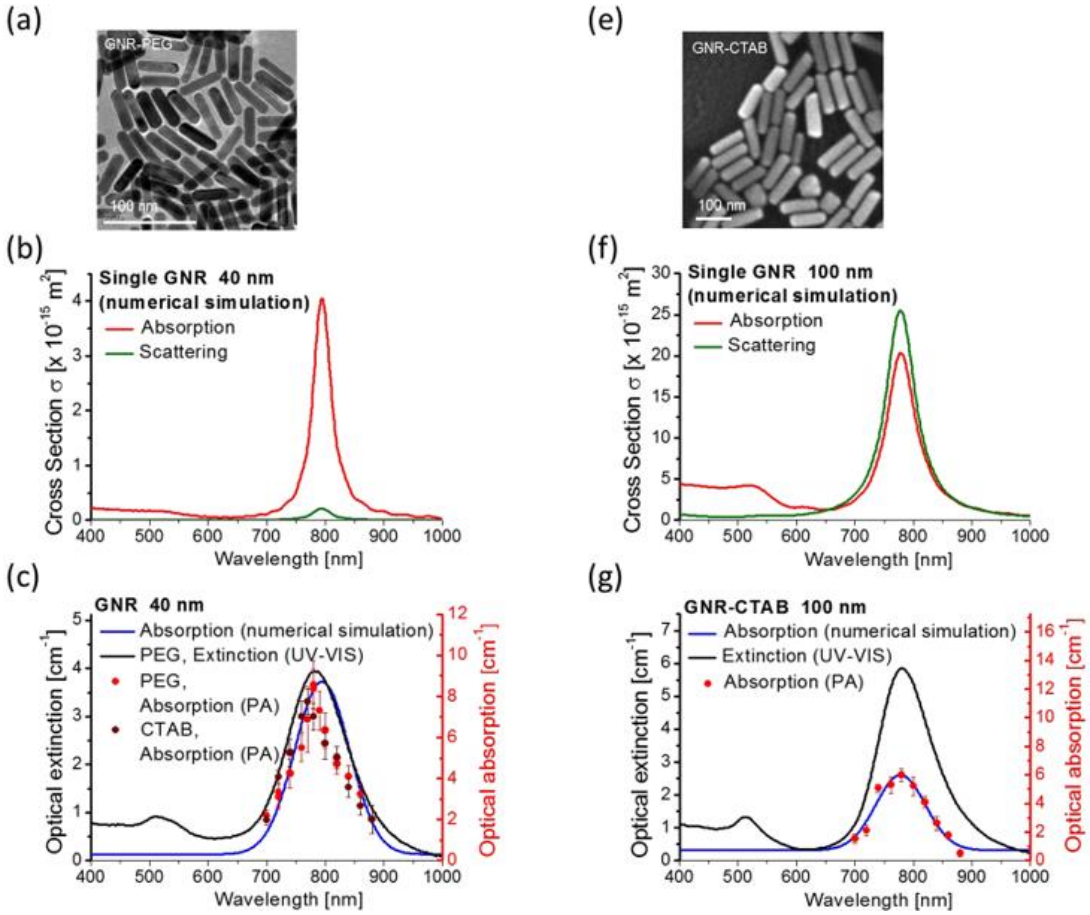

Figure 2.4.2.1 a,e) Electron micrographs of a) PEG-capped 40 nm gold nanorods and e) CTAB-capped 100 nm gold nanorods. b, f) Numerical FDTD simulation of absorption (red trace) and scattering (green trace) cross sections of the b) 40 nm and f) 100 nm gold nanorods. c, g) Gaussian-broadened simulated absorption of the c) 40 nm and g) 100 nm gold nanorod longitudinal peak (blue trace), experimental extinction curve of each sample (black trace), and experimental photoacoustic absorption of each sample (red points).

First, two samples of gold nanorods were obtained as shown in **Figure 2.4.2.1 a** and **e**, of dimensions ~40 x 11 nm and ~100 x 35 nm respectively. The size distribution for the 40 nm gold nanorod sample was provided by the commercial source (Nanohybrids), while the 100 nm sample was custom prepared following previously reported methods[20] and characterized by UV-Vis spectroscopy and scanning electron microscopy (SEM) (Appendix A).

We then computed the scattering and absorption cross sections of these samples by FDTD simulation using a single nanoparticle of the average dimension of each sample. Special attention was given to the slight variation of nanorod geometry, with the 40 nm nanorods displaying a more rounded edge than the 100 nm nanorods (see Methods and Appendix A for more information). The simulated scattering and absorption spectra of a single gold nanorod are shown in **Figure 2.4.2.1 b** and **f**. As predicted, for the 40 nm gold nanorod, the absorption cross section at the longitudinal localized surface plasmon resonance (l-LSPR) is significantly greater than the scattering cross section. In contrast, the absorption and scattering cross sections for the 100 nm gold nanorod are nearly the same at the l-LSPR, with the scattering cross section being even slightly greater than the absorption cross section, and both greater in magnitude than the 40 nm gold nanorod.

Finally, as shown in **Figure 2.4.2.1 c** and **g**, we homogenously broadened the simulated absorption cross section for each nanorod to fit the gaussian distribution of the ensemble extinction spectra in order to compare with the ensemble PA absorption spectra. We then overlay simulated cross sections with the experimentally obtained extinction spectra and PA absorption spectra. For both samples, the calculated optical absorption matched near perfectly to the measured PA absorption, indicating the photoacoustic spectrometer indeed measured only the light absorbed by the nanoparticles, despite the strongly scattering environment of a highly concentrated nanoparticle solution.

2.4.3 CONCLUSIONS

In conclusion, we have simulated the optical cross section of two gold nanorods with varying dimensions and geometries to support the experimental findings of a new non-contact photoacoustic spectroscopy technique. By accurately modeling the geometry and environment of

the nanoparticle as it would exist in solution, the numerical finite-difference time-domain simulated cross sections can also be considered realistically accurate. By showing consistent results between simulated optical absorption and measured optical absorption, we conclude the non-contact photoacoustic spectroscopy method described in this article measures only the light absorbed by the nanoparticle.

2.4.4 METHODS

Materials and Gold Nanorod Synthesis

Gold nanorods of about 40 nm in length and 11 nm in diameter were purchased from Nanohybrids (Austin, TX), with an l-LSPR peak at 773 nm. CTAB-coated GNRs of ~100 nm length were custom made in accordance with the protocol described by Ye et al.[20] Their parameters were: length 101 ± 9 nm, diameter 35 ± 5 nm, (aspect ratio 2.9), and LSPR peak at 774 nm.

Numerical Simulations

FDTD simulations were performed (Lumerical Solutions, Inc. - version 8.19.1466) using a partially rounded cylinder model for nanorods 42.9 nm long by 11.1 nm wide (~40 nm GNR) and 99.7 nm long by 35 nm wide (~100 nm GNR). The spheres used to model the ends of the rod had a radius of 5.55 nm and 30 nm (for 40 nm and 100 nm correspondingly) and were positioned so that the cross-sectional area matched the circular cross section of the cylinder. The rod was then shaped using a dielectric material ring matching the background index. The permittivity of gold was modeled by the Johnson and Christy gold dielectric function.[21] A simulation box with perfectly matched layer (PML) boundaries was used with a mesh size of 0.5 nm and 2 nm (for 40 nm and 100 nm correspondingly), with an override mesh refinement of 1 nm directly over the nanoparticle to ensure convergence. A background refractive index of 1.33 was chosen to simulate

an aqueous environment. A broadband total-field scatter-field with a range of 400–1,000 nm with linear 1 nm spacing was used as the illumination source.

To compare computed GNR optical spectra with experimentally measured ones (**Fig 2.4.2.1)** simulated data were homogenously broadened to the linewidth of the experimental data while conserving area, consistent with an ensemble distribution of particle sizes.

2.4.5 ACKNOWLEDGEMENTS

We would like to greatly thank Professor David Ginger in the Department of Chemistry at the University of Washington for several helpful discussions about this manuscript and the PA technology. This work was partially supported by NIH grants EB-016034, HL-125339, and EY-026532. We also acknowledge support provided by the Alvin L. and Verla R. Kwiram endowed fund and the Department of Bioengineering at the University of Washington.

2.4.6 ABBREVIATIONS

CTAB, cetyl trimethyl ammonium bromide; FDTD, finite-difference time-domain; GNR, gold nanorod; l-LSPR, longitudinal localized surface plasmon resonance; PA, photoacoustic; PML, perfectly matched layer; SEM, scanning electron microscopy

2.4.7 REFERENCES

1. Kreibig, U.; Vollmer, M. *Optical Properties of Metal Clusters*. (Springer Berlin Heidelberg, 1995). vol. 25.
2. Park, K.; Biswas, S.; Kanel, S.; Nepal, D.; Vaia, R. A. Engineering the Optical Properties of Gold Nanorods: Independent Tuning of Surface Plasmon Energy, Extinction Coefficient, and Scattering Cross Section. *J. Phys. Chem. C* **2014**, *118*, 32.
3. Chen, Y.-S.; Zhao, Y.; Joon Yoon, S.; Sam Gambhir, S.; Emelianov, S. Miniature gold nanorods for photoacoustic molecular imaging in the second near-infrared optical window. *Nat. Nanotechnol.* **2019**, *14*, 465–472.
4. Ratto, F.; Matteini, P.; Centi, S.; Rossi, F.; Pini, R. Gold nanorods as new nanochromophores for photothermal therapies. *J. Biophotonics* **2011**, *4*, 64–73.
5. Murphy, C. J.; Gole, A. M.; Stone, J. W.; Sisco, P. N.; Alkilany, A. M.; Goldsmith, E. C.; Baxter, S. C. Gold Nanoparticles in Biology: Beyond Toxicity to Cellular Imaging. **2008**, *1*,.
6. Jain, P. K.; Huang, X.; El-Sayed, I. H.; El-Sayed, M. A. Noble metals on the nanoscale: Optical and photothermal properties and some applications in imaging, sensing, biology, and medicine. *Acc. Chem. Res.* **2008**, *41*, 1578–1586.
7. Giljohann, D. A.; Mirkin, C. A. Drivers of biodiagnostic development. *Nature* **2009**, vol. 462 461–464.
8. Murphy, C. J.; Gole, A. M.; Hunyadi, S. E.; Stone, J. W.; Sisco, P. N.; Alkilany, A.; Kinard, B. E.; Hankins, P. Chemical sensing and imaging with metallic nanorods. *Chemical Communications* **2002**, vol. 8 544–557.
9. S Mura, J. C. P. C. Stimuli-responsible nanocarriers for drug delivery. *Nat. Mater.* **2012**, *12*, 991–1003.
10. Baffou, G.; Quidant, R. Thermo-plasmonics: Using metallic nanostructures as nano-sources of heat. *Laser and Photonics Reviews* **2013**, vol. 7 171–187.
11. Jokerst, J. V.; Thangaraj, M.; Kempen, P. J.; Sinclair, R.; Gambhir, S. S. Photoacoustic imaging of mesenchymal stem cells in living mice via silica-coated gold nanorods. *ACS Nano* **2012**, *6*, 5920–5930.
12. Lu, B.; Morgan, S. P.; Crowe, J. A.; Stockford, I. M. Comparison of methods for reducing the effects of scattering in spectrophotometry. *Appl. Spectrosc.* **2006**, *60*, 1157–1166.
13. Stramski, D.; Piskozub, J. Estimation of scattering error in spectrophotometric measurements of light absorption by aquatic particles from three-dimensional radiative transfer simulations. *Appl. Opt.* **2003**, *42*, 3634.
14. Stockford, I. M.; Lu, B.; Crowe, J. A.; Morgan, S. P.; Morris, D. E. Reduction of error in spectrophotometry of scattering media using polarization techniques. *Appl. Spectrosc.* **2007**, *61*, 1379–1389.
15. Karabutov, A. A.; Pelivanov, I. M.; Podymova, N. B.; Skipetrov, S. E. Determination of the optical characteristics of turbid media by the laser optoacoustic method. *Quantum Electron.* **1999**, *29*, 1054–1059.
16. Yorulmaz, M.; Nizzero, S.; Hoggard, A.; Wang, L. Y.; Cai, Y. Y.; Su, M. N.; Chang, W. S.; Link, S. Single-particle absorption spectroscopy by photothermal contrast. *Nano Lett.* **2015**, *15*, 3041–3047.
17. A Joplin, W.-S. C. S. L. Imaging and spectroscopy of single metal nanostructure absorption.

Langnuir Artic. ASAP **2017**, doi:10.1021/acs.langmuir.7b03154.
18. Jauffred, L.; Samadi, A.; Klingberg, H.; Bendix, P. M.; Oddershede, L. B. Plasmonic Heating of Nanostructures. *Chemical Reviews* **2019**, vol. 119 8087–8130.
19. Kelly, K. L.; Coronado, E.; Zhao, L. L.; Schatz, G. C. The optical properties of metal nanoparticles: The influence of size, shape, and dielectric environment. *J. Phys. Chem. B* **2003**, *107*, 668–677.
20. Ye, X.; Jin, L.; Caglayan, H.; Chen, J.; Xing, G.; Zheng, C.; Doan-Nguyen, V.; Kang, Y.; Engheta, N.; Kagan, C. R.; Murray, C. B. Improved size-tunable synthesis of monodisperse gold nanorods through the use of aromatic additives. *ACS Nano* **2012**, *6*, 2804–2817.
21. Johnson, P. B.; Christy, R. W. Optical constants of the noble metals. *Phys. Rev. B* **1972**, *6*, 4370–4379.

2.5 Theoretical Modeling of Exciton-Photon Fano Resonances and Rabi Splitting of Single Silver Nanoprisms Coupled to 2D Perovskite Films

This section is adapted with modification with permission from the original publication "Tuning Hybrid Exciton-Photon Fano Resonances in Two-Dimensional Organic-Inorganic Perovskite Thin Films" Franziska Muckel, Kathryn N. Guye, Shaun M. Gallagher, Yun Liu, David S. Ginger, which has been submitted to ACS Nano Letters.

2.5.1 Introduction

Plasmonic nanoparticles have the unique capability of focusing light beneath the diffraction limit, generating strong local electric field enhancement when illuminated at the localized surface plasmon resonance (LSPR) energy. When placed within a few nanometers of other materials like chromophores or excitonic emitters the proximity to the nanoparticle and the overlap of absorbance and emission spectra with the LSPR spectrum can quench the fluorescence of the material, enhance absorption of light, or enhance the rate of emission from the excited state.[1–4]

Strong coupling occurs between a plasmonic cavity and an emitter if a resonant exchange of energy occurs between the molecular transition and the focused electric field, resulting in a reversible exchange of energy between light and matter.[5,6] Characterizing and controlling such light-matter interaction is necessary for the generation of new optoelectronic devices and technologies such as polariton lasing or quantum computing,[7,8] relying on effects like enhanced absorption,[9] increased spontaneous emission,[10,11] and Rabi splitting.[12–14]

Due to the intense scattering resonance of plasmonic nanoparticles due to the attenuation of the electric field, Fano resonances are commonly observed between composite materials due to

the interference of scattering resonances, and observed as an asymmetric scattering spectrum.[15–17] Materials with high refractive indices, such as lead halide perovskites (LHPs), can even generate optical resonances with itself as a hybrid exciton-photon Fano resonance.[18,19] This effect, however, can often generate a complex scattering spectrum with multiple interactions and individual components contributing to the overall spectrum of a plasmonic-coupled emitter.

Here, we study Fano resonances generated by a geometry-dependent exciton-photon interference of 2D butylammonium lead iodide (BAPI) perovskite grains, and further explore plasmonic coupling to this hybrid state. Finite-difference time-domain (FDTD) simulations are employed in order to isolate specific interactions between different components of the system and characterize both the self-contained Fano resonance and the coupling strength to silver nanoprisms. Using the simulated scattering spectra to isolate the contribution of only the plasmonic silver nanoprism, we identify Rabi splitting in the strong coupling regime.

2.5.2 Results and Discussion

In this work, Muckel et al. demonstrated an asymmetric peak splitting in the scattering spectra of both an excitonic, two-dimensional (2D) lead halide perovskite (LHP) thin film, butylammonium lead iodide (BAPI) and silver nanoprism (AgNP)-coupled to the LHP film. Intrigued by the asymmetric scattering spectra of the BAPI film even without the presence of a plasmonic cavity, we simulated the scattering and absorbance spectra of a continuous BAPI film, disk-like BAPI grains, and a disk-like dielectric grain, revealing a geometrically-defined scattering resonance resulting in an exciton-photon Fano resonance and Rabi splitting of the AgNP localized surface plasmon resonance (LSPR).

As shown in **Figure 2.5.2.1**, we modeled the dielectric properties of BAPI by ellipsometry spectroscopy and from these measurements, obtained the wavelength-dependent refractive index,

n, and extinction coefficient, k, values. The n and k values were then imported into the finite-different time-domain (FDTD) simulation software, Lumerical, as a 2D-sampled material to model the scattering of a BAPI grain with 150 nm diameter and a thickness of 20 nm. As seen in Fig. 2.5.2.1c., the BAPI grain scattering (green trace) demonstrates an asymmetric split peak at the excitonic transition, whereas a grain of identical dimensions comprised of a high-refractive index dielectric material only shows a monotonic decrease of scattering as wavelength increases, with no resonance at the excitonic transition. We interpret this difference as evidence that the asymmetric peak is not due to the geometric scattering of the BAPI grain alone, but rather as a hybrid exciton-photon Fano resonance between the geometric resonance and the excitonic transition. Furthermore, to account for a distribution of BAPI grain size in a given sample, we simulated grains with a 20 nm thickness and 300, 500, and 700 nm diameters. For each increase in diameter, the total scattering intensity increased, but the lineshape of the spectra otherwise did not change, revealing any observed variation in lineshape of BAPI-AgNP composite samples is due to factors other than local heterogeneity in the BAPI film.

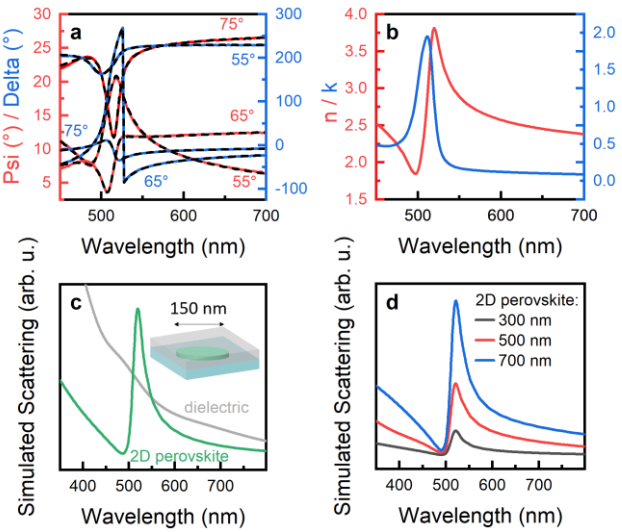

Figure 2.5.2.1. a) Spectroscopic ellipsometry data and globally fitted model (dashed lines) for different incident angles of the light (55°, 65° and 75°), measured on a BAPI thin film on glass at

room temperature. b) Refractive index, n, and extinction coefficient, k, of the 2D perovskite, as extracted from the ellipsometry measurements. c) Simulated scattering spectrum (green line) assuming a cylindrical 2D perovskite grain. The grey line represents the scattering of a dielectric disk with the same dimensions and a constant refractive index of 2.15, providing a reference for BAPI without the excitonic resonance. The inset depicts a schematic of the FDTD model used for the simulations. The perovskite grains are modeled as a cylinder with a thickness of 20 nm and a diameter of 150 nm embedded in a matrix of PMMA (refractive index of 1.4) on a glass substrate. d) Simulated scattering spectra for 2D perovskite grains with a thickness of 20 nm and different diameters of 300, 500 nm and 700 nm, all embedded in PMMA.

Next, as the experimental scattering of the low-energy branch of the coupled AgNP spectra were often obscured by the intense scattering of the exciton-photon Fano resonance (except in the case of very strongly-coupled nanoparticles with a significant redshift of the low-energy peak), we simulated the scattering spectra of AgNP of varying sizes and AgNP coupled to a BAPI thin film as shown in **Figure 2.5.2.2.** For the first simulations, we chose to model the BAPI film as a continuous layer to isolate the exciton-plasmon coupling without the exciton-photon Fano resonance scattering. The AgNP were modeled using silver optical coefficients by Palik[20] with the nanoparticle shape as disks, with a 14 nm thickness and 20 – 40 nm diameter, rather than triangular prisms due to shape distribution in the nanoparticle sample after ligand exchange. As such, we knowingly slightly underestimate the coupling strength due to a reduced electric field enhancement, and avoid making false claims about the magnitude of the BAPI-AgNP coupling strength.

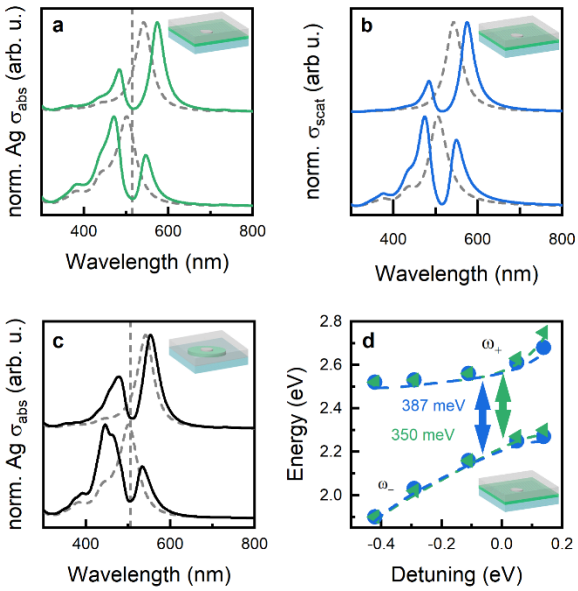

Figure 2.5.2.2. a,b) Simulated a) absorption and b) scattering by the Ag nanodisks within the AgNP - 2D perovskite system: Ag nanodisks with different sizes (30 nm and 40 nm from bottom to top) placed on a uniform layer of 2D perovskite embedded in PMMA. Grey dashed traces in a) and b) depict the scattering and absorption spectra, respectively, of the uncoupled Ag nanodisks embedded in a dielectric material with refractive index of 1.4 on glass. c) Isolated AgNP absorption of Ag nanodisks with a 20 nm (bottom) and 30 nm (top) diameter on top of a 150 nm diameter BAPI grain placed on glass and embedded in PMMA. d) Detuning plot extracted from the maxima in the scattering and absorption spectra of Ag nanodisks with different sizes (as in a and b, among others), placed on a uniform layer of 2D perovskite embedded in PMMA (see (a-b)). The detuning value is determined as the difference between the medium peak position of the scattering of uncoupled AgNP and the energetic position of the dip in the scattering of coupled particles (2.401 eV). Dashed lines are guides to the eye.

First, we simulated a AgNP embedded in a dielectric material with a refractive index of 1.4 on glass to show the LSPR of the uncoupled nanoparticle in the same sample orientation embedded in a PMMA layer, only without a BAPI film underneath. The LSPR of the AgNP in both scattering and absorption were singular peaks and only very slightly redshifted from their solution-sampled resonance position due to the slight increase in refractive index from water to PMMA. We then modeled the silver nanoprism on top of an infinitely wide, 20 nm thick BAPI film. The continuous BAPI film did not significantly scatter light (Appendix A), as such, the scattering spectra obtained from the simulation could be presumed to be purely from the AgNP. To obtain the absorbance of

only the AgNP and not the BAPI film, a frequency-domain field and power monitor was placed around the nanoparticle, not overlapping with the BAPI film. For all nanoparticle sizes, we observed a split peak in both the scattering and absorption of the AgNP, with a dip centered between 513-515 nm. This peak splitting of the plasmon resonance in both scattering and absorption is indicative of plasmon-exciton strong coupling. We then placed the AgNP on top of a simulated BAPI grain, which resulted in the dip blue-shifting to about 506 nm, similar to what was observed in experimental data. This is evidence the plasmon resonance couples directly to the hybrid exciton-photon resonance. Finally, we calculate the detuning values for a variety of nanoparticle diameters, and calculate a Rabi splitting of 387 meV from the absorption resonances and 350 meV from the scattering resonances. These values suggests the BAPI and AgNP are strongly coupled.

2.5.3 CONCLUSIONS

In conclusion, we have used finite-difference time-domain simulations to identify geometric scattering of a dielectric grain and a hybrid exciton-photon Fano resonance between the geometric scattering and the excitonic transition of the 2D perovskite. We have shown coupling between both the silver nanoparticle plasmon resonance by peak splitting of the scattering and absorbance resonances of the nanoparticle, and coupling for the plasmon resonance to the hybrid exciton-photon Fano resonance generated by the BAPI grain microstructure. Lastly, by calculating the detuning energy of the system with nanoparticles of varying sizes, we provide simulated evidence that silver nanoparticle strongly couple to the 2D perovskite BAPI film. The use of finite-difference time-domain simulations shown here provide data complimentary to experimental data, where spectra cannot be deconvolved to reveal the intricacies of multiple coupled materials.

2.5.4 METHODS

Synthesis of AgNP. Silver nanoprisms were synthesized by slightly modifying the process as previously described. [21,22] All glassware and stir bars were cleaned beforehand with aqua regia (3:1 v:v HCl:HNO_3) and rinsed thoroughly with Milli-Q purified water (18.2 MΩ/cm). All reagents were purchased from Millipore Sigma. In a 250 mL round bottom flask, 95 mL of water, 2 mL of 5 mM $AgNO_3$, and 1 mL of 30 mM sodium citrate were combined. The flask was wrapped in foil and placed in ice. The solution was purged with N_2 and stirred with a magnetic stirrer for 1 hour. At this time, 1 mL of 50 mM $NaBH_4$, freshly prepared in cold water, was injected into the reaction solution under rigorous stirring, yielding a transparent, pale yellow solution indicating the formation of silver seeds. The solution was then allowed to equilibrate for 5 minutes. 400 µL of the 50 mM $NaBH_4$ solution was then slowly added to the solution over six minutes. In a separate vial, 1 mL of 5 mM bis(p-sulfonatophenyl)phenylphosphine dihydrate dipotassium salt (BSPP) was combined with 500 µL of the 50 mM $NaBH_4$ solution. 15 minutes after the first borohydride injection, the BSPP/$NaBH_4$ solution was slowly added to the reaction solution over 5 minutes. The seed solution was then allowed to age in the dark for 15 hours in an ice bath without stirring. At this time, if the extinction peak of the precursor solution was 393-394 nm, the pH of the solution was adjusted to 11.0, monitored with a LabQuest 2 pH electrode. The spherical silver particles were then photochemically converted to flattened nanoprisms by placing the solution under a 470 nm or 505 nm LED for smaller and larger prisms, respectively. Samples were exposed to the LED until no significant change to the plasmon resonance was observed. During this time, the solution changed from bright yellow to orange or purple, respectively. Nanoparticles were characterized optically on an Agilent 8453 UV-Vis spectrometer and by electron microscopy on an FEI Sirion scanning electron microscope with an accelerating voltage of 5 kV.

FDTD simulations. To investigate the BAPI exciton-photon Fano resonance and estimate the coupling strength between the AgNP and the BAPI 2D films, we conduct 3-dimensional finite-difference time-domain (FDTD) calculations using a commercial software (Lumerical Solutions, Inc. FDTD solver, version 8.18). The coupled structure is modeled as a silver nanodisk (14 nm thickness with diameters between 20 and 40 nm) on top of the BAPI film, which is placed on top of an infinite glass substrate. The AgNP is covered with an infinite PMMA layer (constant n=1.4). The simulations of bare BAPI in Figure 2 were obtained omitting the AgNP. The BAPI was either modeled as an infinite film of 20 nm thickness (compare schematic in Figure 4), or as a disk with 20 nm thickness and various diameters (see schematic in Figure 4d), with a gap of 1 nm between the BAPI and the AgNP to represent the capping ligand layer. The dielectric function of the silver was modeled using the Palik (0 – 2 μm) Ag model[20], and the glass substrates was described as the Palik SiO_2 model. The BAPI dielectric function extracted via ellipsometry measurements was implemented in the simulation with a single Lorentzian (see Figure S4). The system was illuminated with a broadband total-field scattered-field light source. Scattering and absorption cross sections are calculated by placing frequency-domain field and power monitors outside and inside the source, respectively. The absorption of the AgNP within the coupled system is isolated with a monitor surrounding only the particle.

2.5.5 ACKNOWLEDGEMENTS

This material is based upon work supported primarily by the US Department of Energy, Office of Science, Office of Basic Energy Sciences, as part of the Energy Frontier Research Centers program: CSSAS--The Center for the Science of Synthesis Across Scales under Award Number DE-SC0019288. F.M. acknowledges postdoctoral fellowship support from the German Academic

Exchange Service (DAAD) with funds from the German Federal Ministry of Education and Research (BMBF) and the European Union (FP7-PEOPLE-2013-COFUND - grant agreement n° 605728). Y. L. acknowledges support from the Office of Naval Research through Grant Number N00014-17-1-2201 for performing the ellipsometry measurements. Part of this work was conducted at the Molecular Analysis Facility, a National Nanotechnology Coordinated Infrastructure (NNCI) site at the University of Washington, which is supported in part by funds from the National Science Foundation (awards NNCI-2025489, NNCI-1542101), the Molecular Engineering & Sciences Institute, and the Clean Energy Institute. We are thankful to Harrison J. Goldwyn, Kevin C. Smith, and David J. Masiello for insightful discussions.

2.5.6 ABBREVIATIONS

2D, Two-dimensional; AFM, atomic force microscopy; AgNP, silver nanoparticles; BAPI, butylammounium lead iodide $(C_4H_9NH_3)_2PbI_4$; FDTD, finite-difference time-domain; FWHM, full-width at half-maximum; LHPs, lead halide perovskites; PL, photoluminescence; PMMA, poly(methyl methacrylate)

2.5.7 REFERENCES

1. Munechika, K.; Chen, Y.; Tillack, A. F.; Kulkarni, A. P.; Plante, I. J. La; Munro, A. M.; Ginger, D. S. Spectral control of plasmonic emission enhancement from quantum dots near single silver nanoprisms. *Nano Lett.* **2010**, *10*, 2598–2603.
2. Chen, Y.; Munechika, K.; Ginger, D. S. Dependence of fluorescence intensity on the spectral overlap between fluorophores and plasmon resonant single silver nanoparticles. *Nano Lett.* **2007**, *7*, 690–696.
3. Chen, Y.; Munechika, K.; Jen-La Plante, I.; Munro, A. M.; Skrabalak, S. E.; Xia, Y.; Ginger, D. S. Excitation enhancement of CdSe quantum dots by single metal nanoparticles. *Appl. Phys. Lett.* **2008**, *93*, 053106.
4. HA Atwater, A. P. Plasmonics for improved photovoltaic devices. *Nat. Mater.* **2010**, *9*, 205–213.
5. Dovzhenko, D. S.; Ryabchuk, S. V.; Rakovich, Y. P.; Nabiev, I. R. Light-matter interaction in the strong coupling regime: Configurations, conditions, and applications. *Nanoscale* **2018**, vol. 10 3589–3605.
6. Törmö, P.; Barnes, W. L. Strong coupling between surface plasmon polaritons and emitters: A review. *Reports on Progress in Physics* **2015**, vol. 78 013901.
7. Makarov, S.; Furasova, A.; Tiguntseva, E.; Hemmetter, A.; Berestennikov, A.; Pushkarev, A.; Zakhidov, A.; Kivshar, Y. Halide-Perovskite Resonant Nanophotonics. *Adv. Opt. Mater.* **2019**, *7*, 1800784.
8. Su, R.; Ghosh, S.; Wang, J.; Liu, S.; Diederichs, C.; Liew, T. C. H.; Xiong, Q. Observation of exciton polariton condensation in a perovskite lattice at room temperature. *Nat. Phys.* **2020**, *16*, 301–306.
9. Carretero-Palacios, S.; Calvo, M. E.; Míguez, H. Absorption Enhancement in Organic-Inorganic Halide Perovskite Films with Embedded Plasmonic Gold Nanoparticles. *J. Phys. Chem. C* **2015**, *119*, 18635–18640.
10. Yang, Z.; Pelton, M.; Bodnarchuk, M. I.; Kovalenko, M. V.; Waks, E. Spontaneous emission enhancement of colloidal perovskite nanocrystals by a photonic crystal cavity. *Appl. Phys. Lett.* **2017**, *111*,.
11. Adamo, G.; Swaha Krishnamoorthy, H. N.; Cortecchia, D.; Chaudhary, B.; Nalla, V.; Zheludev, N. I.; Soci, C. Metamaterial Enhancement of Metal-Halide Perovskite Luminescence. *Nano Lett.* **2020**, doi:10.1021/acs.nanolett.0c02571.
12. Zhang, X.; Shi, H.; Dai, H.; Zhang, X.; Sun, X. W.; Zhang, Z. Exciton-Polariton Properties in Planar Microcavity of Millimeter-Sized Two-Dimensional Perovskite Sheet. *ACS Appl. Mater. Interfaces* **2020**, *12*, 5081–5089.
13. Du, W.; Zhang, S.; Zhang, Q.; Liu, X. Recent Progress of Strong Exciton–Photon Coupling in Lead Halide Perovskites. *Adv. Mater.* **2019**, *31*, 1–6.
14. Fieramosca, A.; Polimeno, L.; Ardizzone, V.; De Marco, L.; Pugliese, M.; Maiorano, V.; De Giorgi, M.; Dominici, L.; Gigli, G.; Gerace, D.; Ballarini, D.; Sanvitto, D. Two-dimensional hybrid perovskites sustaining strong polariton interactions at room temperature. *Sci. Adv.* **2019**, *5*, 1–7.
15. Fano, U. Effects of Configuration Interaction on Intensities and Phase Shifts. *Phys. Rev.* **1961**, *124*, 1866–1878.
16. Limonov, M. F.; Rybin, M. V.; Poddubny, A. N.; Kivshar, Y. S. Fano resonances in

photonics. *Nat. Photonics* **2017**, *11*, 543–554.
17. Majorana, E. Teoria dei tripletti P′ Incompleti. *Nuovo Cim.* **1931**, *8*, 107–113.
18. Zhang, S.; Shang, Q.; Du, W.; Shi, J.; Wu, Z.; Mi, Y.; Chen, J.; Liu, F.; Li, Y.; Liu, M.; Zhang, Q.; Liu, X. Strong Exciton-Photon Coupling in Hybrid Inorganic-Organic Perovskite Micro/Nanowires. *Adv. Opt. Mater.* **2018**, *6*, 1701032.
19. Shang, Q.; Zhang, S.; Liu, Z.; Chen, J.; Yang, P.; Li, C.; Li, W.; Zhang, Y.; Xiong, Q.; Liu, X.; Zhang, Q. Surface Plasmon Enhanced Strong Exciton–Photon Coupling in Hybrid Inorganic–Organic Perovskite Nanowires. *Nano Lett.* **2018**, *18*, 3335–3343.
20. Palik, E. *Handbook of Optical Constants of Solids*. (Academic Press, 1985).
21. Xue, C.; Mirkin, C. A. pH-switchable silver nanoprism growth pathways. *Angew. Chemie - Int. Ed.* **2007**, *46*, 2036–2038.
22. Jin, R.; Cao, Y. C.; Hao, E.; Métraux, G. S.; Schatz, G. C.; Mirkin, C. A. Controlling anisotropic nanoparticle growth through plasmon excitation. *Nature* **2003**, *425*, 487–490.

CHAPTER 3. INVESTIGATION OF THE PHOTORESPONSIVE AND PHOTOKINETIC PROPERTIES OF A TETRAMETHOXYAZOBENZENE- AND B-CYCLODEXTRIN-FUNCTIONALIZED POLYMER WITH SELF-FOLDING BEHAVIOR

This section is adapted with modification with permission from the original publication "Dual-stimuli responsive single-chain polymer folding via intra-chain complexation of tetramethoxyazobenzene and β-cyclodextrin" Daniel, Lee, Kathryn N. Guye, Rajan Paranji, Kacper Lachowski, Lilo Pozzo, David S. Ginger, and Suzie H. Pun, which has been submitted to Langmuir.

3.1 OVERVIEW

We synthesize and characterize a tri-block polymer with asymmetric tetramethoxyazobenzene (TMAB) and β-cyclodextrin functionalization, taking advantage of the well-characterized azobenzene derivative-cyclodextrin inclusion complex to pro-mote photo-responsive, self-contained folding of the polymer in an aqueous system. Important for its potential use as a functional material, we show the photoisomerization cyclability of the polymeric TMAB chromophore and calculate isomerization quantum yields by extinction spectroscopy. The observed decrease in photoisomerization quantum yield for the dual-functionalized polymer compared to the isolated chromophore in an aqueous solution confirms TMAB and β -cyclodextrin not only are in proximity to one another, but also form the inclusion complex.

3.2 INTRODUCTION

Molecular switches, motifs that undergo chemical changes in response to external stimuli, have been incorporated into nanoparticle and polymer systems to achieve functional materials. By controlling molecular motion on the nanoscale, researchers have been able to design materials for applications such as nanoactuation,[1–3] drug delivery,[4–6] catalysis,[7,8] and sensing.[7,9]

We were particularly interested in developing a synthetic polymer system that exhibits photoresponsive folding behavior. Light is an attractive stimulus as it can be (1) applied noninvasively from a distance, (2) temporally and spatially controlled, and (3) different wavelengths can be used to selectively activate different chromophores.

Folding behavior has been explored in both biopolymer and synthetic systems, and can be observed by changes in fluorescence between Förster resonance energy transfer pairs,[10] resonant frequencies between plasmonic dimers,[11,12] and electron spin resonance spectra between nitroxide spin labels.[13] More macroscopic changes in the biopolymer have been measured without labeling via circular dichroism[14] and nuclear Overhauser effect (NOE) nuclear magnetic resonance (NMR) experiments.[15]

In synthetic polymer systems, folding behavior can be achieved by placing bonding or complexing molecular pairs at different positions along the polymer main chain. For example, folding polymers of different architectures have been achieved by placing alkynes in different positions along the polymer main chain and covalently stapling them with azide-alkyne click chemistry.[16] In contrast, reversibly folding polymers can be realized by placing stimuli-responsive molecular pairs on the α- and ω- ends of a polymer. One of the earliest reports of reversible folding behavior involved the use of a short oligo(ethylene glycol) chain with anthracenes on the α- and ω- ends that can photodimerize to lock the folded chain.[17] Such α-/ω- complexation has been

further explored to make reversibly folding polymers using hydrogen donor-acceptor pairs,[18,19] metal-ligand complexes,[20] host-guest pairs including β-cyclodextrin (βCD).[21,22]

We set out to further develop these concepts further with a folding polymer that was of high molecular weight and could reversibly fold in response to multiple stimuli. Because large polymers in water often exhibit complicated solution phase behavior as a function of temperature, we wanted to avoid heat as one of the stimuli. Of the many molecular recognition pairs in the literature, the azobenzene-cyclodextrin pair offers attractive features of photoreversible complexation, relative ease of synthesis and derivatization, and subsequent tunable properties.[23–25] Azobenzenes have gained significant attention due to their ability to undergo reversible (E)-to-(Z) isomerization in response to temperature[26] and different wavelengths of light,[23] and have even been used to control polymer morphology[27–29] and solution self-assembly.[30–33] (E)-Azobenzenes complex with cyclodextrin in water to reduce the entropic penalty of water ordering around the hydrophobic (E)-azobenzenes and the hydrophobic inner core of cyclodextrin. (Z)-azobenzenes, however, often exhibit much lower equilibrium association constant (K_a) with cyclodextrins, due to the hydrophilic dipole perpendicular to the azo bond and the steric interference between non-planar (Z)-azobenzene and the fixed diameter of the cyclodextrin inner core. Azobenzene-

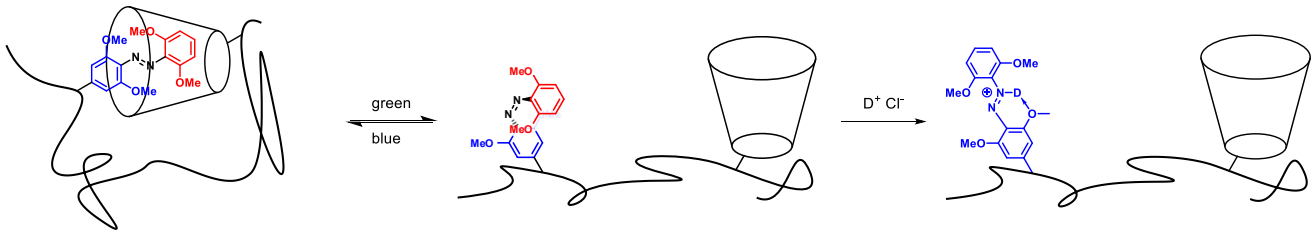

Scheme 3.2.1. Poly1 reversible photoinduced folding and unfolding and irreversible Brønsted acid induced unfolding. Schematic courtesy of Daniel Lee.

cyclodextrin pairs have already been used in stimuli-responsive reversible hydrogels,[34–36] drug release,[25,37,38] material property modulation,[39,40] and supramolecular assembly.[36,41,42]

We identified tetramethoxyazobenzene (TMAB) and β-CD as our molecular recognition pair of choice. βCD shows preferential binding of (E)-TMAB (K_a = 1546 M^{-1}) over (Z)-TMAB (K_a = 82.1 M^{-1}).[25] Although the azobenzene/αCD pair exhibits ~150-fold selectivity for (E)-azobenzene (while TMAB/βCD exhibits ~20-fold selectivity), functionalization of αCD is notoriously difficult and unfunctionalized azobenzenes are not multi-stimuli responsive. The ratio of (E)/(Z)-TMAB can be modulated using multiple stimuli, including heat, light, and Brønsted acids.[43] In particular, the presence of Brønsted acids catalyzes the (Z)-to-(E) isomerization[44,45] and shifts the equilibrium to (E)-TMAB via formation of an intramolecular hydrogen bonding 6-membered species.[43]

Herein we the optical characterization of a multi-stimuli responsive high molecular weight folding polymer (**poly1**). **Poly1** is a triblock copolymer with multiple TMAB and βCD moieties and can be reversibly unfolded by photoinduced (Z)-to-(E) isomerization of TMAB. **Poly1** can also be irreversibly unfolded under acidic conditions; even though introduction of acids favors (E)-TMAB, the protonated (E)-TMAB is no longer hydrophobic and does not complex with βCD (Scheme 1). Folding behavior was characterized by illumination-dependent extinction spectroscopy.

3.3 Results and Discussion

TMAB displays a characteristic double-peak extinction spectrum representing the π-π* and n-π* transitions. Unlike unmodified azobenzene which requires UV light for (E)-to-(Z) isomerization, TMAB undergoes photoisomerization with visible light in both directions as shown in **Figure 3.2.1 a**. When exposed to 523 nm light, (E)-TMAB isomerizes to the less thermally stable (Z)-TMAB which can be observed as a decreasing intensity and blueshift of the π-π*

extinction peak at 320 nm, as well as a blueshift of the n-π* peak at 446 nm. Rapid photoisomerization from (Z)-to-(E) can be obtained by 470 nm illumination.[46] We observe this process by the red-shifting of both extinction peaks and an increased extinction intensity of the π-π* peak.

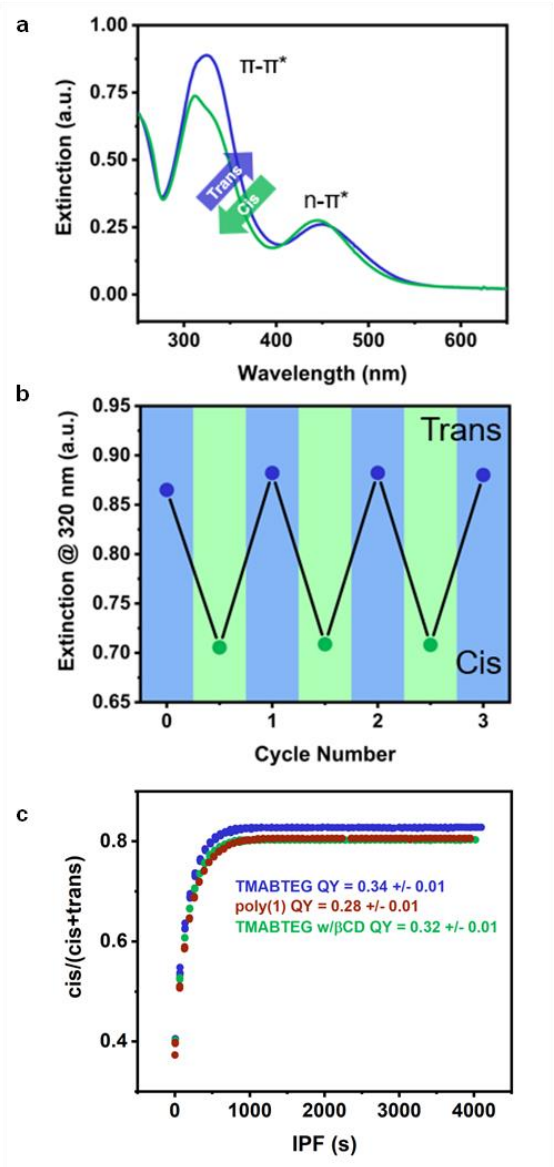

Figure 3.3.1. Quantification of TMAB photoisomerization on poly1. a) Absorption spectrum of poly1 after irradiation with green or blue light. b) Absorption of poly1 at 320 nm after multiple cycles of irradiation with green and blue light. c) Determination of photoisomerization quantum yield of poly1 (red), TMAB-TEG(blue), and TMAB-HP-βCD (green).

Alternating 523 nm and 470 nm LED illuminations revealed the photoisomerization of the TMAB chromophore in poly1 is reversible with no change in the extinction spectrum of the chromophore with repeat cycling as shown in **Figure 3.2.1 b.** Additionally, we determined the photoisomerization quantum yield on TMAB on poly1 and TMAB-TEG. For studies with TMAB-TEG, we used hydroxypropyl-βCD, a more soluble analog of βCD, to attempt to mimic the high local concentration of βCD on poly1.

When comparing the extinction spectra of poly1 to TMAB-TEG, a notable 24 nm redshift of the TMAB-TEG π-π* peak is observed, which can be attributed to the formation of small micellular aggregates[47,48] in solution (Appendix B). When TMAB-TEG is dissolved in excess (2-hydroxypropyl)- β-cyclodextrin (HP-βCD), the extinction spectrum is blueshifted towards the poly1 spectrum as these aggregates are disrupted by the newly formed inclusion complexes. We therefore conclude that TMAB-TEG readily includes βCD in aqueous solutions.

We next sought to confirm the occurrence of inclusion complexes between the TMAB and βCD moieties tethered to the poly1 backbone by determining the photoisomerization quantum yield of (E)-to-(Z) TMAB and comparing to the quantum yields of free TMAB-TEG and TMAB-TEG with soluble HP-βCD. Of the three solutions, folded poly1 would be expected to exhibit the lowest quantum yield for the photoinduced (E)-to-(Z) TMAB isomerization due to the high local concentration of βCD at the polymer backbone, and resulting steric hindering of the (E)-to-(Z) isomerization of an included TMAB molecule. Isomerization of (Z)-to-(E) azobenzene is generally believed to follow a sterically unhindered inversion mechanism[49–51]. (E)-to-(Z) isomerization on the other hand, undergoes a sterically hindered rotation or hula twist, in which case the fraction of azobenzene able to undergo a (E)-to-(Z) isomerization is dependent on the local environment of the chromophore[52–54]. A more sterically crowded environment, such as on the inside of a

cyclodextrin molecule, will limit the rotation of TMAB and thereby reduce the yield of (E)-to-(Z) isomerization, lowering the quantum yield of photoisomerization.

We then measured the extinction spectrum of poly1 and TMAB-TEG over time, shown in **Figure 3.3.1 c**, at low illumination fluence, 5 mW/cm^2, with a 523 nm LED (LED Engin). Time was converted to the integrated photokinetic factor (IPF) (Eqn 3.2.2) to account for the absorption of 523 nm light with time while the extinction spectrum changes, effectively converting time to photon dose. Using a modified method[52] to determine the fraction of (Z)-TMAB with time, these curves were then fit to an exponential curve as:

$$y_t = (y_0 - y_\infty)\, exp(-Ax) + y_\infty \qquad (3.3.1)$$

where y is the fraction of (Z)-TMAB at times t, t=0, and the final photostationary state, x is the IPF, and A is the prefactor value, which is directly related to the (E)-to-(Z) quantum yield, $\Phi_{(E)}$, at 523 nm.

Due to the lineshape differences of the TMAB extinction spectra between poly1, TMAB-TEG, and TMAB-TEG with HP-βCD, the fraction TMAB chromophores in the cis vs. trans state at each of the photostationary states, determined by ^{1}H NMR for TMAB-TEG, could not be extrapolated to the other two solutions at a singular wavelength.

By integrating between isobestic points on the π-π* and n-π*, region I and II respectively in **Figure 3.3.2 a.**, we anticipated that the decrease in region I was proportional to the decrease in [(E)-TMAB] and the increase in region II was proportion to the increase in [(Z)-TMAB$_{cis}$].

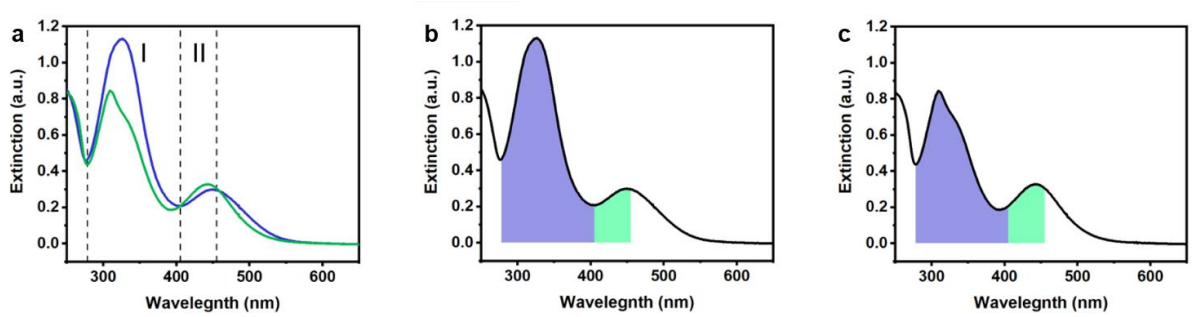

Figure 3.3.2. a) The extinction spectra of (E)-TMAB (purple trace) and (Z)-TMAB (green trace) in poly1 with dotted lines at the isobestic points to depict region I and region II. b,c) Integrated region I (purple) and region II (green) for b) (E)-TMAB and c) (Z)-TMAB.

For the known TMAB-TEG samples, the change in the area under each peak were equal to the measured concentration changes within a 1% deviation. We therefore determined this method could be expanded to the poly1 and TMAB-TEG with HP-βCD samples to determine the [$TMAB_{cis}$] at the photostationary state, assuming all samples began with and equivalent ratio of (Z):(E) isomers.

For each sample, intermediate plots were fit as a linear combination of their starting (mostly trans) and end (mostly cis) spectra. The variable defining the weight of the mostly cis state was then normalized between the initial fraction of $TMAB_{cis}$ as measured by ^{1}H NMR and the final fraction of $TMAB_{cis}$ as determined by the change in peak integration.

Photoisomerization quantum yields were calculated by the methods described by Samai et al.[52]

The photokinetic plots in **Figure 3.3.1 c.** were fit to Eqn 3.2.1, where y is the fraction of (Z)-TMAB at time t, t=0, and the photostationary state. A is the prefactor, and x is the integrated photokinetic factor (IPF).

The integrated photokinetic factor (IPF) was used in order to convert time to photon dose at 523 nm in order to take into account the lineshape changes at the incident wavelength. IPF was calculated by integrating the following equation for the photokinetic factor (F_t):

$$F_t = \frac{1-10^{-abs_t^{\lambda}}}{abs_t^{\lambda}} \qquad (3.3.2)$$

In the above, abs^{λ} is the extinction value at the illumination wavelength (523 nm) at time, t. Finally, the quantum yield, $\Phi_{(E)}$, can be determined by the following:

$$\Phi_{(E)} = \frac{A\,V\,y_{\infty}}{I^{\lambda}\,l\,\varepsilon_{trans}^{\lambda}} \qquad (3.3.3)$$

Where A is the prefactor, V is the solution volume, y_{∞} is the fraction of (Z)-TMAB at the photostationary state, I^{λ} is the illumination intensity, ε^{λ} is the extinction coefficient.

From these results, we calculate a photostationary state of 83% (Z)- TMAB-TEG and 81% (Z)-form for poly1. For TMAB-TEG, a $\Phi_{(E)}$ of 0.34 +/- 0.01 is observed while $\Phi_{(E)}$ = 0.28 +/- 0.01 for poly1. Indeed, a decrease for $\Phi_{(E)}$ is observed for poly1, indicating inclusion of TMAB. To confirm inclusion as the source of a decreased $\Phi_{(E)}$, we repeated this experiment with the TMAB-HP-βCD solution (Figure 2c). An intermediate $\Phi_{(E)}$ of 0.32 +/- 0.01 was observed. An intermediate value is consistent with the previous extinction spectrum indicating incomplete inclusion of all TMAB chromophores in the TMAB-HP-βCD solution. We rationalize this result by taking not only solution concentration into account, but rather local concentration. As poly1 tethers TMAB and βCD within close proximity to one another, the two moieties are more likely to form an inclusion complex than untethered, individual TMAB and βCD molecules in solution.

While some studies reveal a $\Delta\Phi_{(E)}$ as large as 50% due to local steric hindrance of azobenzene isomerization, recent work by Royes et al.[55] report $\Delta\Phi_{(E)}$ of a similar magnitude for the inclusion of unmodified azobenzene with cyclodextrins in a pure aqueous solution.

3.4 CONCLUSIONS

We demonstrate the reversible folding of a high molecular weight polymer in aqueous solution using only visible light. We also demonstrate the ability of our polymer system to respond to a second, non-thermal stimulus as it can undergo irreversible unfolding in response to acidic conditions. Folding behavior of poly1 was determined by a combination of illumination-dependent extinction spectroscopy experiments.

3.5 METHODS

All UV-Vis spectroscopy experiments were performed on an Agilent 8653 spectrometer using a home-built cuvette holder designed with windows for photoisomerization excitation perpendicular to the spectrometer source illumination path. Polymer and TMAB-TEG samples were diluted to an optical density of ~1 at $\lambda = 320$ nm for the polymer and $\lambda = 344$ nm for TMAB-TEG. As freshly prepared solutions were often found in a mixed trans/cis state, all solutions were photocycled between the cis and trans isomer through at least 3 cycles before measurements.

The intensity of the LEDs (470 nm Luxeon; 523 nm LED Engin) were measured by a a calibrated silicon photodiode at the same distance as the LED to the cuvette. Room temperature was confirmed prior to each run, and did not fluctuate more than 1 ^{o}C.

3.6 ACKNOWLEDGEMENTS

This work was supported by the University of Washington Office of Research. We acknowledge the support of the National Institute of Standards and Technology, U.S. Department of Commerce, in providing the neutron research facilities used in this work. Access to the NG-3 45 m very small-angle neutron scattering (SANS) instrument was provided by the Center for High Resolution Neutron Scattering, a partnership between the National Institute of Standards and

Technology and the National Science Foundation under Agreement No. DMR-2010792. Support for SANS measurements presented in this work was provided by the Department of Energy Office of Basic Energy Sciences under awards DE-SC0019911 (LDP) and the EFRC Center for the Science of Synthesis Across Scales (CSSAS) DE-SC0019288 (KL).

3.7 ABBREVIATIONS

βCD, beta-cyclodextrin; DCl, deuterium chloride; DOSY, diffusion ordered spectroscopy; ECT, 4-Cyano-4-(ethylsulfanylthiocarbonyl) sulfanyl pentanoic acid; IPF, integrated photokinetic factor; GPC, gel permeation chromatography; NMR, nuclear magnetic resonance; NOE, nuclear Overhauser effect; NOESY, nuclear Overhauser effect spectroscopy; RAFT, reversible addition-fragmentation chain-transfer polymerization; TMAB, tetramethoxyazobenzene.

3.8 REFERENCES

1. Qian, Z.; Ginger, D. S. Reversibly Reconfigurable Colloidal Plasmonic Nanomaterials. *J. Am. Chem. Soc.* **2017**, *139*, 5266–5276.
2. Samai, S.; Qian, Z.; Ling, J.; Guye, K. N.; Ginger, D. S. Optical Properties of Reconfigurable Polymer/Silver Nanoprism Hybrids: Tunable Color and Infrared Scattering Contrast. *ACS Appl. Mater. Interfaces* **2018**, *10*, 8976–8984.
3. Ding, T.; Valev, V. K.; Salmon, A. R.; Forman, C. J.; Smoukov, S. K.; Scherman, O. A.; Frenkel, D.; Baumberg, J. J. Light-induced actuating nanotransducers. *Proc. Natl. Acad. Sci. U. S. A.* **2016**, *113*, 5503–5507.
4. Mura, S.; Nicolas, J.; Couvreur, P. Stimuli-responsive nanocarriers for drug delivery. *Nat. Mater.* **2013**, *12*, 991–1003.
5. Wang, C. E.; Wei, H.; Tan, N.; Boydston, A. J.; Pun, S. H. Sunflower polymers for folate-mediated drug delivery. *Biomacromolecules* **2016**, *17*, 69–75.
6. Elias, P. Z.; Liu, G. W.; Wei, H.; Jensen, M. C.; Horner, P. J.; Pun, S. H. A functionalized, injectable hydrogel for localized drug delivery with tunable thermosensitivity: Synthesis and characterization of physical and toxicological properties. *J. Control. Release* **2015**, *208*, 76–84.
7. Wang, S.; Yue, L.; Li, Z. Y.; Zhang, J.; Tian, H.; Willner, I. Light-Induced Reversible Reconfiguration of DNA-Based Constitutional Dynamic Networks: Application to Switchable Catalysis. *Angew. Chemie - Int. Ed.* **2018**, *57*, 8105–8109.
8. Yoon, M.; Lee, J. E.; Jang, Y. J.; Lim, J. W.; Rani, A.; Kim, D. H. Comprehensive Study on the Controlled Plasmon-Enhanced Photocatalytic Activity of Hybrid Au/ZnO Systems Mediated by Thermoresponsive Polymer Linkers. *ACS Appl. Mater. Interfaces* **2015**, *7*, 21073–21081.
9. Wei, M.; Gao, Y.; Li, X.; Serpe, M. J. Stimuli-responsive polymers and their applications. *Polym. Chem.* **2017**, *8*, 127–143.
10. Schuler, B.; Eaton, W. A. Protein folding studied by single-molecule FRET. *Curr. Opin. Struct. Biol.* **2008**, *18*, 16–26.
11. Chen, J. I. L.; Chen, Y.; Ginger, D. S. Plasmonic nanoparticle dimers for optical sensing of DNA in complex media. *J. Am. Chem. Soc.* **2010**, *132*, 9600–9601.
12. Chen, J. I. L.; Durkee, H.; Traxler, B.; Ginger, D. S. Optical Detection of Protein in Complex Media with Plasmonic Nanoparticle Dimers. *Small* **2011**, *7*, 1993–1997.
13. Gränz, M.; Erlenbach, N.; Spindler, P.; Gophane, D. B.; Stelzl, L. S.; Sigurdsson, S. T.; Prisner, T. F. Dynamics of Nucleic Acids at Room Temperature Revealed by Pulsed EPR Spectroscopy. *Angew. Chemie - Int. Ed.* **2018**, *57*, 10540–10543.
14. Kelly, S. M.; Price, Nicholas, C. The application of circular dichroism to studies of protein folding and unfolding. *Biochim. Biophys. Acta* **1997**, *1338*, 161–185.
15. Freund, S. M. V.; Wong, K. B.; Fersht, A. R. Initiation sites of protein folding by NMR analysis. *Proc. Natl. Acad. Sci. U. S. A.* **1996**, *93*, 10600–10603.
16. Schmidt, B. V. K. J.; Fechler, N.; Falkenhagen, J.; Lutz, J. F. Controlled folding of synthetic polymer chains through the formation of positionable covalent bridges. *Nat. Chem.* **2011**, *3*, 234–238.
17. Desvergne, J. P.; Bouas-Laurent, H. Cation complexing photochromic materials involving bisanthracenes linked by a polyether chain. Preparation of a crown-ether by

photocycloisomerization. *J. Chem. Soc. Chem. Commun.* **1978**, 403–404 doi:10.1039/C39780000403.
18. Altintas, O.; Gerstel, P.; Dingenouts, N.; Barner-Kowollik, C. Single chain self-assembly: Preparation of α,ω-donor-acceptor chains via living radical polymerization and orthogonal conjugation. *Chem. Commun.* **2010**, *46*, 6291–6293.
19. Hosono, N.; Gillissen, M. A. J.; Li, Y.; Sheiko, S. S.; Palmans, A. R. A.; Meijer, E. W. Orthogonal self-assembly in folding block copolymers. *J. Am. Chem. Soc.* **2013**, *135*, 501–510.
20. Willenbacher, J.; Altintas, O.; Roesky, P. W.; Barner-Kowollik, C. Single-Chain Self-Folding of Synthetic Polymers Induced by Metal–Ligand Complexation. *Macromol. Rapid Commun.* **2014**, *35*, 45–51.
21. Yilmaz, G.; Uzunova, V.; Napier, R.; Remzi Becer, C. Single-Chain Glycopolymer Folding via Host−Guest Interactions and Its Unprecedented Effect on DC-SIGN Binding. *Biomacromolecules* **2018**, *19*, 3040–3047.
22. Inoue, Y.; Kuad, P.; Okumura, Y.; Takashima, Y.; Yamaguchi, H.; Harada, A. Thermal and photochemical switching of conformation of poly(ethylene glycol)-substituted cyclodextrin with an azobenzene group at the chain end. *J. Am. Chem. Soc.* **2007**, *129*, 6396–6397.
23. Jia, S.; Fong, W.-K.; Graham, B.; Boyd, B. J. Photoswitchable Molecules in Long-Wavelength Light-Responsive Drug Delivery: From Molecular Design to Applications. *Chem. Mater.* **2018**, *30*, 2873–2887.
24. Bandara, H. M. D.; Burdette, S. C. Photoisomerization in different classes of azobenzene. *Chem. Soc. Rev.* **2012**, *41*, 1809–1825.
25. Wang, D.; Wagner, M.; Butt, H. J.; Wu, S. Supramolecular hydrogels constructed by red-light-responsive host-guest interactions for photo-controlled protein release in deep tissue. *Soft Matter* **2015**, *11*, 7656–7662.
26. Titov, E.; Lysyakova, L.; Lomadze, N.; Kabashin, A. V.; Saalfrank, P.; Santer, S. Thermal Cis-to-Trans Isomerization of Azobenzene-Containing Molecules Enhanced by Gold Nanoparticles: An Experimental and Theoretical Study. *J. Phys. Chem. C* **2015**, *119*, 17369–17377.
27. Xu, B.; Qian, H.; Lin, S. Self-Assembly and Photoinduced Spindle-Toroid Morphology Transition of Macromolecular Double-Brushes with Azobenzene Pendants. **2020**, doi:10.1021/acsmacrolett.0c00079.
28. Ding, L.; Mao, H.; Xu, J.; He, J.; Ding, X.; Russell, T. P.; Robello, D. R.; Mis, M. Morphological study on an azobenzene-containing liquid crystalline diblock copolymer. *Macromolecules* **2008**, *41*, 1897–1900.
29. Jeong, S. P.; Renna, L. A.; Boyle, C. J.; Kwak, H. S.; Harder, E.; Damm, W.; Venkataraman, D. High Energy Density in Azobenzene-based Materials for Photo-Thermal Batteries via Controlled Polymer Architecture and Polymer-Solvent Interactions. *Sci. Rep.* **2017**, *7*, 1–12.
30. Wang, X.; Yang, Y.; Gao, P.; Yang, F.; Shen, H.; Guo, H.; Wu, D. Synthesis, Self-Assembly, and Photoresponsive Behavior of Tadpole-Shaped Azobenzene Polymers. *ACS Macro Lett.* **2015**, *4*, 1321–1326.
31. Liu, Y. C.; Ny, A. L. M. L.; Schmidt, J.; Talmon, Y.; Chmelka, B. F.; Lee, C. T. Photo-assisted gene delivery using light-responsive catanionic vesicles. *Langmuir* **2009**, *25*, 5713–5724.

32. Yan, Y.; Samai, S.; Bischoff, K. L.; Zhang, J.; Ginger, D. S. Photocontrolled DNA Hybridization Stringency with Fluorescence Detection in Heterogeneous Assays. *ACS Sensors* **2016**, *1*, 556–571.
33. Yan, Y.; Chen, J. I. L.; Ginger, D. S. Photoswitchable oligonucleotide-modified gold nanoparticles: Controlling hybridization stringency with photon dose. *Nano Lett.* **2012**, *12*, 2530–2536.
34. Zhao, Y.-L.; Stoddart, J. F. Azobenzene-Based Light-Responsive Hydrogel System. *Langmuir* **2009**, *25*, 8442–8446.
35. Tamesue, S.; Takashima, Y.; Yamaguchi, H.; Shinkai, S.; Harada, A. Photoswitchable supramolecular hydrogels formed by cyclodextrins and azobenzene polymers. *Angew. Chemie - Int. Ed.* **2010**, *49*, 7461–7464.
36. Tomatsu, I.; Hashidzume, A.; Harada, A. Photoresponsive Hydrogel System Using Molecular Recognition of a-Cyclodextrin. *Macromolecules* **2005**, *38*, 5223–5227.
37. Tarn, D.; Ferris, D. P.; Barnes, J. C.; Ambrogio, M. W.; Stoddart, J. F.; Zink, J. I. A reversible light-operated nanovalve on mesoporous silica nanoparticles. *Nanoscale* **2014**, *6*, 3335.
38. Ferris, D. P.; Zhao, Y.-L.; Khashab, N. M.; Khatib, H. A.; Stoddart, J. F.; Zink, J. I. Light-Operated Mechanized Nanoparticles. *J. Am. Chem. Soc.* **2009**, *131*, 1686–1688.
39. Bian, Q.; Chen, S.; Xing, Y.; Yuan, D.; Lv, L.; Wang, G. Host-guest self-assembly toward reversible visible-light-responsive switching for bacterial adhesion. *Acta Biomater.* **2018**, *76*, 39–45.
40. Ito, S.; Akiyama, H.; Mori, M.; Yoshida, M.; Kihara, H. Azobenzene-Containing Triblock Copolymer Adhesive Based on Light-Induced Solid–Liquid Phase Transition: Application to Bonding for Various Substrates. *Macromol. Chem. Phys.* **2019**, *1900105*, 1900105.
41. Wang, Y.; Ma, N.; Wang, Z.; Zhang, X. Photocontrolled reversible supramolecular assemblies of an azobenzene-containing surfactant with α-cyclodextrin. *Angew. Chemie - Int. Ed.* **2007**, *46*, 2823–2826.
42. Asanuma, H.; Liang, X.; Nishioka, H.; Matsunaga, D.; Liu, M.; Komiyama, M. Synthesis of azobenzene-tethered DNA for reversible photo-regulation of DNA functions: hybridization and transcription. *Nat. Protoc.* **2007**, *2*, 203–212.
43. Samanta, S.; Babalhavaeji, A.; Dong, M. X.; Woolley, G. A. Photoswitching of ortho-substituted azonium ions by red light in whole blood. *Angew. Chemie - Int. Ed.* **2013**, *52*, 14127–14130.
44. Sanchez, A. M.; Barra, M.; De Rossi, R. H. On the mechanism of the acid/base-catalyzed thermal cis-trans isomerization of methyl orange. *J. Org. Chem.* **1999**, *64*, 1604–1609.
45. Azuki, M.; Morihashi, K.; Watanabe, T.; Takahashi, O.; Kikuchi, O. Ab initio GB study of the acid-catalyzed cis-trans isomerization of methyl yellow and methyl orange in aqueous solution. *J. Mol. Struct. THEOCHEM* **2001**, *542*, 255–262.
46. Beharry, A. A.; Sadovski, O.; Woolley, G. A. Azobenzene Photoswitching without Ultraviolet Light. *J. Am. Chem. Soc.* **2011**, *133*, 19684–19687.
47. Wu, S.; Niu, L.; Shen, J.; Zhang, Q.; Bubeck, C. Aggregation-induced reversible thermochromism of novel azo chromophore-functionalized polydiacetylene cylindrical micelles. *Macromolecules* **2009**, *42*, 362–367.
48. Weis, P.; Wang, D.; Wu, S. Visible-Light-Responsive Azopolymers with Inhibited π-π Stacking Enable Fully Reversible Photopatterning. *Macromolecules* **2016**, *49*, 6368–6373.

49. Talaty, E. R.; Fargo, J. C. Thermal cis-trans-isomerization of substituted azobenzenes: A correction of the literature. *Chem. Commun.* **1967**, 65–66 doi:10.1039/C19670000065.
50. Rau, H.; Lüddecke, E. On the Rotation-Inversion Controversy on Photoisomerization of Azobenzenes. Experimental Proof of Inversion. *J. Am. Chem. Soc.* **1982**, *104*, 1616–1620.
51. Ikegami, T.; Kurita, N.; Sekino, H.; Ishikawa, Y. Mechanism of Cis-to-trans isomerization of azobenzene: Direct MD study. *J. Phys. Chem. A* **2003**, *107*, 4555–4562.
52. Samai, S.; Bradley, D. J.; Choi, T. L. Y.; Yan, Y.; Ginger, D. S. Temperature-Dependent Photoisomerization Quantum Yields for Azobenzene-Modified DNA. *J. Phys. Chem. C* **2017**, *121*, 6997–7004.
53. Yan, Y.; Wang, X.; Chen, J. I. L.; Ginger, D. S. Photoisomerization quantum yield of azobenzene-modified DNA depends on local sequence. *J. Am. Chem. Soc.* **2013**, *135*, 8382–8387.
54. Bortolus, P.; Monti, S. Cis ⇄ trans photoisomerization of azobenzene-cyclodextrin inclusion complexes. *J. Phys. Chem.* **1987**, *91*, 5046–5050.
55. Royes, J.; Courtine, C.; Lorenzo, C.; Lauth-De Viguerie, N.; Mingotaud, A. F.; Pimienta, V. Quantitative Kinetic Modeling in Photoresponsive Supramolecular Chemistry: The Case of Water-Soluble Azobenzene/Cyclodextrin Complexes. *J. Org. Chem.* **2020**, *85*, 6509–6518.

CHAPTER 4. IMPORTANCE OF SUBSTRATE-PARTICLE REPULSION FOR PROTEIN-TEMPLATED ASSEMBLY OF METAL NANOPARTICLES

This section is adapted with permission and minor modifications from "Importance of Substrate-Particle Repulsion for Protein-Templated Assembly of Metal Nanoparticles" Kathryn N. Guye, Hao Shen, Muammer Y. Yaman, Gerald Y. Liao, David Baker, and David S. Ginger, which has been submitted to Langmuir.

4.1 OVERVIEW

We study the protein-directed assembly of colloidal gold nanoparticles on *de novo* designed protein nanofiber templates. Using sequential assembly on glass substrates, we attach of positively-charged gold nanoparticles to protein nanofibers engineered to have a high density of negatively-charged surface residues. Using a combination of electron and optical microscopy, we measure the density of particle attachment and characterize binding specificity. By varying nanoparticle size and pH of the solution, we explore the importance of charge-dependent particle-fiber and particle-substrate interactions. We find an inverse correlation between particle size and attachment density to the protein nanofibers, attributed to the balance between size-dependent electrostatic particle-fiber attraction and particle-substrate repulsion. We show pH-dependent particle attachment density and binding specificity in relation to the protonation fraction of each assembly layer. Finally, we employ hyperspectral scattering microscopy to draw conclusions about particle density and interparticle spacings of optically-observable particle assemblies.

4.2 INTRODUCTION

In recent years, the assembly of hybrid organic/inorganic nanostructures has drawn notable interest as the result of many material designs with simple assembly strategies, yet highly functional products.[1,2] Such materials combine the optical and electronic functionality of inorganic materials, like plasmonic metal nanoparticles[3,4] or semiconductor quantum dots,[5,6] with the tailorable assembly of biologic[7–11] and biomimetic materials,[12–15] such as proteins,[16–18] peptides,[19–23] peptoids,[24,25] and DNA.[26–31] Using biomolecules to direct the local position and orientation of such inorganic materials clears a pathway for tailorable and scalable nanoparticle assemblies for functional purposes.[32–39]

While metal coordination complexes and covalent bonding of the inorganic material to its biological template are common due to the vast library of capping ligands and tailorable coordination sites[40–42] available for inorganic nanoparticles,[33,43–47] electrostatic-driven assembly takes advantage of a similar collection of surface ligands to induce both attractive and repulsive interactions between assembly elements to target specific binding sites.[48–52] In aqueous systems, electrostatic interaction energies can be altered by increasing the ionic strength of the solution, disrupting the electrical double layer and reducing the Debye screening length.[46,51,53] If assembly elements contain labile protons, the surface potential of those elements can be tuned by controlling the pH of the system, affecting both local and bulk material.[10,54,55] Lastly, electrostatic interaction energies are geometrically-dependent, determined by the shapes and sizes of the interacting surfaces.[56] As the synthesis of both bioorganic and inorganic materials have achieved highly tailorable designs, it becomes quite feasible to design a system that can electrostatically template a specific nanoparticle with high binding specificity.

Tailor-made biomolecules such as *de novo* designed proteins offer the opportunity to express certain surface residues of a particular charge at specific locations for functional patterning of the higher order protein structure.[57] Shen and coworkers recently reported the *de novo* design of the hierarchical synthesis of helical, high aspect ratio protein nanofibers with controllable length, diameter, and charge density. Not only are these structures unique, the high density of glutamic and aspartic acid residues at their surface yield a net negative surface charge under physiological conditions, providing energetically favorable interactions for electrostatic nanoparticle attachment.[58] Understanding the attachment of inorganic particles to engineered proteins is important both for understanding the fundamental design rules for hierarchical self-assembly, as well as for beginning to use such structures to produce materials with interesting optical, electrical, or chemical properties.

4.3 Results and Discussion

Herein, we study the templating of spherical gold nanoparticles on such protein nanofibers at the substrate interface. We identify an inverse relationship between particle size and attachment density, we tune the particle density and specific binding by varying pH, and use hyperspectral darkfield scattering microscopy to reveal both ensemble and local spectral differences for plasmonic nanoparticles assembled under varying pH conditions and attribute these line shape differences to particle binding specificity trends - showing that the assembly conditions can have a direct impact on the resulting optical properties.

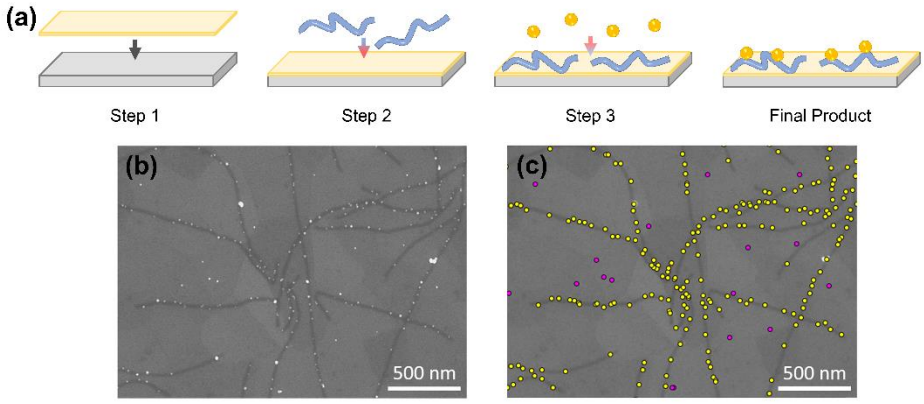

Figure 4.3.1. a) Schematic of the electrostatic layer-by-layer assembly. Step 1) A silica substrate with a thin layer of ITO is silanized with (3-aminopropyl)triethoxysilane (APTES). Step 2) Under aqueous conditions, net-negative protein nanofibers are drop cast onto the net-positive silane layer. Step 3) The protein-functionalized substrate is then exposed to a solution of net-positive, CTAB-capped gold nanoparticles, yielding b) 10 nm gold nanoparticle-protein nanofiber composites characterized by scanning electron microscopy, and c) a labeled micrograph of gold nanoparticles bound specifically to protein fibers (yellow dots), with limited nonspecific binding of particles to the silanized substrate (purple dots).

To study the assembly of protein nanofiber-templated gold nanoparticles, we propose a layer-by-layer assembly approach with alternating attractive charges to promote composite assembly and highly specific nanoparticle-to-nanofiber attachment. These structures were then observed by scanning electron microscopy (SEM). **Figure 4.3.1a.** shows the assembly schematic of the layer-by-layer approach. In step 1, we functionalize an ITO-coated silica substrate with (3-aminopropyl)triethoxysilane (APTES) by vapor deposition yielding a net positive charge at the surface of the substrate in aqueous solution. In step 2, an aliquot of 3 μM protein nanofiber solution was drop cast onto the silanized substrate. A combination of glutamic acid and aspartic acid residues at the surface of the helical fibers are deprotonated in the pH 8/25 mM Tris/75 mM NaCl buffer solution. Protein nanofibers were anchored randomly to the surface of the substrate through attractive van der Waals and electrostatic interactions. Excess protein solution was gently rinsed

from the substrate surface. Separately, a PDMS spacer was placed on a cleaned glass coverslip, creating a well atop the coverslip. Just before use, excess cetyltrimethlyammonium bromide (CTAB) was removed from the CTAB-capped gold nanoparticle solution by centrifugation and redispersal in Milli-Q Nanopure distilled water (18.2 MΩ.cm). The PDMS well was filled with the nanoparticle solution and placed on a flat surface. In step 3, the protein-functionalized substrate was then placed protein-side-down over the nanoparticle solution. The CTAB capping of the gold nanoparticles yield a net-positive surface potential (Supporting Information), generating van der Waals and electrostatic attraction between the nanoparticle and protein nanofiber, and strong electrostatic repulsion between the nanoparticle and silanized substrate, leading to specific binding of the particles to the protein surface. After incubation, the composite-assembled slide was removed from the excess nanoparticle solution, rinsed with a small amount of Milli-Q distilled water, and gently dried by flowing N_2 over the surface. Samples were analyzed by scanning electron microscopy, with consideration toward the large number of particles attached specifically to the protein fibers, as well as to the few nonspecifically bound gold nanoparticles to the silanized slides. **Figure 4.3.1b.** shows an electron micrograph of the assembled hybrid structure and nanoparticles color-coded in **Figure 4.3.1c.** as on-fiber (yellow dots) or off-fiber (purple dots). Following standard Derjaguin-Landau-Verwey-Overbeek (DLVO) theory[56], the two physical forces driving the formation of the protein-nanoparticle composites are van der Waals attraction and electrostatic double layer attraction between oppositely-charged moieties and repulsion between those like-charged. As such, the CTAB-capped gold nanoparticles are energetically more likely to bind to the negatively-charged nanofibers with both DLVO elements in the attractive regime, and less likely to nonspecifically bind to the substrate with only one attractive (van der Waals) force and one repulsive (electrostatic) force. However, it is possible for nonspecific binding

to occur if there are small regions of incomplete silanization on the ITO substrate or a nanoparticle has a lower capping ligand density, reducing the electrostatic repulsion and permitting binding through van der Waals attraction.

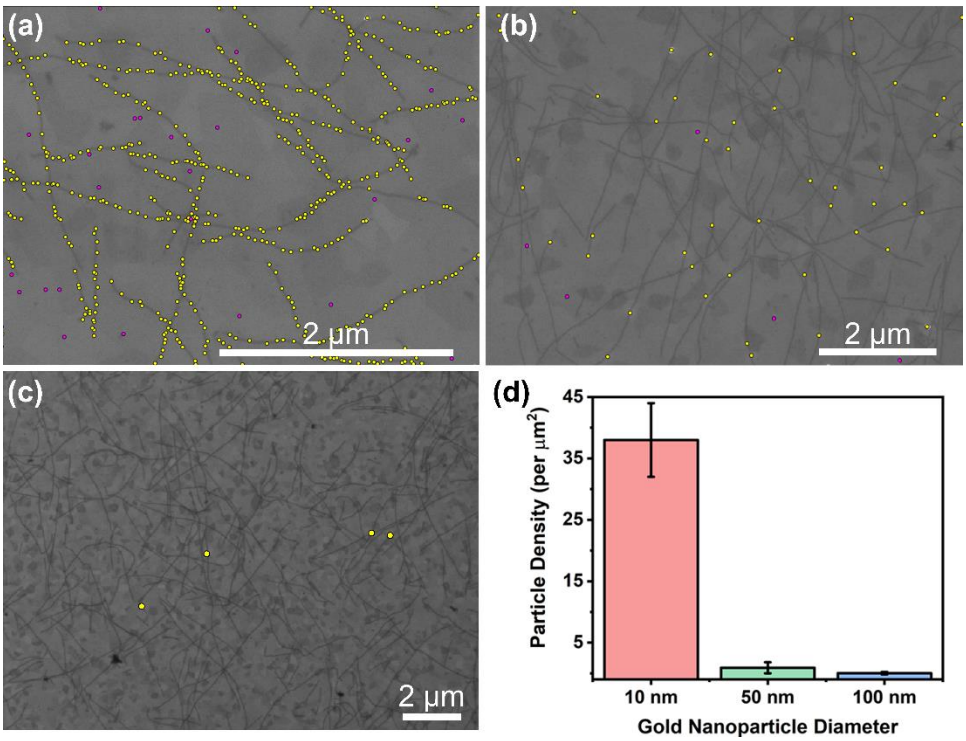

Figure 4.3.2. Gold nanoparticle electrostatic attachment density is size-dependent. Composites comprising a) 10 nm gold nanoparticles, b) 50 nm gold nanoparticles, and c) 100 nm gold nanoparticles were prepared and imaged by SEM. Yellow markers represent particles attached to the protein fibers and purple markers are particles attached to the substrate. d) Particle density in number of particles/µm2 by the diameter of the gold nanoparticles. Error bars represent Poisson counting distributions.

To examine the effect this substrate-particle repulsion has on nanoparticle attachment, we assembled the protein-particle composites with spherical gold nanoparticle of varying diameters. As shown in **Figure 4.3.2**, we assembled structures with 10 nm (Fig. 4.3.2a.), 50 nm (Fig. 4.3.2b.), and 100 nm (Fig. 4.3.2c.) CTAB-capped gold nanoparticles and show a representative, labeled electron micrograph for each sample. Gold nanoparticle attachment is notably qualitatively greater

for 10 nm gold nanoparticles, compared to 50 and 100 nm gold nanoparticles, with 10 nm gold nanoparticles outlining each nanofiber. In the 50 nm gold nanoparticle composites, at least one particle attaches to each nanofiber. In the 100 nm gold nanoparticle composites, however, most nanofibers remain bare. To quantify these results, we assume the protein fiber density is consistent between samples and record the areal attachment density as number of particles/μm^2. In Fig. 4.3.2d, we plot nanoparticle attachment density by the gold nanoparticle diameter to enumerate the significant difference in particle attachment. We observe 38 ± 6 10 nm gold nanoparticles/μm^2, 0.9 ± 0.9 50 nm gold nanoparticles/μm^2, and 0.03 ± 0.2 100 nm gold nanoparticles/μm^2, yielding a 10 nm:50 nm:100 nm gold nanoparticle ratio attachment of 1267:30:1. When $D_{particle} \sim D_{protein}$, the particle-substrate repulsion is more effectively screened by the negatively-charged protein, allowing the nanoparticles to electrostatically bind to the protein. As particle diameter increases to several times larger than the diameter of the protein fiber (50 nm), a larger surface area of the gold nanoparticle is no longer screened by the attractive force and repelled by the like-charged substrate, counteracting the attraction of the nanoparticle and protein, resulting in sparse nanoparticle attachment. Gold nanoparticles with a diameter nearly an order of magnitude larger than the protein (100 nm) are expected to experience only insignificant charge-screening from the protein, but significant repulsion from the like-charged substrate, yielding extremely sparse gold nanoparticle attachment to the nanofiber. As the gold nanoparticle must be able to approach the protein-functionalized substrate in order to attach to the substrate-anchored protein without being repelled away, and the diameter of the nanoparticle is the variable defining the substrate-gold nanoparticle repulsion, the size of the gold nanoparticle plays a significant role in the nanoparticle attachment density.

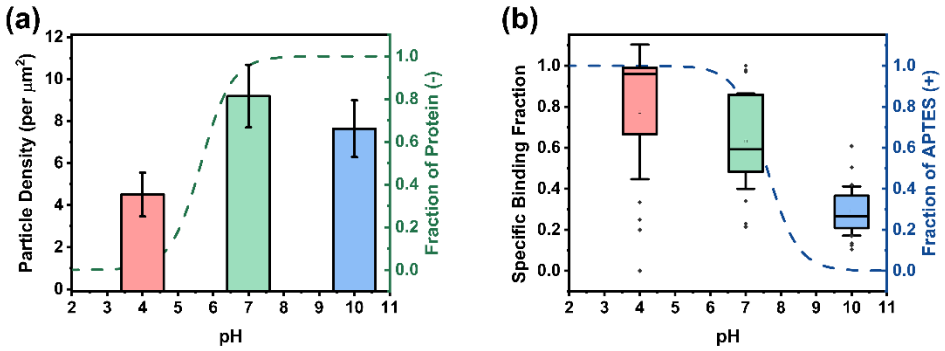

Figure 4.3.3. Particle density and specific binding of 10 nm diameter gold nanoparticles as a function of pH. a) Gold nanoparticle density on proteins (particles/μm^2) at pH 4 (red), 7 (green), and 10 (blue) compared to the calculated fraction of negatively-charged protein (dark green dashed line) as defined by its isoelectric point. b) Gold nanoparticle specific binding fraction at pH 4 (red), 7 (green), and 10 (blue) compared to the calculated fraction of protonated APTES (dark blue dashed line) as defined by its monolayer pK_a.

To achieve a "fine-tuning" of nanoparticle attachment in terms of both gold nanoparticle density as well as specific binding of gold nanoparticles to protein nanofibers, we varied the pH of the gold nanoparticle solution during step 3 of the assembly process, between anchoring the protein nanofibers to the silanized substrate and depositing gold nanoparticles. Here, the specific binding fraction is defined as:

$$Specific\ Binding\ Fraction = \frac{\#\ GNP\ on\ protein}{\#\ GNP\ on\ protein + \#GNP\ off\ protein} \quad (4.1)$$

Figure 4.3.3a. shows the areal density of 10 nm gold nanoparticles specifically-bound to the protein nanofibers at pH 4, 7, and 10. We find that the density of specifically-bound gold nanoparticles increases as the pH increases from pH 4 to pH 7, then decreases slightly as the pH increases from pH 7 to pH 10. Similarly, **Figure 4.3.3b.** shows the fraction of nanoparticles that are specifically attached at pH 4, 7, and 10. Comparing Fig. 4.3.3a and Fig. 4.3.3b we see that, as we increase the pH, the number of specifically-bound particles per square micron increases, however, the number of nonspecifically bound particles increases even more rapidly (Supporting

Information) meaning that the fraction of particles that are bound to the nanofibers, relative to those bound to the substrate decrease continuously as pH increases.

We explain this increase in attachment density and concomitant decrease in the specific binding fraction in the context of a competition between repulsion of the positively-charged gold nanoparticles from the positively-charged APTES-functionalized glass, and their attraction to the negatively-charged, carboxy-functionalized protein nanofibers, and the varying relative charge states of the APTES and protein nanofibers due to changing pH.

In Fig. 4.3.3a, we compare the attachment density of particles to the theoretical charge potential magnitude of the protein as defined by the protein isoelectric point, 5.66[59]. At low pH values, the carboxylic acid surface residues are nearly fully protonated, thus reducing the electrostatic attraction between the particles and protein, and even generating some particle-protein repulsion as the charge state of amino-functionalized residues remain positive. The small amount of attachment that does occur under acidic conditions is likely due to small local variations in pH and the incomplete protonation of the carboxy-surface residues. As the pH rises, the carboxy-surface residues become negatively-charged, providing more energetically-favorable binding sites for gold nanoparticles. This is consistent with the aforementioned observations that particle attachment increases with increasing pH.

In Fig. 4.3.3b, we compare the specific binding fraction of particles to the theoretical fraction of protonated APTES. At low pH values, the monolayer of APTES is completely protonated, generating a greater positive charge at the substrate surface. As such, the limited number of particles that did attach at low pH were almost all bound specifically to protein nanofibers. As pH increases, the amino group of APTES becomes deprotonated with a $pK_a = 7.6$.[60] As the amino group is deprotonated, the substrate becomes neutral, greatly reducing substrate-particle repulsion.

While the substrate does not become electrostatically attractive, the pre-existing interplay between dominant electrostatic repulsion and van der Waals attraction is no longer balanced, and attachment by van der Waals attraction becomes energetically favorable.

Having characterized the critical balance between electrostatic attraction and repulsion in the protein-templated nanoparticle assembly with attention to only the final composite product, we note the ability to observe the self-assembly process in real time provides more nuanced information about kinetic processes and critical timepoints of the assembly process.[61,62] As such, optical darkfield scattering microscopy is an enticing option for observing the self-assembly of gold nanoparticles, as a noninvasive, nondestructive method of observation, while taking advantage of the plasmonic optical properties of gold nanoparticles.[27,63] Although the 10 nm gold nanoparticle composites are densely concentrated on the protein nanofibers and likely show some collective scattering, the individual particles do not scatter strongly enough to be observable by darkfield microscopy for potential *in situ* measurements. Therefore, we turn to the larger 50 nm gold nanoparticle composites. Single 50 nm gold nanoparticles are just large enough to sufficiently scatter a measurable amount of light. While the nanoparticles are not highly concentrated on the protein nanofibers, we set out to determine if these particles followed similar trends to the 10 nm particles, with regard to pH, and whether these trends could be observed by their single-particle or multimer spectra. We prepared samples at pH 5, and 9, choosing pH conditions with the same ionic strength, yet a likelihood of attachment in both cases, and investigated the nanoparticle distribution by comparing the frequency of plasmon coupling observed via hyperspectral scattering microscopy.

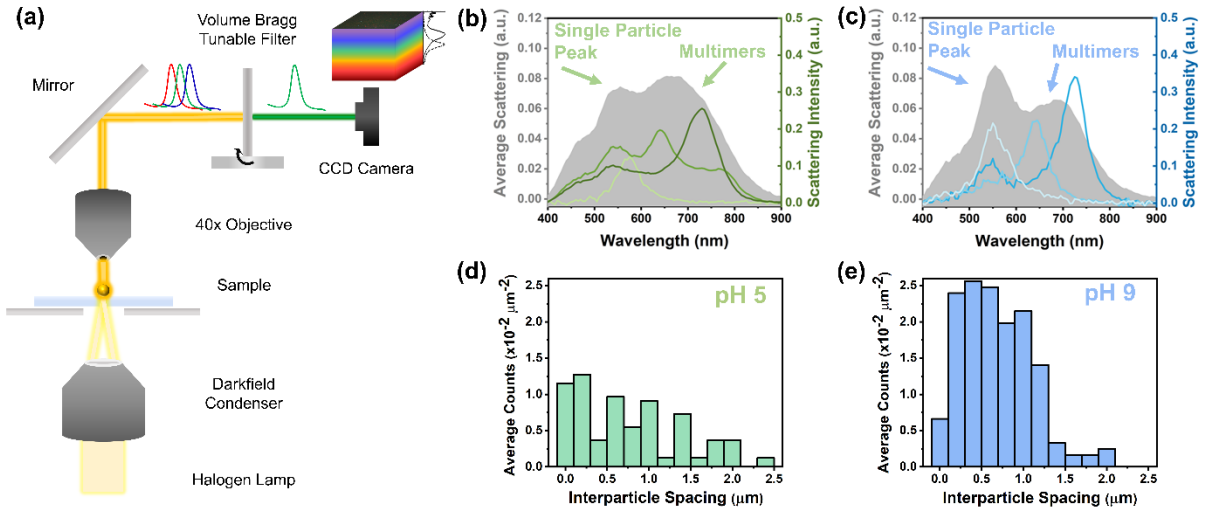

Figure 4.3.4. Hyperspectral darkfield scattering measurements of protein-templated 50 nm gold nanoparticles. a) Hyperspectral microscope schematic. (b, c) Average (grey) and single-spot (blue/green traces) scattering spectra for composite samples prepared at b) pH 5 and c) pH 9. (d, e) The distribution of center-to-center interparticle, nearest-neighbor distances for d) pH 5 and e) pH 9 as determined by electron micrograph image analysis.

In **Figure 4.3.4a.** we show a simplified schematic of the hyperspectral darkfield microscope. In the hyperspectral scattering experiment, the pre-assembled sample was illuminated with a halogen white light, and the scattered light was collected through a 40x objective lens. The scattered light was then passed through a volume Bragg tunable filter which, at a particular angle, meets the Bragg condition to only diffract a single wavelength of light (± 2 nm) which is collected as a monochromatic image by a CCD camera. As the filter turns, the incident angle of light changes, satisfying the Bragg condition for different wavelengths of light across the whole white light spectrum to build the hyperspectral data cube.[64]

In **Figure 4.3.4b.** and **Figure 4.3.4c.** the average spectrum of 50 nm gold nanoparticle-protein composites assembled at pH 5 and pH 9, respectively, are shown in grey. Individual spectra were identified from the data cube as described in the Experimental Methods section and averaged together while filtering out massive aggregates or dust particles that were particularly bright and

having an undue influence on the averaged spectra. In both samples, the average ensemble spectra are fairly broad, indicating a large variation of single gold nanoparticles and multimers of varying geometries. Both samples also had a large variety of single-spot spectra as show by the single-particle traces for each sample. Finally, a set of SEM micrographs of each sample were labeled to obtain the nanoparticle positions, and the distance to the two nearest-neighbors for each nanoparticle was identified. The distribution of the distances is shown in **Figure 4.3.4d** and **Figure 4.3.4e** for pH 5 and pH 9, respectively. Each particle was assigned two nearest-neighbors, as the best theoretical composite outcome would be 100% binding specificity of particles on fibers, in which case each particle would have another particle on either side of the one-dimensional protein nanofiber. True composites, however, have a combination of specifically- and nonspecifically-bound particles, and since particles' binding specificity could not be labeled in the hyperspectral dataset alone, we did not limit nearest-neighbors to either on or off the protein nanofiber.

The pH 5 sample was prepared in order to prevent nonspecific binding due to a fully-protonated silane monolayer, while the surface protein residues were deprotonated to some degree to allow for electrostatic particle attachment. Image analysis reveals a specific binding fraction of 0.90 for this sample. Notably, the single-particle peak around 550 nm appears only as a shoulder in the broad scattering across the entire white light spectrum. Although single-particle spectra are observed, a comparatively large population of various dimers and trimers are also observed. We attribute this to the reduced surface area the gold nanoparticles can occupy, confined to only the negatively-charged protein nanofibers and reduced nonspecific attachment to the substrate. Therefore, it is more likely a gold nanoparticle will attach within coupling distance of another gold nanoparticle. We see this confirmed by the nearest-neighbor distributions in the pH 5 sample in Fig. 4.3.4d, that the largest population of nearest-neighbors are within coupling distance, and then

experience a steady decrease for particles with far-away neighbors, which would have a spectral signature of a single particle. It is worth mentioning, however, this also indicates particle attachment energies may not be isotropic across the protein nanofiber and substrate. Heterogeneous silanization of the substrate may create larger energy barriers in certain regions, driving nanoparticles to attach in a further reduced area of the protein, increasing the likelihood of gold nanoparticle coupling. Additionally, the curvature of an entropically anchored protein nanofiber or its proximity to another nanofiber may also act to reduce the energy barrier and provide a more accessible binding site for multiple gold nanoparticles.

The pH 9 sample, which was predicted to have the greatest particle attachment density due to a deprotonated, neutral substrate and negatively-charged protein nanofiber, indeed exhibited a specific binding fraction of only 0.65, and the highest overall average pixel intensity at 550 nm, due to a large population of uncoupled, single particles both specifically-attached to the protein and nonspecifically to the silanized substrate, consistent with the 10 nm gold nanoparticle observations in alkaline conditions. In addition to the intense peak at 550 nm, a secondary peak is observed around 700 nm. This shoulder is attributed to the smaller population of coupled dimers and trimers which exhibit a strongly scattering, redshifted peak due to the additional plasmon mode along the longitudinal axis of the multimer. Since the longitudinal peak of multimers tends to scatter several times more intensely than the shorter, transverse plasmon mode, we can conclude that since this 700 nm shoulder is less intense than the 550 nm peak, the number of single particles far exceeds the number of coupled multimers. This is consistent with the distribution of nearest-neighbor distances in Fig. 4.3.4e, showing that while there is a population of nanoparticles within close proximity to one another, there is also a consistently large population of isolated, single particles.

We believe these observations are encouraging for further *in situ* assembly studies to investigate electrostatic, protein-driven nanoparticle assemblies, utilizing hyperspectral microscopy to probe gold nanoparticle attachment and interparticle orientations in real time. Due to the rapid acquisition of a large volume of data, however, parallel advancements in real time data analysis are needed.

4.4 CONCLUSIONS

Protein-templated gold nanoparticle assemblies were realized via a layer-by-layer assembly process using elements with alternating surface potentials. Size-dependent gold nanoparticle attachment density reveals particle-substrate repulsion is a dominating interaction, the magnitude of which determines whether particles are able to attach to the protein near the substrate interface. By varying the pH, we show control over the assembly parameters via the tunability of the fraction of protonated or deprotonated surface functional groups of each assembly component. Finally, we show hyperspectral scattering microscopy can be a powerful tool for optically analyzing such assemblies, potentially allowing for noninvasive *in situ* observation of the assembly process.

4.5 METHODS

Preparation of CTAB-Coated Gold Nanoparticles. A sample of citrate-capped gold nanoparticles (BBI Solutions Inc.) was centrifuged at 14,5000 rpm for 10 minutes. The supernatant of excess citrate was removed, and the particles were redispersed in Milli-Q Nanopure distilled water (18.2 MΩ.cm). A 0.3% w/w aqueous solution of cetyltrimethylammonium bromide (CTAB, TCI America), was added to the gold nanoparticles under rigorous stirring until the final

concentration of CTAB reached 0.15%. The solution was incubated while stirring overnight. Particles were stored in this 0.15% CTAB solution until use. Ligand exchange was confirmed by UV-Vis on an Agilent 8453 and zeta potential measured on a Malvern Zetasizer.

Preparation of *de novo* Designed Protein Nanofibers. Protein nanofibers were prepared following previously reported literature methods.[58]

Silane Functionalization of ITO Substrates. Silica substrates with a thin layer of indium tin oxide (ITO, Thin Film Devices) were cleaned by sonication in Micro-90 detergent, acetone, and isopropyl alcohol consecutively for ~15 minutes each to remove bulk contaminants. The substrates were then rinsed with ethanol and dried with N_2. To remove any lingering organic contaminants at the substrate surface, substrates were oxygen plasma cleaned for 1 minute. Substrates were then placed in a vacuum oven to be functionalized with (3-aminopropyl)triethoxysilane (APTES, Millipore Sigma) by vapor deposition at 100ºC for 1 hour. After 1 hour, substrates were sonicated for 5 minutes in isopropyl alcohol to remove excess silane.

Layer-by-Layer Protein-Directed Assembly of Gold Nanoparticles. A small aliquot of the stock solution of protein nanofibers was diluted to 3 µM with pH 8/25 mM Tris/75mM NaCl buffer solution. The diluted aliquot was then drop cast onto the silane-functionalized ITO substrate and rinsed with 1 mL of the buffer solution, and subsequently by a minimal amount of Milli-Q Nanopure water to remove excess salt, leaving a layer of randomly-positioned protein nanofibers anchored to the silane surface. Separately, a PDMS spacer (Grace BioLabs) was placed on a cleaned glass substrate, creating a well atop the coverslip. This well was filled with 36 µL of nanoparticle solution and 4 µL of Milli-Q Nanopure water or 4 µL of the variable solution for observation (e.g. the pH 10 sample, 36 µL of nanoparticles and 4 µL of $1x10^{-3}$ M NaOH in Milli-Q Nanopure water so that the final [NaOH] was $1x10^{-4}$ M). For the pH 7 sample, 4 µL of a $1x10^{-}$

^{3} M NaCl solution was used to keep the ionic strength of the system consistent with the pH 4 and pH 10 samples. The protein-functionalized slide was then placed protein-side-down onto the well to eliminate gravimetric sedimentation of the nanoparticles. Protein-functionalized substrates were incubated in the nanoparticle solution for 10 minutes for all samples. Slides were rinsed with a minimal amount of Milli-Q Nanopure water and very gently dried with N_2.

Scanning Electron Microscopy Imaging and Analysis. Composite samples were imaged by SEM on an FEI Sirion XL30 with an accelerating voltage of 5.0 V. From each sample, images were obtained at random, arbitrary locations across the deposited protein area. Number of particles attached to protein nanofibers and number of particles bound nonspecifically to the substrate surface were counted using ImageJ. Particles were considered bound to the protein if any part of the bright white nanoparticle appeared to overlap the dark nanofiber. If particles appeared aggregated, that is a clear boundary could not be identified, the aggregate was considered a single particle as it could not be determined if the particle aggregated in solution or after attaching to the protein. For average interparticle distances of the 50 nm gold nanoparticle composites, coordinate positions were identified using ImageJ particle analysis and their centroid positions were stored as the center-of-particle location. Using Python 3.7 programming, the center-to-center distance of the two nearest nanoparticle neighbors for each nanoparticle were identified.

Hyperspectral Darkfield Scattering Microscopy. Hyperspectral darkfield scattering data sets were obtained on a Photon Etc. IMA system, using a Nikon Ni-U upright microscope and a 40x objective lens (Nikon, NA 0.6). Full-field scattered light was passed through the tunable volume Bragg grating filter with a step size of 5 nm and integration time of 5 seconds/step. The scattered light at each wavelength step was collected by a CCD camera (Thorlabs, 1501M-US-TE), building the hyperspectral data cube by accumulating each wavelength slice. Scattering

spectra were normalized by dividing by a white light reference spectra and background corrected. Single-particle spectra were obtained using the Photon Etc. PHySpec software. The average particle spectra were obtained using a clustering algorithm using Google Colab programming to identify the central pixel of a diffraction-limited spot, and then average the pixel spectra of a given pixel neighborhood around the central pixel to be counted as one particle spectrum. All particle spectra were then averaged to obtain the ensemble average spectrum.

4.6 Acknowledgements

This material is based upon work supported by the US Department of Energy, Office of Science, Office of Basic Energy Sciences, as part of the Energy Frontier Research Centers program: CSSAS--The Center for the Science of Synthesis Across Scales under Award Number DE-SC0019288. Part of this work was conducted at the Molecular Analysis Facility, a National Nanotechnology Coordinated Infrastructure (NNCI) site at the University of Washington, which is supported in part by funds from the National Science Foundation (awards NNCI-2025489, NNCI-1542101), the Molecular Engineering & Sciences Institute, and the Clean Energy Institute. D.S.G. also acknowledges support from the University of Washington, Department of Chemistry Alvin L. and Verla R. Kwiram endowment. K.N.G. and M.Y.Y. acknowledge Dr. Sergei V. Kalinin at Oakridge National Lab for his valuable input for writing the Google Colab script for obtaining single particle spectra from the hyperspectral dataset.

4.7 Abbreviations

APTES, (3-aminopropyl)triethoxysilane; CCD, charged coupling device; CTAB, cetyltrimethylammonium bromide; DLVO, Derjaguin-Landau-Verwey-Overbeek; ITO, indium tin oxide; SEM, scanning electron microscopy

4.8 REFERENCES

1. Samai, S.; Qian, Z.; Ling, J.; Guye, K. N.; Ginger, D. S. Optical Properties of Reconfigurable Polymer/Silver Nanoprism Hybrids: Tunable Color and Infrared Scattering Contrast. *ACS Appl. Mater. Interfaces* **2018**, *10*, 8976–8984.
2. Ding, T.; Valev, V. K.; Salmon, A. R.; Forman, C. J.; Smoukov, S. K.; Scherman, O. A.; Frenkel, D.; Baumberg, J. J. Light-induced actuating nanotransducers. *Proc. Natl. Acad. Sci. U. S. A.* **2016**, *113*, 5503–5507.
3. Kreibig, U.; Vollmer, M. *Optical Properties of Metal Clusters*. (Springer Berlin Heidelberg, 1995). vol. 25.
4. Willets, K. A.; Van Duyne, R. P. Localized Surface Plasmon Resonance Spectroscopy and Sensing. *Annu. Rev. Phys. Chem.* **2007**, *58*, 267–297.
5. Woggon, U. *Optical Properties of Semiconductor Quantum Dots*. (Springer, Berlin, Heidelberg, 1997). vol. 136.
6. *Nanocrystal Quantum Dots* . (CRC Press, 2010).
7. Pyles, H.; Zhang, S.; De Yoreo, J. J.; Baker, D. Controlling protein assembly on inorganic crystals through designed protein interfaces. *Nature* **2019**, *571*, 251–256.
8. Zhang, S.; Chen, J.; Liu, J.; Pyles, H.; Baker, D.; Chen, C.; De Yoreo, J. J. Engineering Biomolecular Self-Assembly at Solid–Liquid Interfaces. *Adv. Mater.* **2020**, 1905784 doi:10.1002/adma.201905784.
9. Zhang, S.; Alberstein, R. G.; De Yoreo, J. J.; Tezcan, F. A. Assembly of a patchy protein into variable 2D lattices via tunable multiscale interactions. *Nat. Commun.* **2020**, *11*, 1–12.
10. Kumagai, S.; Yoshii, S.; Yamada, K. High-Density and Highly Surface Selective Adsorption of Protein--Nanoparticle Complexes by Controlling Electrostatic Interaction. *Jpn. J. Appl. Phys* **2006**, *45*, 4259.
11. Douglas, S. M.; Dietz, H.; Liedl, T.; Högberg, B.; Graf, F.; Shih, W. M. Self-assembly of DNA into nanoscale three-dimensional shapes. *Nature* **2009**, *459*, 414–418.
12. Lee, D. C.; Lamm, R. J.; Prossnitz, A. N.; Boydston, A. J.; Pun, S. H. Dual Polymerizations: Untapped Potential for Biomaterials. *Adv. Healthc. Mater.* **2019**, *8*, 1800861.
13. Cai, B.; Li, Z.; Chen, C. L. Programming Amphiphilic Peptoid Oligomers for Hierarchical Assembly and Inorganic Crystallization. *Acc. Chem. Res.* **2021**, *54*, 81–91.
14. Pashuck, E. T.; Seeman, N.; MacFarlane, R. Self-Assembly of bioinspired and biologically functional materials. *MRS Bull.* **2020**, *45*, 832–840.
15. Wang, S. T.; Gray, M. A.; Xuan, S.; Lin, Y.; Byrnes, J.; Nguyen, A. I.; Todorova, N.; Stevens, M. M.; Bertozzi, C. R.; Zuckermann, R. N.; Gang, O. DNA origami protection and molecular interfacing through engineered sequence-defined peptoids. *Proc. Natl. Acad. Sci. U. S. A.* **2020**, *117*, 6339–6348.
16. Lin, W.; Insley, T.; Tuttle, M. D.; Zhu, L.; Berthold, D. A.; Král, P.; Rienstra, C. M.; Murphy, C. J. Control of Protein Orientation on Gold Nanoparticles. *J. Phys. Chem. C* **2015**, *119*, 21035–21043.
17. Wangoo, N.; Suri, C. R.; Shekhawat, G. Interaction of gold nanoparticles with protein: A spectroscopic study to monitor protein conformational changes. *Appl. Phys. Lett.* **2008**, *92*, 133104.
18. Li, D.; Dong, Y.; Li, B.; Wu, Y.; Wang, K.; Zhang, S. Colorimetric sensor array with unmodified noble metal nanoparticles for naked-eye detection of proteins and bacteria.

Analyst **2015**, *140*, 7672–7677.
19. Hellner, B.; Lee, S. B.; Subramaniam, A.; Subramanian, V. R.; Baneyx, F. Modeling the Cooperative Adsorption of Solid-Binding Proteins on Silica: Molecular Insights from Surface Plasmon Resonance Measurements. *Langmuir* **2019**, *35*, 5013–5020.
20. Vogele, K.; List, J.; Pardatscher, G.; B. Holland, N.; C. Simmel, F.; Pirzer, T. Self-Assembled Active Plasmonic Waveguide with a Peptide-Based Thermomechanical Switch. *ACS Nano* **2016**, *10*, 11377–11384.
21. Coomber, D.; Bartczak, D.; R. Gerrard, S.; Tyas, S.; G. Kanaras, A.; Stulz, E. Programmed Assembly of Peptide-Functionalized Gold Nanoparticles on DNA Templates. *Langmuir* **2010**, *26*, 13760–13762.
22. Lu, J.; Xue, Y.; Bernardino, K.; Zhang, N.-N.; Gomes, W. R.; Ramesar, N. S.; Liu, S.; Hu, Z.; Sun, T.; de Moura, A. F.; Kotov, N. A.; Liu, K. Enhanced optical asymmetry in supramolecular chiroplasmonic assemblies with long-range order. *Science* **2021**, *371*, 1368–1374.
23. Whaley, S. R.; English, D. S.; Hu, E. L.; Barbara, P. F.; Belcher, A. M. Selection of peptides with semiconductor binding specificity for directed nanocrystal assembly. *Nature* **2000**, *405*, 665–668.
24. Monahan, M.; Cai, B.; Jian, T.; Zhang, S.; Zhu, G.; Chen, C.-L.; De Yoreo, J. J.; Cossairt, B. M. Peptoid-directed assembly of CdSe nanoparticles. *Nanoscale* **2021**, *13*, 1273–1282.
25. Yan, F.; Liu, L.; Walsh, T. R.; Gong, Y.; El-Khoury, P. Z.; Zhang, Y.; Zhu, Z.; De Yoreo, J. J.; Engelhard, M. H.; Zhang, X.; Chen, C. L. Controlled synthesis of highly-branched plasmonic gold nanoparticles through peptoid engineering. *Nat. Commun.* **2018**, *9*, 1–8.
26. Girard, M.; Wang, S.; Du, J. S.; Das, A.; Huang, Z.; Dravid, V. P.; Lee, B.; Mirkin, C. A.; de la Cruz, M. O. Particle analogs of electrons in colloidal crystals. *Science* **2019**, *364*, 1174–1178.
27. Samai, S.; Choi, T. L. Y.; Guye, K. N.; Yan, Y.; Ginger, D. S. Plasmonic Nanoparticle Dimers with Reversibly Photoswitchable Interparticle Distances Linked by DNA. *J. Phys. Chem. C* **2018**, *122*, 13363–13370.
28. Martens, K.; Binkowski, F.; Nguyen, L.; Hu, L.; Govorov, A. O.; Burger, S.; Liedl, T. Long- and short-ranged chiral interactions in DNA-assembled plasmonic chains. *Nat. Commun.* **2021**, *12*, 1–6.
29. Schreiber, R.; Do, J.; Roller, E. M.; Zhang, T.; Schüller, V. J.; Nickels, P. C.; Feldmann, J.; Liedl, T. Hierarchical assembly of metal nanoparticles, quantum dots and organic dyes using DNA origami scaffolds. *Nat. Nanotechnol.* **2014**, *9*, 74–78.
30. Chen, J. I. L.; Chen, Y.; Ginger, D. S. Plasmonic nanoparticle dimers for optical sensing of DNA in complex media. *J. Am. Chem. Soc.* **2010**, *132*, 9600–9601.
31. Nykypanchuk, D.; Maye, M. M.; Van Der Lelie, D.; Gang, O. DNA-guided crystallization of colloidal nanoparticles. *Nature* **2008**, *451*, 549–552.
32. Huang, S.; Qi, J.; deQuilettes, D. W.; Huang, M.; Lin, C.; Bardhan, N. M.; Dang, X.; Bulović, V.; Belcher, A. M. M13 Virus-Based Framework for High Fluorescence Enhancement. *Small* **2019**, *15*, 1901233.
33. D. Merg, A.; C. Boatz, J.; Mandal, A.; Zhao, G.; Mokashi-Punekar, S.; Liu, C.; Wang, X.; Zhang, P.; C. A. van der Wel, P.; L. Rosi, N. Peptide-Directed Assembly of Single-Helical Gold Nanoparticle Superstructures Exhibiting Intense Chiroptical Activity. *J. Am. Chem. Soc.* **2016**, *138*, 13655–13663.

34. Nam, Y. S.; Magyar, A. P.; Lee, D.; Kim, J. W.; Yun, D. S.; Park, H.; Pollom, T. S.; Weitz, D. A.; Belcher, A. M. Biologically templated photocatalytic nanostructures for sustained light-driven water oxidation. *Nat. Nanotechnol.* **2010**, *5*, 340–344.
35. Mokashi-Punekar, S.; Brooks, S. C.; Hogan, C. D.; Rosi, N. L. Leveraging Peptide Sequence Modification to Promote Assembly of Chiral Helical Gold Nanoparticle Superstructures. *Biochemistry* **2021**, *60*, 1044–1049.
36. Nie, Z.; Petukhova, A.; Kumacheva, E. Properties and emerging applications of self-assembled structures made from inorganic nanoparticles. *Nat. Nanotechnol.* **2010**, *5*, 15–25.
37. Lukach, A.; Thérien-Aubin, H.; Querejeta-Fernández, A.; Pitch, N.; Chauve, G.; Méthot, M.; Bouchard, J.; Kumacheva, E. Coassembly of gold nanoparticles and cellulose nanocrystals in composite films. *Langmuir* **2015**, *31*, 5033–5041.
38. Jiang, W.; Qu, Z. B.; Kumar, P.; Vecchio, D.; Wang, Y.; Ma, Y.; Bahng, J. H.; Bernardino, K.; Gomes, W. R.; Colombari, F. M.; Lozada-Blanco, A.; Veksler, M.; Marino, E.; Simon, A.; Murray, C.; Muniz, S. R.; de Moura, A. F.; Kotov, N. A. Emergence of complexity in hierarchically organized chiral particles. *Science* **2020**, *368*, 642–648.
39. Ghotra, G.; Nguyen, B. K.; Chen, J. I. L. DNA-functionalized gold nanoparticles with toehold-mediated strand displacement for nucleic acid sensors. *ACS Appl. Nano Mater.* **2020**, *3*, 10123–10132.
40. Sun, S.; Yang, S.; Xin, H. L.; Nykypanchuk, D.; Liu, M.; Zhang, H.; Gang, O. Valence-programmable nanoparticle architectures. *Nat. Commun.* **2020**, *11*, 1–10.
41. Mei, B. C.; Oh, E.; Susumu, K.; Farrell, D.; Mountziaris, T. J.; Mattoussi, H. Effects of ligand coordination number and surface curvature on the stability of gold nanoparticles in aqueous solutions. *Langmuir* **2009**, *25*, 10604–10611.
42. Rossi, L. M.; Fiorio, J. L.; Garcia, M. A. S.; Ferraz, C. P. The role and fate of capping ligands in colloidally prepared metal nanoparticle catalysts. *Dalt. Trans.* **2018**, *47*, 5889–5915.
43. Mucic, R. C.; Storhoff, J. J.; Letsinger, R. L.; Mirkin, C. A. A DNA-based method for rationally assembling nanoparticles into macroscopic materials. *Nature* **1997**, *382*, 607.
44. Wang, S.; Zhang, Y.; Qin, X.; Zhang, L.; Zhang, Z.; Lu, W.; Liu, M. Guanosine Assembly Enabled Gold Nanorods with Dual Thermo- And Photoswitchable Plasmonic Chiroptical Activity. *ACS Nano* **2020**, *14*, 6087–6096.
45. Park, S. Y.; Lytton-Jean, A. K. R.; Lee, B.; Weigand, S.; Schatz, G. C.; Mirkin, C. A. DNA-programmable nanoparticle crystallization. *Nature* **2008**, *451*, 553–556.
46. Lewis, D. J.; Gabrys, P. A.; Macfarlane, R. J. DNA-Directed Non-Langmuir Deposition of Programmable Atom Equivalents. *Langmuir* **2018**, *34*, 14842–14850.
47. Murphy, C. J.; Sau, T. K.; Gole, A. M.; Orendorff, C. J.; Gao, J.; Gou, L.; Hunyadi, S. E.; Li, T. Anisotropic metal nanoparticles: Synthesis, assembly, and optical applications. *J. Phys. Chem. B* **2005**, *109*, 13857–13870.
48. Chen, Q.; Bae, S. C.; Granick, S. Staged self-assembly of colloidal metastructures. *J. Am. Chem. Soc.* **2012**, *134*, 11080–11083.
49. Sastry, M.; Rao, M.; Ganesh, K. N. Electrostatic assembly of nanoparticles and biomacromolecules. *Acc. Chem. Res.* **2002**, *35*, 847–855.
50. Sharma, N.; Top, A.; Kiick, K. L.; Pochan, D. J. One-Dimensional Gold Nanoparticle Arrays by Electrostatically Directed Organization Using Polypeptide Self-Assembly.

Angew. Chemie Int. Ed. **2009**, *48*, 7078–7082.
51. Hueckel, T.; Hocky, G. M.; Palacci, J.; Sacanna, S. Ionic solids from common colloids. *Nature* **2020**, *580*, 487–490.
52. Leunissen, M. E.; Christova, C. G.; Hynninen, A. P.; Royall, C. P.; Campbell, A. I.; Imhof, A.; Dijkstra, M.; Van Roij, R.; Van Blaaderen, A. Ionic colloidal crystals of oppositely charged particles. *Nature* **2005**, *437*, 235–240.
53. Adamczyk, Z.; Nattich-Rak, M.; Sadowska, M.; Michna, A.; Szczepaniak, K. Mechanisms of nanoparticle and bioparticle deposition - Kinetic aspects. *Colloids Surfaces A Physicochem. Eng. Asp.* **2013**, *439*, 3–22.
54. Sivasankar, S.; Subramaniam, S.; Leckband, D. Direct molecular level measurements of the electrostatic properties of a protein surface. *Proc. Natl. Acad. Sci. U. S. A.* **1998**, *95*, 12961–12966.
55. Honig, B.; Nicholls, A. Classical electrostatics in biology and chemistry. *Science* **1995**, *268*, 1144–1149.
56. Israelachvili, J. N. *Intermolecular and Surface Forces*. (Elsevier Science & Technology, 2010).
57. Huang, P. S.; Boyken, S. E.; Baker, D. The coming of age of de novo protein design. *Nature* **2016**, vol. 537 320–327.
58. Shen, H.; Fallas, J. A.; Lynch, E.; Sheffler, W.; Parry, B.; Jannetty, N.; Decarreau, J.; Wagenbach, M.; Vicente, J. J.; Chen, J.; Wang, L.; Dowling, Q.; Oberdorfer, G.; Stewart, L.; Wordeman, L.; De Yoreo, J.; Jacobs-Wagner, C.; Kollman, J.; Baker, D. De novo design of self-assembling helical protein filaments. *Science* **2018**, *362*, 705–709.
59. Gasteiger, E.; Hoogland, C.; Gattiker, A.; Duvaud, S.; Wilkins, M. R.; Appel, R. D.; Bairoch, A. The Proteomics Protocols Handbook. *Proteomics Protoc. Handb.* **2005**, 571–608 doi:10.1385/1592598900.
60. Zhang, H.; He, H. X.; Wang, J.; Mu, T.; Liu, Z. F. Force titration of amino group-terminated self-assembledmonolayers using chemical force microscopy. *Appl. Phys. A Mater. Sci. Process.* **1998**, *66*, 269–271.
61. Ou, Z.; Wang, Z.; Luo, B.; Luijten, E.; Chen, Q. Kinetic pathways of crystallization at the nanoscale. *Nat. Mater.* **2020**, *19*, 450–455.
62. Yao, L.; Ou, Z.; Luo, B.; Xu, C.; Chen, Q. Machine Learning to Reveal Nanoparticle Dynamics from Liquid-Phase TEM Videos. *ACS Cent. Sci.* **2020**, *6*, 1421–1430.
63. K. Jain, P.; Huang, W.; A. El-Sayed, M. On the Universal Scaling Behavior of the Distance Decay of Plasmon Coupling in Metal Nanoparticle Pairs: A Plasmon Ruler Equation. *Nano Lett.* **2007**, *7*, 2080–2088.
64. Blais-Ouellette, S.; Daigle, O.; Taylor, K. The imaging Bragg tunable filter: a new path to integral field spectroscopy and narrow band imaging. in *Ground-based and Airborne Instrumentation for Astronomy* (SPIE, 2006). (eds. McLean;I. S. & Iye;M.) vol. 6269 62695H.

CHAPTER 5. CONCLUSIONS AND FUTURE DIRECTIONS

5.1 CONCLUSIONS

This dissertation presents work on the optical characterization of metal nanoparticles, bio-inspired organic materials, and their combined composite structures, with particular focus on the simulated optical properties of nanoparticles of varying geometries interacting with their local environment, the photokinetics and photoisomerization quantum yield of a photoresponsive, host-guest polymer with self-folding behavior, and electrostatic assembly of protein-templated gold nanoparticles.

In Chapter 2, we presented finite-difference time-domain simulations for three different systems including orientation- and intersurface distance-dependent silver nanoprism dimers, gold nanorods of varying sizes, and silver nanoprisms coupled to a two-dimensional lead halide perovskite film. In the first section, nanoparticle dimers comprising of either two gold nanospheres or two silver nanorprisms were modeled to simulate the redshift of the localized surface plasmon resonance (LSPR) as a function of interparticle distance. For the anisotropic silver nanoprisms, we varied the orientation of one nanoprism with respect to the other, demonstrating a range of fractional redshifts dependent on the geometry of interactions. The redshift of all silver nanoprism dimers, however, were greater than for the 50 nm gold nanospheres at the same surface-to-surface distance. These simulations therefore showed the incredible redshift with novel infrared scattering of nanorpisms tethered to the thermoresponsive microsphere at temperatures above the transition temperature, in comparison to previous simulations, was due to plasmonic coupling between particles. We then simulated two nanorods with similar LSPR energies, but a notably different scattering contribution to the extinction coefficient. Calculated absorption and extinction cross-

sections were compared to a new method for obtaining photoacoustic absorption spectra, showing incredible accuracy of the spectrometer to measure purely the absorption of light by the nanoparticles, even in a high-scattering environment. Finally, we simulated silver nanoprisms coupled to a 2D lead halide perovskite thin film. From these simulations, we were able to deconvolve contributions of geometric scattering, a hybrid exciton-photon Fano resonance, and the strongly-coupled plasmon resonance from the experimental spectra. We were also able to calculate the Rabi splitting of the coupled nanoparticles to reveal a strongly-coupled system, when these values were otherwise unattainable due to the strong scattering contribution of the exciton-photon Fano resonance. In general, finite-difference time-domain simulations provide an excellent, reliable mechanism for supporting experimental results and providing insight into optical properties which are unattainable from experiments directly.

Next, in Chapter 3, we studied a photoresponsive, self-folding triblock copolymer driven by a host-guest cyclodextrin-azobenzene derivative pair. The azobenzene derivative, tetramethoxyazobenzene (TMAB), is nonpolar in its trans-state and therefore includes the cyclodextrin to mediate hydrophobic interactions in the aqueous solution. However, after undergoing photoisomerization to the cis-state, TMAB excludes cyclodextrin. This photoisomerization, however, is sterically hindered by the surrounding cyclodextrin walls, thereby lowering its photoisomerization quantum yield. In this chapter, we show the light-induced reversibility and cyclability of the TMAB chromophore both tethered and untethered to the polymer, propose a modified method for quantifying the fraction of cis-state TMAB when the extinction coefficient is not obtainable by NMR for the polymer system, and confirm a reduction in the quantum yield of the TMAB in the polymer, confirming self-inclusion and therefore self-folding.

Finally, in Chapter 4, we study the electrostatically-driven protein-templating of small gold nanoparticles near the surface of a charged substrate. Guided by the long-studied Derjaguin-Landau-Verwey-Overbeek (DLVO) theory, we identify a critical balance between electrostatic attraction and repulsion to offset nonspecific van der Waals attraction while still permitting specific attachment for nanoparticle assembly. We show nanoparticle size directs substrate-particle repulsion, resulting in larger nanoparticles being driven away from the protein-functionalized substrate while the substrate-particle repulsion of small nanoparticles is better screened by the protein-particle attraction, therefore attach at a much higher density. Local surface potentials can also be tuned by varying the pH of solution. As pH increases, the protein nanofibers become more negatively charged yielding an increase in protein-particle attraction, however the silane layer on the substrate concomitantly becomes deprotonated, yielding a larger degree of nonspecific binding of particles, thus a balance must be identified between strong protein-particle attraction and substrate-particle repulsion. Finally, using larger nanoparticles, we measure the scattering spectra of nanoparticle-protein composites, yielding results comparable to those observed by electron microscopy. This suggests optical microscopy, even with poorly-attaching nanoparticles, may yield critical insight into the assembly dynamics by *in situ* observation.

5.2 Future Directions

Stimulus-Responsive Self-Folding Polymers

In Chapter 3, we discussed the analysis of a self-folding polymer driven by a photoresponsive host-guest complex. Moving forward, such a functional material which demonstrates stimulus-responsive, reversible volume actuation is an attractive target for preparing nanoparticle dimers with the ability to vary the interparticle distance, such as in the work by Samai et al. in 2018 using

azobenzene-modified DNA hairpin loops[1]. Polymers, compared to DNA, tend to be more stable in various solution conditions and benefit from the ability to economically produce large quantities with specialized designs and functionalities. In order to employ this self-folding polymer to manufacture photoreversible nanoparticle dimer actuators, a gold-binding functional group, such as a thiol, would need to be added to each end of the copolymer. Due to the strong surface charge of typical citrate-capped nanoparticles after synthesis (typically -30 meV), ligand exchange on the nanoparticle surface may be needed in order to passivate such repulsive charges, allowing the nanoparticles to dimerize via a short-distance tether. One neutralizing capping ligand would be a thiolated polyethylene glycol chain which readily binds to the surface of the nanoparticle and nearly neutralizes the surface charge. We had previously also proposed capping the nanoparticle with a thiolated photoinduced ring-opening spiropyran which under one wavelength of light is neutral and by excitation of another becomes ionized[2]. Such a controllable neutral-to-charged capping ligand is a strong contender for achieving maximum actuation by aiding the entropy of diffusion of the unfolding of the polymer with nanoparticle surface-to-surface repulsion. However, careful consideration of this system would need to be taken to avoid undesirable absorbance overlap between the azobenzene and spiropyran. The spiropyran is also known to function as a photoacid, releasing a proton via the ring-opening step. Consequently, too significant of a drop in pH results in a locked "super-trans" state in which the azo bond of tetramethoxyazobenzene (TMAB) becomes protonated and due to the formal charge, can no longer include cyclodextrin. In order to generate discrete dimers, a layer-by-layer self-assembly approach would likely yield best results, drop casting one set of nanoparticles, then drop casting the thiolated self-folding polymer under green light illumination to drive the TMAB into a majority cis-state resulting in unfolding and reducing the opportunity for the polymer to chelate the first nanoparticle, and finally an

incubation set of more gold nanoparticles to generate nanoparticle dimers. The actuation of dimers could then be studied in solution by hyperspectral darkfield microscopy, with an obvious redshift and split peak of nanoparticle dimers form in the folded state of the polymer following known plasmon ruler modeling. Dimers would also be characterized by scanning electron microscopy. A layer-by-layer approach would also benefit the ability to replace the second nanoparticle with a semiconductor quantum dot, resulting in fluorescence quenching in the folded state, and quantum dot fluorescence in the unfolded state. Composites formed in solution would also be of interest, however it is less likely to form an abundance of discrete two-particle dimers rather than large aggregates, however such large aggregates may also demonstrate interesting photoresponsive behavior, and could also increase the likelihood of photothermal heating driving the cis-to-trans transition of TMAB or other azobenzene-derivative with a greater sensitivity to temperature.

Finally, another synthetic design which has recently generated interest, is the tethering of a fluorophore and quenching molecule, both organic, to either end of an actuatable polymer chain, resulting in observable fluorescence in the unfolded state and quenched fluorescence in the folded state, similar to the plasmonic particle-semiconductor quantum dot design. Using an all-organic system however, prevents potential complications of surface-surface repulsion reducing dimerization yield and can be incorporated directly during the synthetic preparation. Finally, such a system could be blended into an elastic hydrogel matrix and investigated for mechanical, stress-induced actuation[3].

Bio-Templated Assembly of Nanoparticles and Photomediated pH Control

In Chapter 4 we discussed the electrostatically-driven templating of small gold nanoparticles by protein nanofibers and characterized the balance between electrostatic attraction and repulsion as the main driving force of assembly. In this chapter we showed preliminary data that assembly

could be monitored via hyperspectral darkfield microscopy, with conclusions relating to interparticle spacing, attachment density, and binding specificity being drawn from the ensemble average scattering spectra of the sample. Currently, efforts are being done to use machine learning to automate a rapid prediction of nanoparticle position, geometry, and orientation from the individual scattering spectra (much like the information obtainable from the plasmon ruler model or finite-difference time-domain simulations). Moving forward, in 2019, Boyken and coworkers designed *de novo* protein structures with an embedded pH-responsive histidine network which engages in hydrogen bonding at high solution pH values allowing the protein to assemble in various structures such as a nanofiber[4]. However, when the pH is dropped, the histidine becomes protonated, and the steric hindrance between residues breaks apart the protein. If the pH is increased, the histidine will deprotonate again, and the protein microstructure will reform. Taking what we have learned from the project described in Chapter 4, we plan to tag such pH-responsive protein nanofibers with gold nanoparticles and observe *in situ* the formation, denaturation, and reformation of the fiber structure as a response to solution pH. Furthermore, we have the opportunity to combine our knowledge of photoresponsive materials such as described in Chapter 3 by introducing a photoacid to the protein-nanoparticle composite solution. Photoacids are chromophores which, in their photoinduced excited state, results in a weakened chromophore-labile proton bond and a pKa drop of usually several pH units. Photoacids can be irreversible (often used in acid-catalyzed free radical polymer syntheses) or reversible by diffusion of the proton back to the host chromophore in the dark. The benefits of using a photoacid compared to manual titration of an acid or base into the composite buffer are 1) the solution does not become over diluted, as the proteins require a Goldilocks-zone of monomer concentration in order to form the nanofiber microstructures; 2) the ionic strength does not monotonically increase with each acid-base cycling

reducing the rapidity of cycling fatigue of the system; 3) whereas manual titration of solution must affect the entire solution, light can be focused to the nanoscale, triggering pH actuation over a small, local area, allowing for nanoscale control over assembly and disassembly of protein structures; and finally 4) a wide range of photoacid exists commercially and synthetically allowing for selection of illumination wavelength and pH-drop including the ground state and excited state pK_a values. As many biomolecules assemble via a combination of hydrophobic and electrostatic interactions, the ability to trigger assembly and disassembly via a non-contact stimulus would be extendable to many systems including proteins, peptides, peptoids, and even bio-inspired polymers.

Lastly, as the organization of nanoparticle arrays is highly desirable due to the many optoelectronic functionalities of such structures, the *de novo* design of the proteins may be further adjusted to selectively bind a secondary particle, such as a semiconductor quantum dot, in between gold particles or as a Janus material with two discrete functionalities on either end in order to benefit from plasmonic-enhanced absorption, emission, or even strong coupling between emitter and plasmonic cavity. Alternatively, the templated nanoparticles, if sufficiently close to one another to create rows of nanoantennae, could be used as nanosensors or have a material with a strong excitonic transition such as butylammonium lead iodide or a J-aggregate dye spin cast over top of the templated particles for further investigation of plasmonic materials coupled to two-dimensional excitonic emitters.

5.3 REFERENCES

1. Samai, S.; Choi, T. L. Y.; Guye, K. N.; Yan, Y.; Ginger, D. S. Plasmonic Nanoparticle Dimers with Reversibly Photoswitchable Interparticle Distances Linked by DNA. *J. Phys. Chem. C* **2018**, *122*, 13363–13370.
2. Ipe, B. I.; Mahima, S.; Thomas, K. G. Light-induced modulation of self-assembly on spiropyran-capped gold nanoparticles: A potential system for the controlled release of amino acid derivatives. *J. Am. Chem. Soc.* **2003**, *125*, 7174–7175.
3. Creusen, G.; Schmidt, R. S.; Walther, A. One-Component DNA Mechanoprobes for Facile Mechanosensing in Photopolymerized Hydrogels and Elastomers. *ACS Macro Lett.* **2021**, 671–678 doi:10.1021/acsmacrolett.1c00211.
4. Boyken, S. E.; Benhaim, M. A.; Busch, F.; Jia, M.; Bick, M. J.; Choi, H.; Klima, J. C.; Chen, Z.; Walkey, C.; Mileant, A.; Sahasrabuddhe, A.; Wei, K. Y.; Hodge, E. A.; Byron, S.; Quijano-Rubio, A.; Sankaran, B.; King, N. P.; Lippincott-Schwartz, J.; Wysocki, V. H.; Lee, K. K.; Baker, D. De novo design of tunable, pH-driven conformational changes. *Science* **2019**, *364*, 658–664.

APPENDIX A.

2.3 Theoretical Modeling of Plasmonic Coupling of Anisotropic Silver Nanoprisms with Varying Interparticle Distances and Orientations

3D geometric design of gold nanorods for FDTD simulations

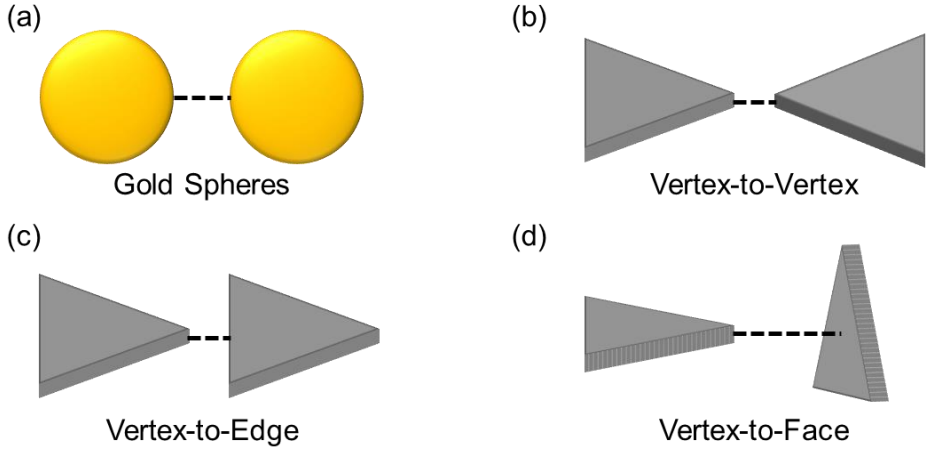

Figure A1. Depiction of a) gold nanosphere and b-d) silver nanoprism dimers with varying interparticle orientations for the anisotropic nanoparticles including b) vertex-to-vertex, c) vertex-to-edge, and d) vertex-to-face. The dashed line between each particle indicates the distance interparticle spacing was measured.

Varying the Size and LSPR of Silver Nanoprisms in PNIPAM Composites

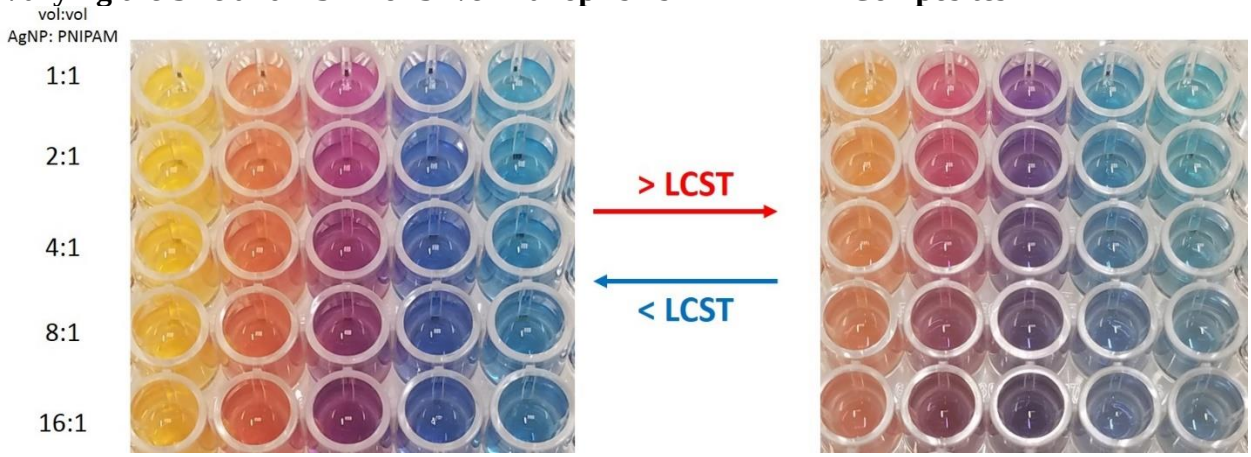

Figure A2. Silver nanoprisms of varying sizes (left-to-right, small-to-large) synthesized by synthesis method 2 as discussed in the main text, and combined with PNIPAM microspheres at varying ratios The temperature of solutions, all at once, were raised above the LCST to show a dramatic color change for each sample, with the most noticeable changes with the smaller nanoparticles.

2.4 Theoretical Modeling o Size-Dependent Absorption and Scattering of Gold Nanorods in Comparison with Photoacoustic Spectroscopy

Synthesis of gold nanorods

The synthesis of gold nanorods followed a modified method described by Ye *et al.*[1] All reagents were obtained from Sigma Aldrich unless otherwise specified.

Seed Solution. 5 mL of 0.5 mM $HAuCl_4$ was added to a solution of 0.2 M CTAB (TCI America) while stirring (600 rpm) using MilliQ Nanopure water for all solutions. A fresh solution of 0.01 M $NaBH_4$ (Stream Chemicals) was then prepared. 600 µL was diluted to 1 mL and added to the Au-CTAB solution. The solution quickly turned from pale yellow to brown while it stirred for two minutes. At this time, the stirring was stopped and the seed solution aged for 30 minutes while the growth solution was prepared.

Growth Solution. 0.7 g of CTAB and 0.1234 g of sodium oleate were added to a centrifuge tube with 25 mL of MilliQ water and heated to ~70^{o}C with occasional shaking. When the CTAB and sodium oleate were completely dissolved, the solution was moved to an Erlenmeyer flask and the temperature reduced to 30^{o}C. 1.8 mL of 4 mM $AgNO_3$ while stirring to obtain a homogenous mixture, and then left undisturbed without stirring for 15 minutes. Then 25 mL of 1 mM $HAuCl_4$ was added under rigorous stirring (600-700 rpm). The solution aged while stirring, and over this time, the color faded from pale yellow to colorless. After 90 minutes, the pH was adjusted by adding 150 µL of concentrated HCl (12.1M) and the solution was left stirring at 400 rpm for 15 minutes. 125 µL of 0.064 M ascorbic acid was then added and stirred vigorously (700 rpm) for 30 seconds.

With the seed solution and growth solution finishing aging at the same time, 35 µL of seed solution was injected into the growth solution. The reaction mixture was stirred for 30 seconds and

then left undisturbed at 30°C for twelve hours. The final product of gold nanorods were characterized by UV-Vis spectroscopy on an Agilent 8453 UV-Vis spectrometer and scanning electron microscopy on an FEI Sirion with a 5 kV accelerating voltage. Gold nanorods were purified from the reaction mixture by centrifugation at 12,500 rpm for 10 minutes and then redispersed in a 50 mM CTAB solution until use.

Characterization of gold nanorods

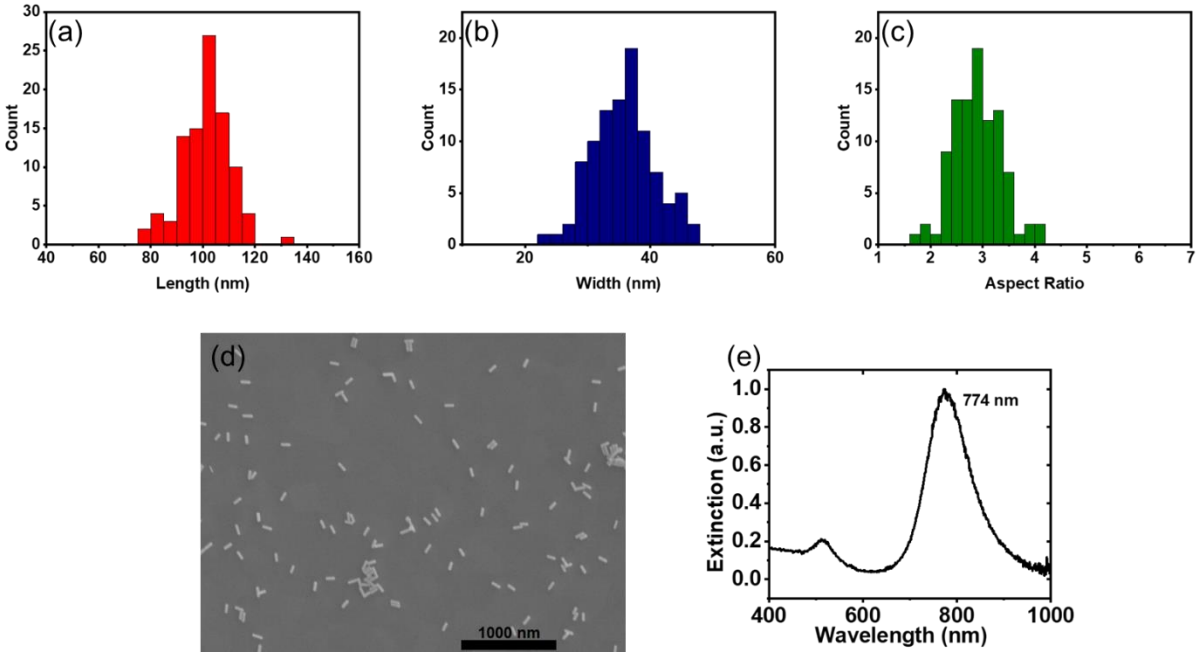

Figure A3. a) Histogram of the distribution of nanoparticle lengths. b) Histogram of the distribution of nanoparticle widths. c) Histogram of the average aspect ratio. d) Representative electron micrograph of the gold nanorods on an ITO substrate. e) Normalized UV-Vis extinction curve of the nanoparticle solution.

The length and width of 75 nanoparticles were measured using ImageJ image analysis software. The average length of the nanorods was 99.7 ± 9 nm, the average width was 35 ± 5 nm, and the average aspect ratio was 2.9 ± 0.4. The average length divided by the average width was 2.9 in good agreement with the average of individual particle aspect ratios. With a gaussian distribution on each histogram and an agreement between the calculated aspect ratios, it can be

determined this sample of gold nanorods is monodisperse with regard to shape and size. The UV-Vis extinction spectrum also indicates a monodisperse sample with a fairly narrow longitudinal peak centered at 774 nm and a low intensity transverse peak at 514 nm indicating a low or nonexistent population of contaminant gold nanospheres.

3D geometric design of gold nanorods for FDTD simulations

Finite-difference time-domain simulations are capable of calculating scattering and absorption spectra of plasmonic nanoparticles with an astounding accuracy if the material optical properties are well-characterized, and if the refractive index of the environment and geometry of the nanoparticle are accurate.

The 40 nm nanorod has a more traditional geometry from gold nanorods with spherically rounded ends. Therefore, the 40 nm nanorod was constructed in the Lumerical software by overlapping two gold spheres of an 11.1 nm diameter at the edges of a gold cylinder with a diameter of 11.1 nm and a length of 31.8 nm, yielding a final length of the nanorod of 42.9 nm. In order for this structure to behave as a single rod-like nanoparticle during the simulations, a mesh order must be set for the two spheres and cylinder. In Lumerical, when objects overlap, the object with a lower mesh order will take priority, and the software will ignore the overlapping portion of the object with the higher mesh order. Therefore, each sphere was given a mesh order of 3 and the cylinder a mesh order of 2, yielding a final rod-like nanoparticle as a cylindrical structure with hemisphere caps at each end as shown below:

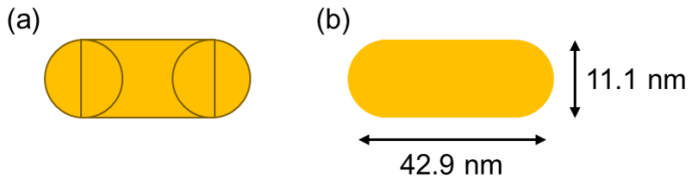

Figure A4. a) Design of the 40 nm gold nanorod with independent objects. b) Final simulated object after mesh order is considered (images not drawn to scale).

For the 100 nm gold nanorod, however, the edges were flatter and less spherical. To construct such a nanoparticle, we made the spheres larger and positioned them closer to the center of the cylinder to where the cross section of the cylinder matched the cross section of the sphere. Because the actual curvature of the nanoparticle edges was not measured, this was done by trial and error until the peak position of the nanoparticle was consistent with the peak in the extinction spectrum with a spherical diameter of 60 nm.

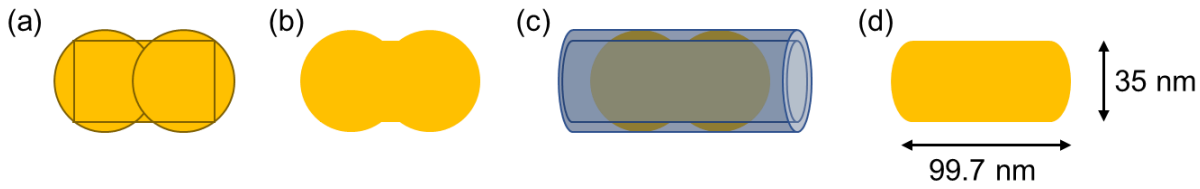

Figure A5. a) Design of the 100 nm gold nanorod with independent objects, including larger spheres at the edges. b) A barbell-shaped nanoparticle after considering the mesh order of the gold objects alone. c) The barbell-shaped nanoparticle in a ring with inner diameter of 35 nm and a refractive index of 1.33. d) Final simulated object after mesh order of the gold and dielectric ring are considered (images not drawn to scale).

Enlarging the spheres, however, yields a barbell-shaped nanoparticle that is not consisten with the nanorod structure. To remove the extra parts of the sphere around the cylinder, a ring with an inner diameter of 35 nm and an outer diameter of 60 nm was placed over the nanoparticle with the same central axis. We set the material of the ring as a dielectric material with a refractive index of 1.33 to match the water background, and the lowest mesh order. Therefore, the excess gold around

the edges from the enlarged spheres would be discarded, leaving only the gold inside the inner diameter of the ring to be accounted for. The final mesh orders of each object was 4 for the spheres, 3 for the cylinder, and 2 for the ring. The shape of the nanoparticle was confirmed with a refractive index monitor to ensure proper meshing.

Finally, a background index of 1.33 was set to simulate the refractive index of an aqueous solution at room temperature.

2.5 Theoretical Modeling of Exciton-Photon Fano Resonance and Rabi Splitting of Single Silver Nanoprisms Coupled to 2D Perovskite Films

Effect of grain diameter on BAPI scattering

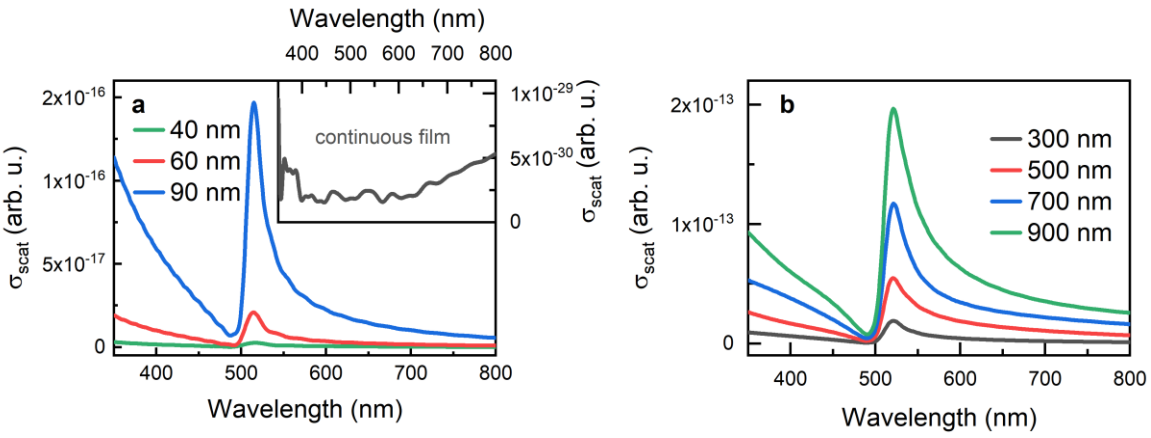

Figure A6. FDTD simulations of the scattering cross section of 2D BAPI nanodisks with 20 nm thickness und different diameters of a) 40 nm - 90 nm and b) 300 nm - 900 nm). The inset in a) depicts the scattering of a continuous BAPI film.

To account for variations of the scattering contribution of BAPI due to a distribution of BAPI grain sizes in the actual film, we simulated the scattering coefficient of small and large BAPI grains. Even a few tens of nanometers difference in grain diameter increases the scattering coefficient by an order of magnitude for the smaller grains. The larger grains, which have very high scattering coefficients comparatively, do not increase scattering with size as rapidly. Based on the size of grain or grains the nanoparticle overlaps in the coupled sample, the BAPI scattering contribution may vary, and therefore cannot be background corrected from the nanoparticle spectra.

Silver Nanoprism Characterization

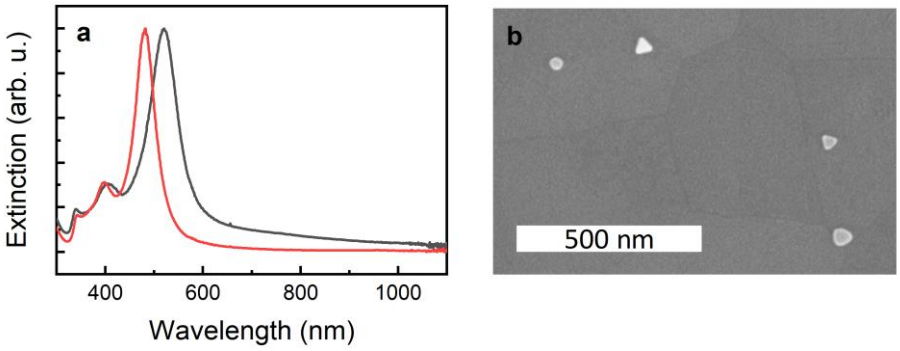

Figure A7. Silver nanoparticles. a) Normalized extinction spectra of two different batches of AgNP in aqueous solution. B) SEM images of AgNP on an indium tin oxide substrate

Silver nanoparticles were prepared by modified methods as previously described by Mirkin an coworkers[2,3] and described in the main text.

REFERENCES

1. Ye, X.; Jin, L.; Caglayan, H.; Chen, J.; Xing, G.; Zheng, C.; Doan-Nguyen, V.; Kang, Y.; Engheta, N.; Kagan, C. R.; Murray, C. B. Improved size-tunable synthesis of monodisperse gold nanorods through the use of aromatic additives. *ACS Nano* **2012**, *6*, 2804–2817.
2. Xue, C.; Mirkin, C. A. pH-switchable silver nanoprism growth pathways. *Angew. Chemie - Int. Ed.* **2007**, *46*, 2036–2038.
3. Jin, R.; Cao, Y. C.; Hao, E.; Métraux, G. S.; Schatz, G. C.; Mirkin, C. A. Controlling anisotropic nanoparticle growth through plasmon excitation. *Nature* **2003**, *425*, 487–490.

APPENDIX B.

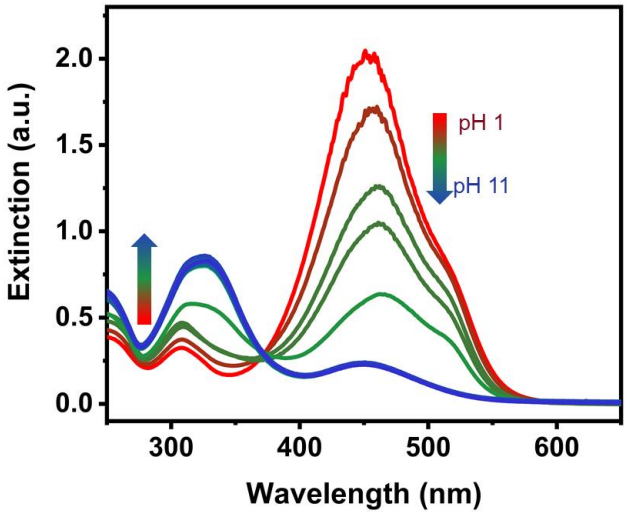

Figure B1a. pH-dependent extinction spectra of **poly1** from pH 1 (red) to pH 11 (blue).

Under very acidic conditions, the azo group in TMAB is protonated. This proton then forms an additional hydrogen bond with the nearest methoxy group to form a psuedo third ring as shown below.

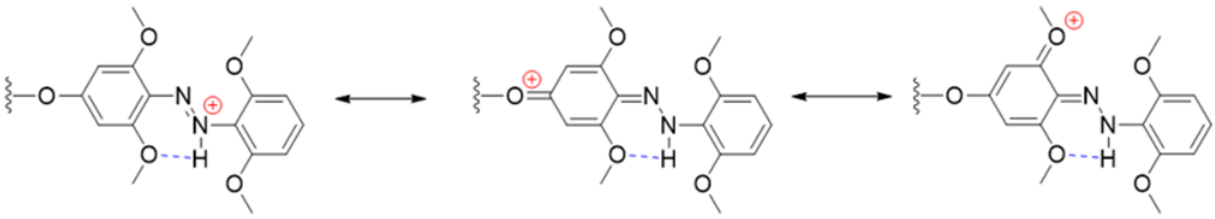

Figure B1b. Resonance structures of the protonated TMAB moiety.

The formation of this additional psuedo ring is observed in the extinction spectrum as the growth of a peak at 465 nm and decrease of the π-π* peak at 320 nm, consistent with previous reports[1,2]. The formation of the hydrogen bond stabilizes the azo group in the trans isomer. It also,

however, results in a formal charge on the previous apolar TMAB group, thereby inhibiting inclusion as discussed in the main text.

Aggregation behavior of TMAB in solution

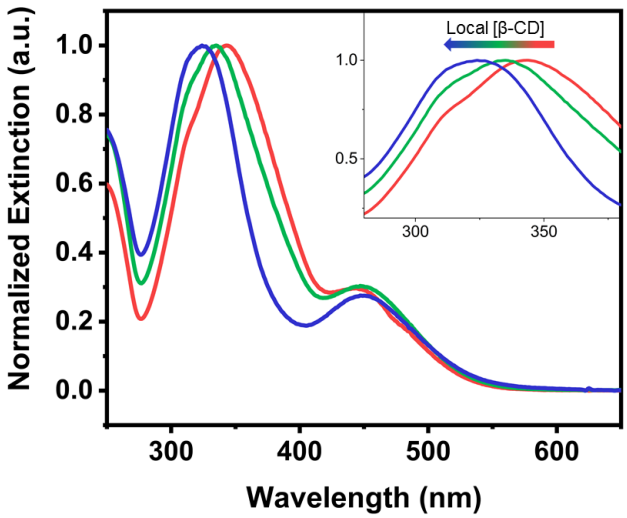

Figure B2a. Normalized extinction spectra of poly(1) (blue), TMAB-TEG (red), and TMAB-TEG in excess HP-βCD. All dissolved in 9:1 H2O:D2O. Inset is an enlarged view of the π- π* extinction peak positions, showing a blueshift of the peak position with respect to the local concentration of βCD.

We observed a redshift of the π- π* extinction peak for TMAB-TEG (red trace) compared to the spectrum of poly(1) (blue trace) and reported literature spectra for the TMAB chromophore. Redshifting of chromophore spectra is indicative of intermolecular dipole alignment as the result of aggregation. When in the presence of excess HP-βCD, this peak blueshifts towards the poly(1) position, indicating the inclusion complex disrupts aggregate formation. By tethering both TMAB and βCD together by polymerization, we increase the local concentration of βBD, preventing the significant formation of chromophore aggregation via the inclusion complex.

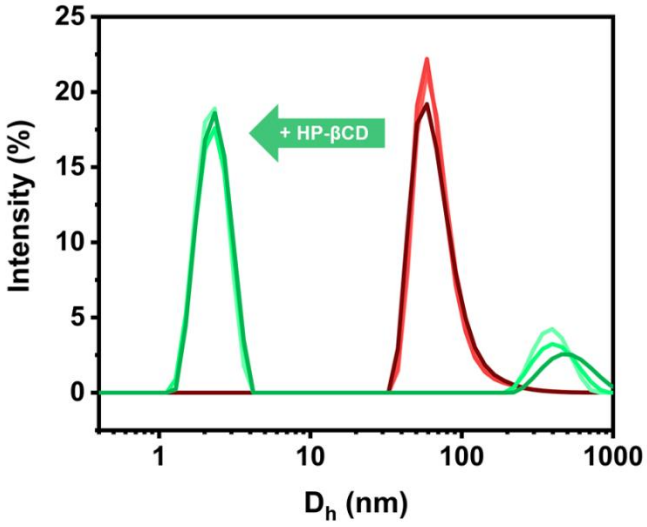

Figure B2b. Dynamic light scattering spectra of a sample of TMAB-TEG in 9:1 H_2O:D_2O (red), and a sample of TMAB-TEG in excess HP-βCD in 9:1 H_2O:D_2O (green).

We further used dynamic light scattering (DLS) spectroscopy to confirm the presence of aggregates and the deaggregation by cyclodextrin inclusion complexation. Without HP-βCD, larger aggregates form in solution. With the addition of HP-βCD, the aggregates dissociate almost completely. It is consistent with the extinction spectra, however, that the aggregates do not dissociate entirely to single molecules.

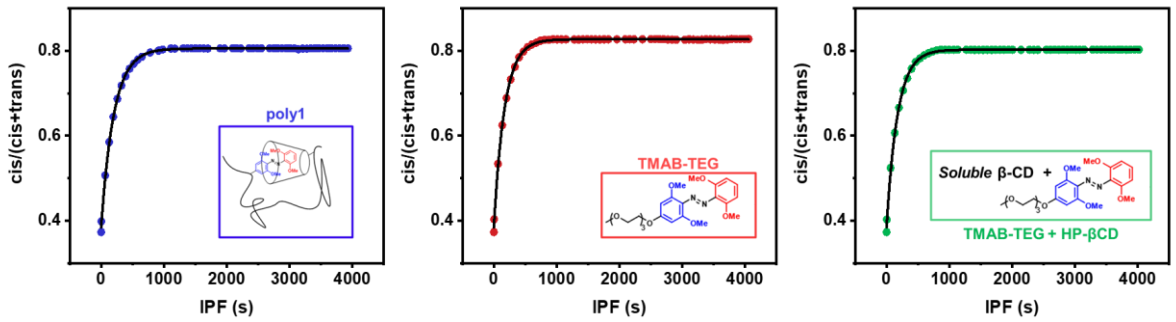

Figure B3. Representative photokinetic plots of poly1 (blue), TMAB-TEG (red), and TMAB-TEG with HP-βCD. Photokinetic fits, as described in the main text, are shown as a black trace.

	y_0	y_∞	A	Φ_{Trans}
poly1	0.385 ± 0.001	0.806 ± 0.0004	4.95E-3 ± 4E-5	**0.28 ± 0.01**
TMAB-TEG	0.386 ± 0.002	0.827 ± 0.0004	5.85E-3 ± 6E-5	**0.34 ± 0.01**
TMAB-TEG+CD	0.386 ±0.002	0.803 ± 0.0004	5.66E-3 ± 5E-5	**0.32 ± 0.01**

Table B1. Average values for fit-extracted constants an variable of photokinetic traces and the calculated quantum yield for the trans-to-cis isomerization. Errors on the extracted variables are calculated by the standard deviation of the fits from three samples. Error on the quantum yield is measured by the variance observed in the quantification of trans vs. cis ratios by the integration method.

Each sample was photocycled three times before photokinetic measurements. Sampling frequency vs. illumination intensity were balanced in order to avoid lamp-induced photoconversion and allow for sufficient sampling time. Photokinetic plots were fit as described in the main text and by Samai et al.[3] Quantum yield values were consistent with previously reported results for cyclodextrin-included azobenzene in an aqueous solution.[4]

REFERENCES

1. Zheng, X.; Bian, Q.; Ye, C.; Wang, G. Visible light-, pH-, and cyclodextrin-responsive azobenzene functionalized polymeric nanoparticles. *Dye. Pigment.* **2019**, *162*, 599–605.
2. Samanta, S.; Babalhavaeji, A.; Dong, M. X.; Woolley, G. A. Photoswitching of ortho-substituted azonium ions by red light in whole blood. *Angew. Chemie - Int. Ed.* **2013**, *52*, 14127–14130.
3. Samai, S.; Bradley, D. J.; Choi, T. L. Y.; Yan, Y.; Ginger, D. S. Temperature-Dependent Photoisomerization Quantum Yields for Azobenzene-Modified DNA. *J. Phys. Chem. C* **2017**, *121*, 6997–7004.
4. Royes, J.; Courtine, C.; Lorenzo, C.; Lauth-De Viguerie, N.; Mingotaud, A. F.; Pimienta, V. Quantitative Kinetic Modeling in Photoresponsive Supramolecular Chemistry: The Case of Water-Soluble Azobenzene/Cyclodextrin Complexes. *J. Org. Chem.* **2020**, *85*, 6509–6518.

APPENDIX C.

Supporting Information 1 – Extinction and Zeta Potential Measurements of Gold Nanoparticles

Diameter	$\lambda_{max,\ citrate}$	$\lambda_{max,\ CTAB}$	$\zeta_{citrate}$	ζ_{CTAB}
10 nm	518 nm	524 nm	-33 mV	+31 mV
50 nm	530 nm	533 nm	-45 mV	+42 mV
100 nm	574 nm	577 nm	-51 mV	+34 mV

Table C1. Table showing the localized surface plasmon resonance (LSPR, λ_{max}) and average zeta potential (ζ) for all nanoparticle solutions before and after the citrate-to-CTAB ligand exchange for each nanoparticle solution. A slight redshift in the LSPR is expected when the replacement ligand has a higher refractive index than the original ligand.[1] The zeta potential of the nanoparticles changes from negative-to-positive with the ligand exchange, consistent with a citrate-to-CTAB ligand exchange. We note that zeta potential of the CTAB-capped nanoparticles do not trend with nanoparticle size. Therefore, increased repulsion due to an increasing zeta potential magnitude is not the cause of the reduced attachment of larger nanoparticles, rather the size-dependent substrate-particle repulsion determines attachment density.

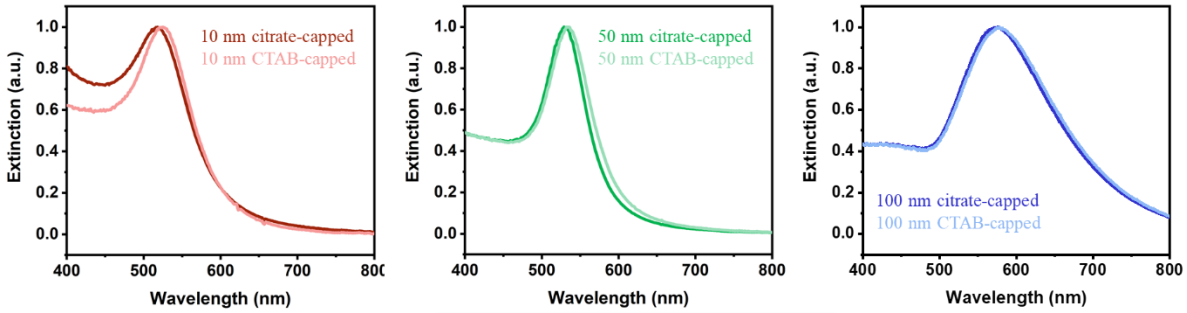

Figure C1. Normalized extinction plots of the 10 nm (red), 50 nm (green), and 100 nm (blue) gold nanoparticles as citrate-capped (darker traces) and after the citrate-to-CTAB ligand exchange (lighter traces). As discussed above, a slight redshift due to the CTAB capping is observed for each sample, however the line shape of the extinction traces do not drastically change, indicating nanoparticles remain monodisperse after ligand exchange.

Supporting Information 2 – Description of Intersurface Forces During Step 3 of the Assembly Process

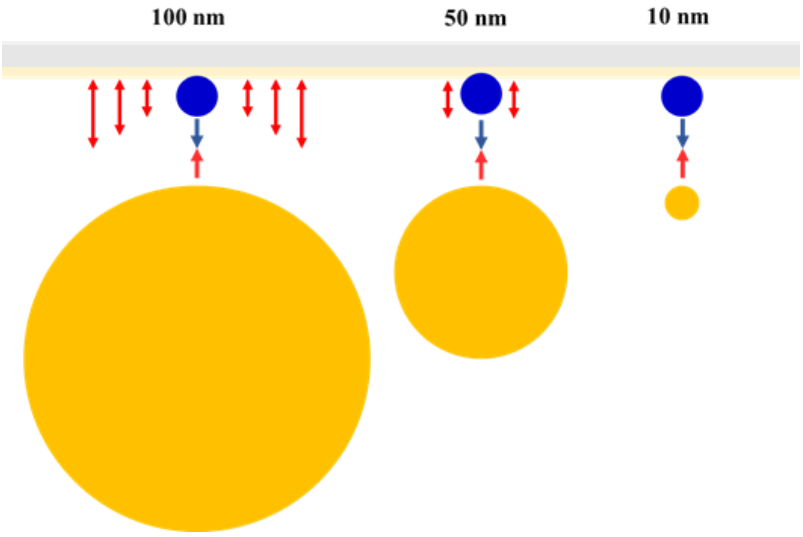

Figure C2. Free body diagram of the relative electrostatic forces acting on gold nanoparticles of varying sizes in the assembly geometry. There are three main elements to take into consideration in this system – the planar, positively-charged substrate; the cylindrical, negatively-charged protein nanofibers; and the spherical, positively-charged gold nanoparticles. Here, gold nanoparticles (yellow circles) approach a cross-section of the protein nanofiber (blue circles) anchored to the silane monolayer (beige plane) on the glass substrate (grey plane).

The protein-particle interaction is characterized as an attractive force (converging blue-red arrows) due to their opposite surface charges. The substrate-particle interaction, however, is characterized as an electrostatic repulsive force (diverging red-red arrows). While this repulsive force drives specific binding and prevents aggregation of the particles, it may also repel the particles from the substrate and therefore the protein nanofiber, preventing nanoparticle assembly.

In addition to the electrostatic forces, according to DLVO theory[2], all elements experience van der Waals attraction between them, which is presumed to be the driving force behind nonspecific attachment.

Furthermore, the nanoparticles in solution are subject to a downward gravitational force. By placing the protein-functionalized substrate face-down in the nanoparticle solution, gravitational sedimentation of gold nanoparticles does not contribute to the overall attachment of nanoparticles.

Supporting Information 3 – Representative Images of Composites at pH 4, 7, and 10

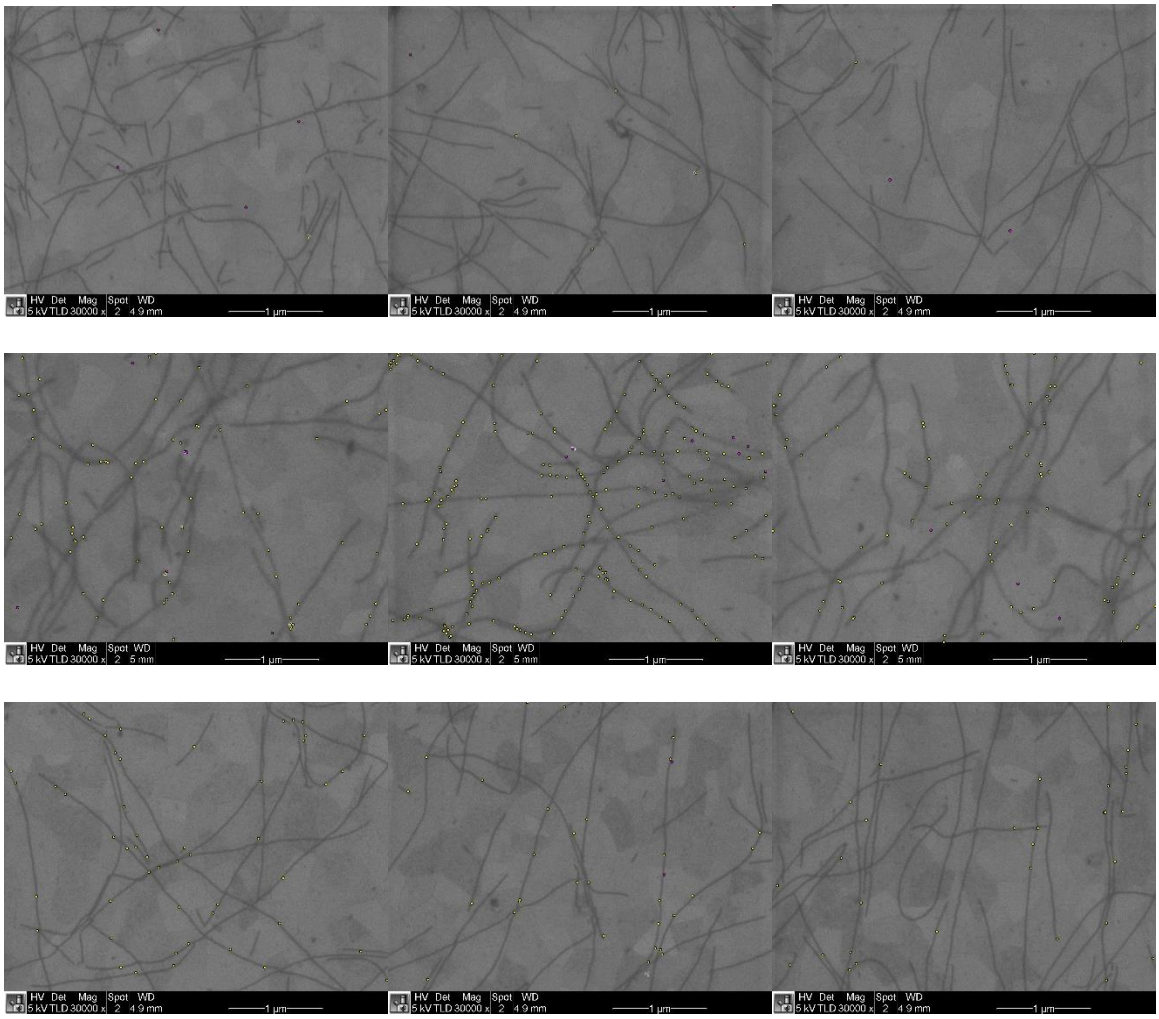

Figure C3a. Representative images from three samples of composites assembled at pH 4.

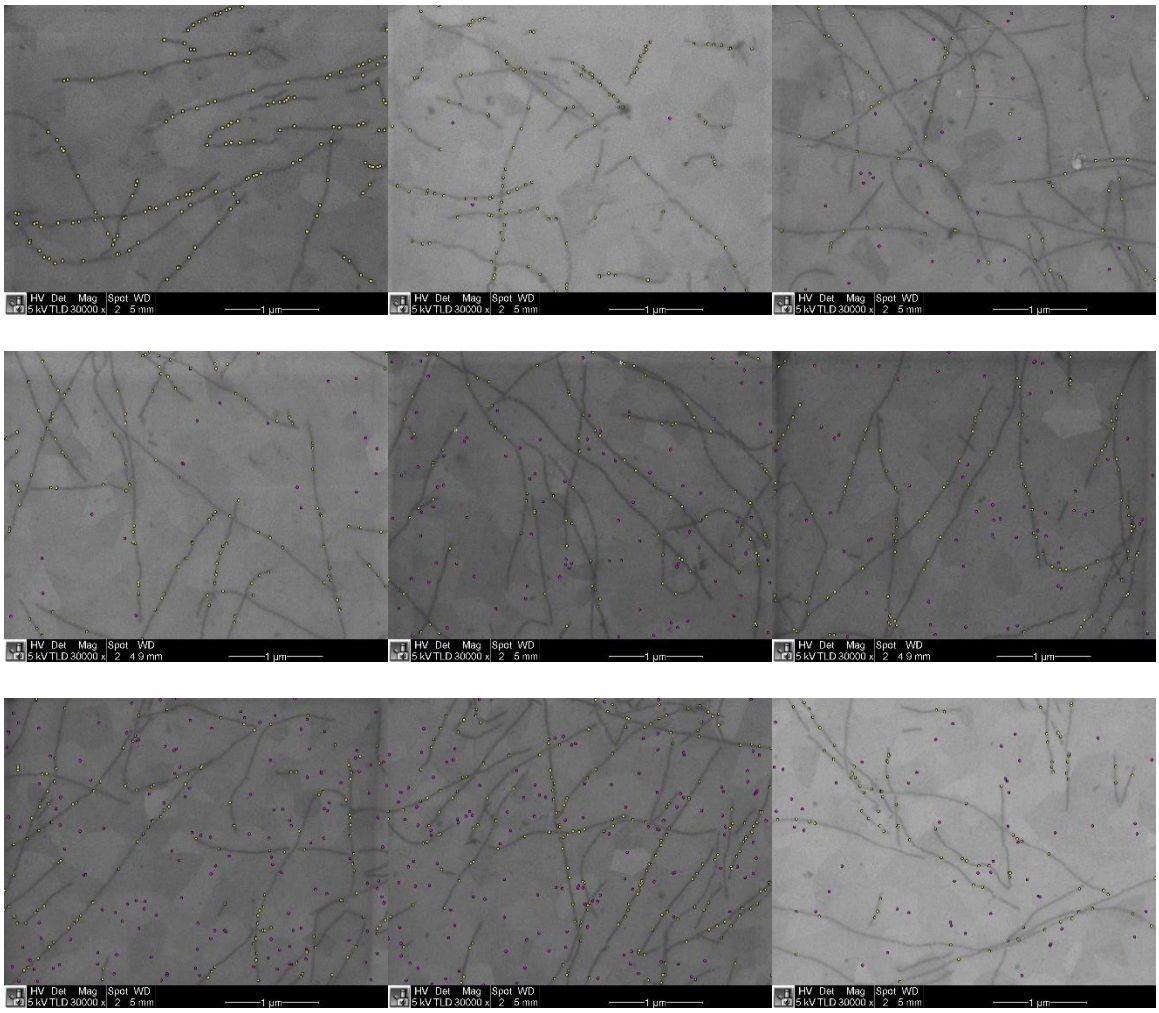

Figure C3b. Representative images from three samples of composites assembled at pH 7.

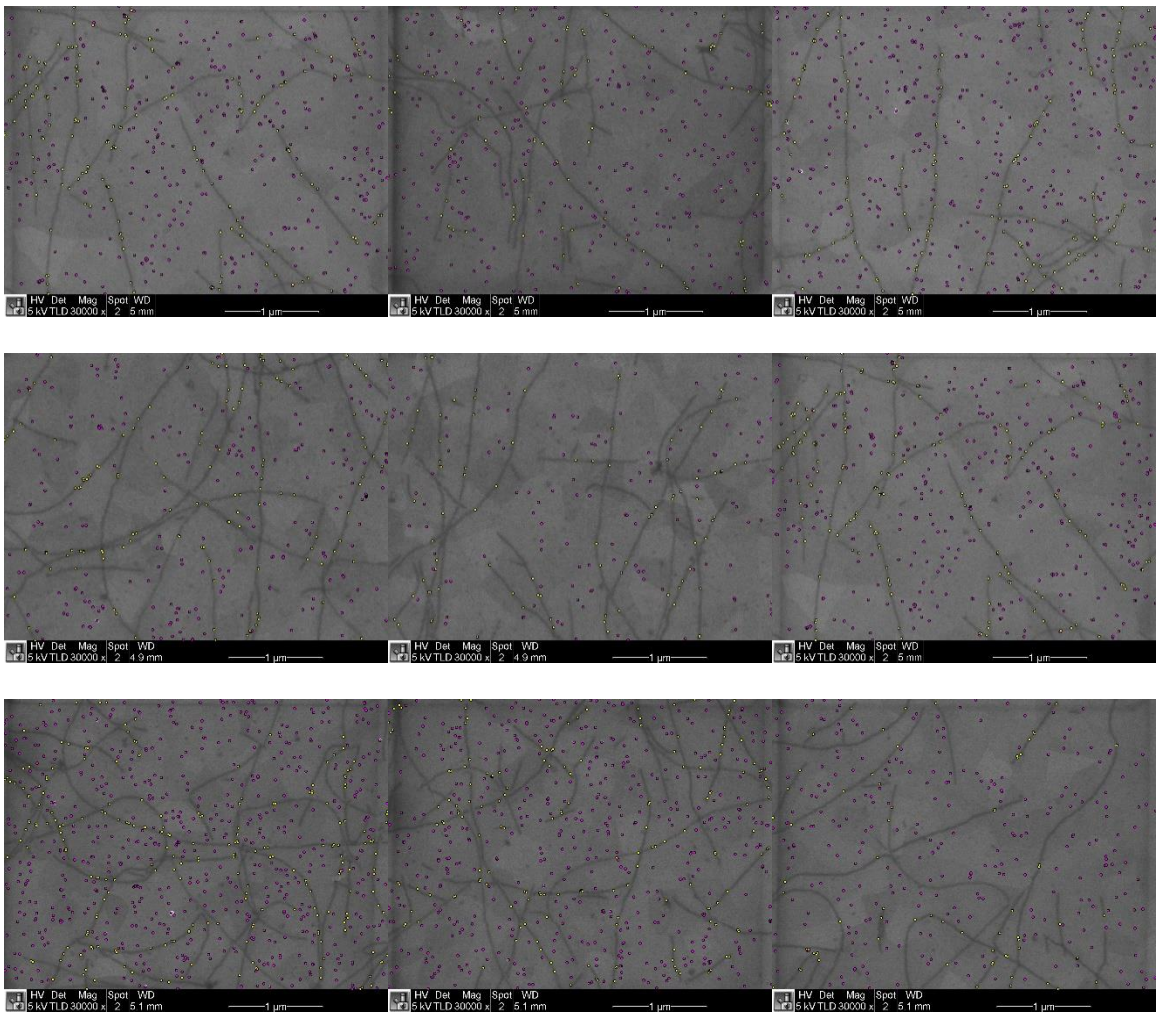

Figure C3c. Representative images from three samples of composites assembled at pH 10.

Supporting Information 4 – Calculation of Theoretical Protonation of APTES and Protein Nanofibers as a Function of pH

For a monolayer of APTES, the pK_a has been measured at 7.6[3]. The ratio of protonated APTES, abbreviated as H:APTES(+) to neutral APTES was then calculated as:

$$\frac{H{:}\,APTES(+)}{APTES} = 1 - \frac{\frac{Ka}{H}}{\frac{Ka}{H} + 1}$$

Unlike the silane monolayer, the protein nanofibers do not only go from charged-to-neutral, but rather negatively-charged, to neutral, to positively-charged as the protein behaves as a collection of pH-responsive residues and therefore pH-responsive functional groups. Therefore, rather than using a single functional group's pK_a, we calculated the isoelectric point[4] of the protein to be 5.66. At a pH below the isoelectric point, the net charge of the protein is positive; at pH 5.66, the average charge of the protein is assumed to be neutral; and above pH 5.66, the protein is net negative. Heterogeneity of residue positioning, however, means electrostatic interactions with the nanoparticles can occur as soon as the carboxylic acid residues begin deprotonating. To visualize the fraction of negatively-charged residues to residues of all charge states, we calculated:

$$\frac{Protein(-)}{Total\ Protein} = \frac{\frac{KI}{H}}{\frac{KI}{H} + 1}$$

Supporting Information 5 – Example of Particle Identification and Nearest Neighbors Labeling

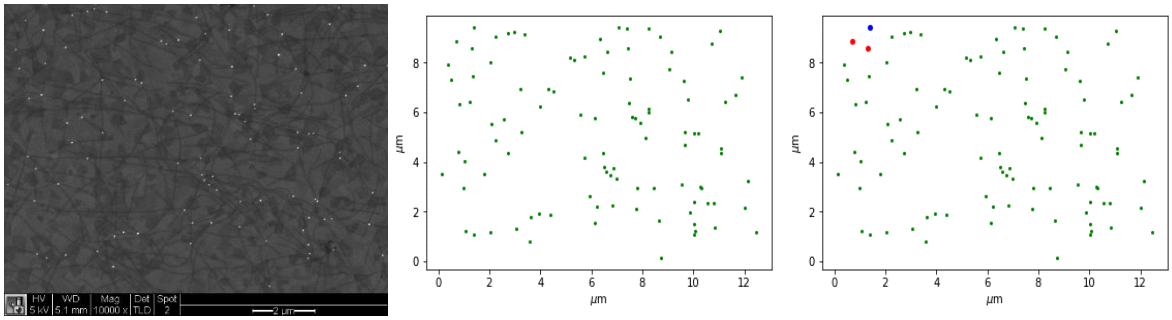

Figure C5. Nanoparticle labeling of a 50 nm gold nanoparticle composite sample for coordinate identification and nearest neighbors calculations. (left) SEM micrograph, (center) nanoparticle positions, (right) example of a nanoparticle (blue) and its labeled two nearest neighbors (red).

REFERENCES

1. Willets, K. A.; Van Duyne, R. P. Localized Surface Plasmon Resonance Spectroscopy and Sensing. *Annu. Rev. Phys. Chem.* **2007**, *58*, 267–297.
2. Israelachvili, J. N. *Intermolecular and Surface Forces*. (Elsevier Science & Technology, 2010).
3. Zhang, H.; He, H. X.; Wang, J.; Mu, T.; Liu, Z. F. Force titration of amino group-terminated self-assembledmonolayers using chemical force microscopy. *Appl. Phys. A Mater. Sci. Process.* **1998**, *66*, 269–271.
4. Gasteiger, E.; Hoogland, C.; Gattiker, A.; Duvaud, S.; Wilkins, M. R.; Appel, R. D.; Bairoch, A. The Proteomics Protocols Handbook. *Proteomics Protoc. Handb.* **2005**, 571–608 doi:10.1385/1592598900.

Kathryn N. Guye
Vitae

Education

Ph.D., Chemistry **June 2021**
University of Washington, Seattle, WA

Dissertation Title: *Optical Characterization of Bio-Inspired Functional Materials, Metal Nanoparticles, and Their Composites*
Advisor: David S. Ginger, Alvin L. and Verla R. Kwiram Endowed Professor of Chemistry, University of Washington

M.S., Chemistry **2020**
University of Washington, Seattle, WA

B.A., Chemistry, *Cum Laude, American Chemical Society Certification* **2015**
Bryn Mawr College, Philadephia, PA
Thesis Title: *Investigation of Dual-Center Ruthenium and Iridium Photocatalysis with Varying Linker Lengths*

Research Experience

University of Washington Department of Chemistry **2015-present**
Advisor: Dr. David S. Ginger
Studied plasmon-enhanced photocatalysis of small organic surface ligands for measuring electron damping and hot carrier emission lifetimes; reversible, reconfigurable stimulus-responsive organic/inorganic composite materials; and, protein-directed assembly of metal nanoparticles, investigating the role of intersurface interactions on assembly dynamics.

Bryn Mawr College Department of Chemistry **2013-2015**
Advisor: Dr. Jonas I. Goldsmith
Investigated ruthenium- and iridium-based organometallic photosensitizers for photocatalytic reduction of water.

Teaching Experience

University of Chemistry Department of Chemistry **2015-2020**
General Chemistry Teaching Assistant
General Chemistry Mentor Teaching Assistant
Honors General Chemistry Teaching Assistant

Bryn Mawr College Department of Chemistry **2014-2015**
General Chemistry Laboratory Teaching Assistant

Publications

8. "Alignment of Au nanorods along de novo designed protein nanofibers studied with automated image analysis" Muammer Y. Yaman, Kathryn N. Guye, Maxim Ziatdinov, Hao Shen, David Baker, Sergei V. Kalinin, David S. Ginger *Accepted, Soft Matter*

7. "Importance of Substrate-Particle Repulsion for Protein-Templated Assembly of Metal Nanoparticles" Kathryn N. Guye, Hao Shen, Muammer Y. Yaman, Gerald Y. Liao, David Baker, David S. Ginger *Under review, Langmuir*

6. "Dual-stimuli responsive single-chain polymer folding via intra-chain complexation of tetramethoxyazobenzene and β-cyclodextrin" *Under review, Langmuir*

5. "Strong Coupling Between Silver Nanoparticles and Hybrid Photon-Exciton Fano Resonances in Two-Dimensional Organic-Inorganic Perovskite Thin Films" Franziska Muckel, Kathryn N. Guye, Shaun M. Gallagher, Yun Liu, David S. Ginger *Under review, ACS Nano Letters*

4. "Molecular fingerprinting of nanoparticles in complex media with non-contact photoacoustics: beyond the light scattering limit" Ivan Pelivanov, Elena Petrova, Soon Joon Yoon, Zhaoxia Qian, Kathryn N. Guye, Matthew O'Donnell *Sci. Rep.* 8 (1), 1-13

3. "Optical properties of reconfigurable polymer/silver nanoprism hybrids: tunable color and infrared scattering contrast" Soumyadyuti Samai, Zhaoxia Qian, Jian Ling, Kathryn N. Guye, David S. Ginger *ACS Appl. Mater. Interfaces* 10 (10), 8976-8984 (2018)

2. "Plasmonic Nanoparticle Dimers with Reversibly Photoswitchable Interparticle Distances Linked by DNA" Soumyadyuti Samai, Tina Lok Yee Choi, Kathryn N. Guye, Yunqi Yan, David S. Ginger *J. Phys. Chem. C* 122 (25), 13363-13370 (2017)

1. "Dynamic optical switching of polymer/plasmonic nanoparticle hybrids with sparse loading" Zhaoxia Qian, Kathryn N. Guye, David J. Masiello, David S. Ginger *J. Phys. Chem. B.* 121 (5), 1092-1099 (2017)

Presentations

"Influence of Surface Charge on Protein-Directed Electrostatic Assembly of Metal Nanoparticles" **Kathryn N. Guye**, Hao Shen, Muammer Y. Yaman, Gerald Y. Liao, David Baker, David S. Ginger *Materials Research Society Spring 2021 Meeting & Exhibit, SM 12.05 Bio-Inspired Hybrid Materials Poster Session,* April 2021

"Towards Dynamic Control of Nanoscale Architectures via Deep Learning Image Analysis and Stimulus-Responsive Materials" **Kathryn N. Guye**, Muammer Yaman, Maxim Ziatdinov, Xin Li, Shuai Zhang, Amy Stegmann, Harley Pyles, Julia Boese, Hao Shen, David Baker, James J. De Yoreo, François Baneyx, Andrew Ferguson, Sergei V. Kalinin, David S. Ginger *Department of Energy, Energy Frontiers Research Center Midterm Review Poster Session,* February 2020

"Machine Learning Methods for 2D Images and Hyperspectral Data" Maxim Ziatdinov and **Kathryn N. Guye** *Center for the Science of Synthesis Across Scales Annual Meeting,* October 2019

Honors and Awards

Best Poster Nominee Materials Research Society Spring 2021 Meeting & Exhibit